TECHNISCHE UNIVERSITÄT MÜNCHEN

Klinikum rechts der Isar der Technischen Universität München
Abteilung für Diagnostische und Interventionelle Neuroradiologie

From Tissue Perfusion to Oxygenation: Characterizing Glioma Heterogeneity with Dynamic Susceptibility Contrast Enhanced Magnetic Resonance Imaging

Anne Kathrin Kluge

Vollständiger Abdruck der von der Medizinischen Fakultät der Technischen Universität München zur Erlangung des akademischen Grades eines

Doktors der Naturwissenschaften (Dr. rer. nat.)

genehmigten Dissertation.

Vorsitzender: Prof. Dr. Claus Zimmer

Prüfer der Dissertation:

1. Priv.-Doz. Dr. Christine Preibisch
2. Prof. Dr. Axel Haase

Die Dissertation wurde am 13.04.2017 bei der Technischen Universität München eingereicht und durch die Medizinische Fakultät am 09.08.2017 angenommen.

Abstract

Cellular heterogeneity, altered microvasculature and hypoxic niches are considered major causes of treatment resistance of tumors. The cerebral blood volume (CBV) helps to differentiate between tumor grades, to assess their therapy response and to quantify their oxygen consumption. The procedure most frequently used to determine CBV is dynamic susceptibility contrast-enhanced magnetic resonance imaging (DSC-MRI). Using fast successive MR images, the signal intensity can be tracked while a gadolinium-based contrast agent is rapidly injected. The contrast agent induces susceptibility effects leading to a signal intensity drop. The CBV is calculated on the principle of kinetic modeling intravascular tracers. Different algorithms and influencing factors complicate comparisons of CBVs obtained from different studies. In the presence of a disrupted blood-brain-barrier, e.g. in high-grade gliomas, the contrast agent extravasates, further compromising the measurement.

An adapted image post-processing or a modified acquisition, such as the administration of a pre-bolus that saturates the tissue with contrast agent, reduces calculation errors in tissues with a disrupted blood-brain-barrier. Recently gadolinium has been found to deposit in brain tissue. Thus, dosages should be minimized. An optimal post-processing is therefore to be favored. So far no standardized, reliable CBV analysis has been developed.

To find the most robust CBV, four calculation methods correcting contrast agent extravasation were thoroughly examined. Each processing step was optimized, including tissue segmentation, conversion of MR signals in contrast agent concentration, selecting the arterial input function and CBV calculation itself. In simulations individual methods were investigated and influences, such as signal-to-noise ratios and the strength of extravasation, were isolated. Within this work, DSC-data from two studies were analyzed. Patients with high-grade gliomas received either two contrast agent boli of different dosages or two types of contrast agent. In order to measure the oxygen consumption of tissue and to characterize tumor heterogeneity, additional relaxation maps and dynamic T1-weighted perfusion MRI were acquired simultaneously with positron emission tomography. Comparisons of CBVs based on the perfusion data enabled the identification of the most stable and reliable image processing.

Regarding CBV quantitation, each method yielded different absolute values. Except for one, all DSC-based CBVs were significantly higher than reported literature values measured with gold standard positron emission tomography. Although the arterial input function could be regarded as stable, partial volume effects and the complex signal-to-concentration behavior have been identified as the main reason for quantification problems. Considering extravasation effects improved the accordance between CBVs compared to standard procedures, but still showed high variability among patients and

processing methods. More reproducible maps with physiologically reasonable values could only be generated by normalizing CBVs to healthy white matter.
Accordingly, in this work a completely automatic tool for analyzing DSC data has been developed. The tool enables a fast and reproducible determination of CBV, independent of the arterial input function and contrast agent extravasation. Although no quantitative CBV could be determined, it was possible to generate nearly identical relative CBV values for different types and doses of contrast agents, acquisition parameters and integration intervals. In addition to reducing the dose of contrast agent, this tool allows for better comparability of different studies. Furthermore, first images of tissue oxygenation based on optimized CBVs yielded promising results.

Zusammenfassung

Zelluläre Heterogenität, veränderte Blutgefäßstrukturen und hypoxische Nischen werden als Hauptursachen für die Resistenz von Tumoren gegenüber Therapien angesehen. Das zerebrale Blutvolumen (CBV) kann helfen zwischen Tumorgraden zu unterscheiden, ihr Therapieansprechen zu bewerten und deren Sauerstoffverbrauch zu quantifizieren. Das am häufigsten verwendet Verfahren zur Bestimmung des CBV ist die dynamische Suszeptibilitätskontrast Magnetresonanztomographie (DSC-MRT). Unter Verwendung von zeitlich hochaufgelösten 4D MRT-Bildserien kann der Signalintensitätsabfall, verursacht durch Suszeptibilitätseffekte des injizierten gadoliniumhaltigen Kontrastmittels, verfolgt werden. Das CBV kann dann mittels kinetischer Modellierung intravaskulärer Tracer errechnet werden. Unterschiedliche Algorithmen und verschiedene Einflussfaktoren erschweren hierbei den studienübergreifenden Vergleich dieses Parameters. Physiologische Variabilität, wie sie beispielsweise bei einer gestörten Blut-Hirn-Schranke und der damit verbundenen Extravasation des Kontrastmittels auftritt, erschwert die Quantifizierung des CBV zusätzlich. Eine adaptierte Bildnachverarbeitung oder eine modifizierte Akquisition, wie die Verabreichung eines Prä-Bolus, der das Gewebe mit Kontrastmittel sättigt, kann Messfehler in Geweben mit einer gestörten Blut-Hirn-Schranke reduzieren. Allerdings konnte vor kurzem eine potentiell schädliche Akkumulation von Gadolinium im Hirngewebe nachgewiesen werden. Diese Arbeit beschäftigt sich daher mit der Optimierung von Auswertemethoden zur Berechnung des CBV um die Gadolinium-Dosierung zu minimieren. Vier Berechnungsmethoden zur Korrektur der Kontrastmittel-Extravasation wurden mit Hinblick auf ihre Genauigkeit und Stabilität untersucht. Jeder Verarbeitungsschritt, einschließlich Gewebesegmentierung, Umwandlung des MR-Signals in Kontrastmittelkonzentration, Auswahl der arteriellen Eingangsfunktion und die CBV-Berechnung selbst, wurden optimiert. In Simulationen wurden einzelne Verfahren detaillierter untersucht und Einflüsse, wie das Signal-zu-Rausch-Verhältnis und die Stärke der Extravasation, isoliert. Im Rahmen dieser Arbeit wurden DSC-Daten von verschiedenen Patientenstudien analysiert. In zwei Studien erhielten Patienten mit hochgradigen Gliomen entweder zwei Kontrastmittelboli mit verschiedenen Dosierungen oder zwei unterschiedliche Kontrastmittel. Um den Sauerstoffverbrauch des Gewebes zu messen und die Tumor-Heterogenität zu charakterisieren, wurden zusätzlich die transversalen Relaxationszeiten kartiert und dynamische, T1-gewichtete Perfusions-MRT Daten parallel zu einer Positronen-Emissions-Tomographie aufgenommen. Vergleiche von CBV, basierend auf den Perfusionsdaten, ermöglichten die Identifizierung der stabilsten und zuverlässigsten Bildverarbeitungsmethode.

Bezüglich der CBV-Quantifizierung lieferte jedes Verfahren unterschiedliche absolute Werte. Bis auf eines, lieferten alle DSC-basierten Methoden CBV Werte, die signifikant

höher waren als Literaturwerte, die mit dem Goldstandard Positronen-Emissions-Tomographie ermittelt wurden. Obwohl sich die automatische Bestimmung der arteriellen Eingangsfunktion als stabil erwies, wurde die Quantifizierung des CBV, aufgrund von Partialvolumeneffekten und des komplexen Signal zu Konzentrations-verhaltens, hauptsächlich durch deren Skalierung, beeinträchtigt. Die Betrachtung von Extravasationseffekten verbesserte die Übereinstimmung zwischen den mit unterschiedlichen Methoden ermittelten CBV Werten, zeigte jedoch eine hohe Variabilität zwischen den Patienten und den Verarbeitungsmethoden. Reproduzierbare Karten mit physiologisch sinnvollen Werten konnten nur durch die Normierung der CBV Werte auf gesunde weiße Substanz erzeugt werden.

Um eine möglichst robuste und reproduzierbare Auswertung von DSC-Daten für klinische Studien und diagnostische Anwendungen zu entwickeln, wurde in dieser Arbeit ein automatisches Verfahren zur Analyse von DSC-Daten entwickelt. Das Tool ermöglicht eine schnelle und reproduzierbare Bestimmung von CBV-Parameterkarten, unabhängig von der arteriellen Eingangsfunktion und der Kontrastmittel-Extravasation. Obwohl das CBV nicht quantitativ bestimmt werden konnte, war es durch Normierung möglich, nahezu identische Werte für verschiedene Typen und Dosierungen von Kontrastmitteln, Akquisitionsparametern und Integrationsintervallen zu erzeugen. Neben der Reduktion der Kontrastmitteldosis ermöglicht dieses Tool eine bessere Vergleich-barkeit verschiedener Studien. Darüber hinaus ergaben erste Parameterkarten der Oxygenierung des Hirngewebes, die auf Basis optimierter CBV-Karten berechnet wurden, vielversprechende Ergebnisse.

Content

1 Introduction

1.1 Microstructural Heterogeneity in Gliomas

Gliomas are among the most treatment-resistant brain tumors [1, 2]. Strong cellular heterogeneity, altered signaling pathways and hypoxic niches are considered major reasons for this resistance. Due to heterogeneity, certain therapy concepts work only in sub-regions with responsive cells [3, 4]. Cancer stem cells as well as hypoxic cells, for example, are known to be especially resistant to standard therapy concepts (radiotherapy, chemotherapy) and therefore play an import role in tumor initiation, angiogenesis and progression [2]. One leading cause of high tumor proliferation is the development of new blood vessels (angiogenesis); consequently, several treatment approaches use anti-angiogenic agents that inhibit vascular endothelial growth factor signaling pathways [5]. Accordingly, the characterization of gliomas regarding their microstructural heterogeneity is a prerequisite for an optimal combination of treatment modalities. Due to their fast tumor growth a special characteristic of the microvasculature in gliomas is that vessels are often tortuously organized and highly permeable. The increased vascular permeability arises from a compromised blood-brain barrier (BBB), and mechanisms increasing BBB permeability are the reduced expression or destruction of tight junction enzymes, which act in healthy brains as a physical barrier [6]. The permeability of blood vessels is thought to reflect the amount of angiogenesis and could potentially function as a surrogate marker for tumor growth [7]. Furthermore, the tortuous vessel structure could lead to an imbalance between oxygen supply (mitochondrial respiration) and consumption (oxygen bound to hemoglobin). Initially, the organism seeks to compensate for this imbalance by adapting blood flow and vessel dilation. Once those possibilities are exhausted, hypoxic tumor regions are formed. One reason for hypoxia is restricted perfusion, due to occluded vessels, or increased interstitial pressure. An inadequate blood supply might create an acute hypoxia [8]. Another reason for this imbalance may be inappropriate vasculature so that some cells are more than 70 μm apart from the next supporting vessel. This distance corresponds to the diffusion length of O_2; thus, these cells are not provided with oxygen. An oxygen shortage might also be a result of a cancer treatment that could reduce the capacity of blood to transport O_2 [8]. Typically, hypoxia is a temporary phenomenon, because microvasculature is constantly changing. Cells that survive the hypoxic conditions adapt to this environment by changing molecular pathways. These intermediate hypoxic cells are suspected to be detrimental for patient survival because they are more therapy resistant and aggressive. Both tumor resistance and aggressiveness are highly dependent on physical properties of the vasculature and hemodynamic properties of the tumor. Non-invasive imaging of hypoxia and vascular parameters would

thus improve tumor grading and control by offering measures for monitoring the response to individualized therapy concepts.

1.2 Motivation and Outline

The motivation behind this study was to improve the detection of hypoxia using magnetic resonance imaging (MRI). To quantify the oxygen consumption of tissue, the percentage of oxygen removed from the blood during its passage through the capillary network can be characterized, a ratio termed oxygen extraction fraction (OEF). The underlying approach to measuring the OEF was developed by Yablonskiy and Haacke [9]. It utilizes the differences in magnetic properties between oxygenated and deoxygenated blood. A clinically applicable MRI method to measure a relative OEF (rOEF) is based on separate measurements of the transverse relaxation rates and cerebral blood volume (CBV) [10].

Besides its relevance for OEF determination, the quantification of tissue perfusion is also extremely important in itself, e.g. for clinical tumor grading and the assessment of tumor heterogeneity [11]. However, reliable quantitation of an absolute blood volume is challenging. Especially in tumors and other brain injuries where the BBB is disrupted, CBV determination with standard perfusion imaging is error-prone and may lead to either under- or overestimation [12]. This dissertation focuses therefore on the correction of these effects for the most widely used MRI perfusion technique, dynamic susceptibility contrast (DSC). Several correction methods have been proposed to counteract the extravasation problem, many of which concentrate on post-processing techniques [12-17]. Other researchers developed new acquisition strategies, such as the dual echo approach, where images with two different TEs are acquired during the bolus passage to isolate T2* changes [18] or the application of a pre-bolus to saturate the tissue with CA [19]. The latest concepts include both optimized acquisition and post-processing [20-22]. The large variety of methods hinders comparisons of CBV values obtained from different studies. Since no clear consensus exists in the literature about reliability, quality and stability of adequate post-processing [23], a systematic analysis is required. In this work, four extravasation correction methods are investigated in combination with a pre-bolus technique. The existing methods are optimized and validated using simulations and patient data from double dose studies and simultaneous positron emission tomography (PET) acquisitions. Since recent publications [24] caution against the careless use of gadolinium-based contrast agents because of depositions detected in the brain, the applicability of an alternative high relaxivity contrast agent for magnetic resonance perfusion imaging and a possible reduction of contrast agent dose are also evaluated. Additionally, general problems of absolute CBV quantitation are scrutinized.

Chapter 2 briefly summarizes the background of MRI and PET as well as the biological basics and general concepts of perfusion imaging. The peculiarities of CBV quantification

and extravasation correction methods, which are investigated in this work, receive detailed attention in chapter 3. The results of simulations and examinations on patient data are described in chapter 4, showing a high variability of CBV values with post-processing methods. In chapter 5, those results are discussed in the context of the literature, and the usefulness of additional permeability related parameters are investigated. Further, sources of errors as well as the effect of a leakage corrected CBV on rOEF are outlined. The concluding chapter (chapter 6) offers suggestions for selecting the best methods under consideration of the clinical questions as well as for future improvements.

2 Theoretical Background

2.1 Basics of Magnetic Resonance Imaging

2.1.1 Nuclear Magnetic Resonance

Clinical magnetic resonance imaging in general exploits the magnetic properties of the hydrogen nucleus because it is the most abundant element in the body. Moreover, its magnetic properties are particularly advantageous. The hydrogen nucleus consists of a single proton, which, like all protons, possesses an intrinsic angular momentum (spin) $\boldsymbol{I}$ and a magnetic dipole momentum $\boldsymbol{\mu}$. The angular momentum and magnetic dipole momentum of a proton are directly linked over a nucleus-specific constant called gyromagnetic ratio γ:

$$\boldsymbol{\mu} = \gamma \boldsymbol{I} \tag{2.1}$$

With a value of $2.675 \cdot 10^8$ rad s^{-1} T^{-1} hydrogen has the largest gyromagnetic ratio in nature. Whenever a hydrogen atom is placed in an external static magnetic field ($\boldsymbol{B_0}$), the energy level of its nucleus is split into two possible energy states (Zeeman effect). The quantization of direction allows only two discrete, opposite polarities (parallel or anti-parallel aligned to $\boldsymbol{B_0}$), taking on the energies:

$$E_m = -\gamma \hbar m \boldsymbol{B_0} \qquad , with \ m = \pm \frac{1}{2} \tag{2.2}$$

Here, $\hbar$ is the Planck's constant divided by 2π, and m is the magnetic quantum number. The energy difference ΔE between the two energy states is associated with the specific resonance frequency of the nucleus, called the Larmor frequency $\boldsymbol{\omega_0}$, according to:

$$\Delta E = \hbar \boldsymbol{\omega_0} \tag{2.3}$$

The relation to $\boldsymbol{B_0}$ is then given by combining Eqs. (2.2) and (2.3):

$$\boldsymbol{\omega_0} = \gamma \boldsymbol{B_0} \tag{2.4}$$

To induce transitions between the two energy states, a second orthogonally oriented alternating magnetic field oscillating with the Larmor frequency has to be applied ($\boldsymbol{B_1}$) [25].

2.1.2 Macroscopic Magnetization

For imaging, not only a single spin, but a spin ensemble needs to be considered. The number of magnetic moments in an ensemble taking on one of the two allowed energy states is defined by the Boltzmann distribution. At body temperature, the difference in this number is very small, however, because of the large number of spins in an ensemble, a measurable magnetic moment in direction of $\boldsymbol{B_0}$ exists, called macroscopic magnetization $\boldsymbol{M}$. In the classical picture, this dipole moment experiences a torque if placed in an external field. Thus, the magnetization behavior can be described by a vector $\boldsymbol{M}$ that precesses with the Larmor frequency $\boldsymbol{\omega_0}$ around the axis of $\boldsymbol{B_0}$. The magnetization $\boldsymbol{M}$ can be divided into two components: the longitudinal magnetization M_z (parallel to $\boldsymbol{B_0}$) and the transversal magnetization M_{xy} (orthogonal to $\boldsymbol{B_0}$). In thermal equilibrium $M_{xy} = 0$, and $M_z = |\boldsymbol{M}| = M_0$, where M_0 is the equilibrium magnetization. For further descriptions, a system that rotates with the Larmor frequency around the z-axis is considered. In this rotating frame system, those spins rotating with the Larmor frequency are stationary, while those with divergent frequency show a phase difference [25].

2.1.3 Excitation and Relaxation

In the state of equilibrium the system is stable. By applying a radiofrequency (RF) pulse with the frequency $\boldsymbol{\omega_0}$ ($\boldsymbol{B_1}$ field), the magnetization $\boldsymbol{M}$ is rotated towards the transverse plane. Depending on the length and the amplitude of the RF pulse the degree of rotation, or flip angle α, is specified. If $\alpha = 90°$, $\boldsymbol{M}$ is rotated onto the xy-plane, while, for $\alpha = 180°$, the magnetization is inversed. In a quantum-mechanical sense, this excitation lifts the protons into the higher energy state. After the RF pulse is turned off, the protons return to the equilibrium state by emitting energy in form of radiofrequency waves. In the classical picture, this event is represented by rotating the macroscopic magnetization back in the z-direction. This process is called T1 relaxation or spin-lattice-relaxation. With a 90° flip angle, the magnetization is not only flipped onto the xy-plane, but the spins are synchronized in their phase. After time elapses, given the Brownian motion and diffusion of atoms and molecules that take place, spin-spin interactions occur and the phase coherence of the spins diminishes. This dephasing process, called T2 relaxation, reduces the net magnetization. In reality, inhomogeneities of the main magnetic field lead to additional dephasing, resulting in a faster effective transverse relaxation time, referred to as T2*. Both, T1 and T2 are tissue specific, since intramolecular interactions differ

between substances. In addition to the proton density, these interactions build the basis of MR contrast (section 2.4).

The classical description of the temporal evolution of the magnetization vector $\boldsymbol{M}$ in the presence of external magnetic fields $\boldsymbol{B}_{eff}$ and relaxation effects are known as Bloch-Equations (2.5):

$$\begin{aligned} \frac{dM_x(t)}{dt} &= \gamma\left(\boldsymbol{M} \times \boldsymbol{B}_{eff}\right)_x - \frac{M_x(t)}{T2} \\ \frac{dM_y(t)}{dt} &= \gamma\left(\boldsymbol{M} \times \boldsymbol{B}_{eff}\right)_y - \frac{M_y(t)}{T2} \\ \frac{dM_z(t)}{dt} &= \gamma(\boldsymbol{M} \times \boldsymbol{B}_{eff})_z - \frac{M_z(t) - M_0}{T1} \end{aligned} \tag{2.5}$$

2.1.4 Basic Sequence Designs

In MRI, in principle two pulse sequence designs exist for echo generation. In the following, both are briefly explained.

In **spin echo** (SE) experiments (Figure 2.1), a 90° RF excitation pulse is followed by an 180° refocusing pulse. After excitation, the spins dephase until the refocusing pulse is applied, which then reverses their individual phases. After that, the spins continue to dephase in the same direction so that the faster precessing spins, now at the back of the pack, start to outrun the slower ones. After a time period that is equal to the time period between the 90° and 180° RF pulses (TE/2), the spin echo is formed [25].

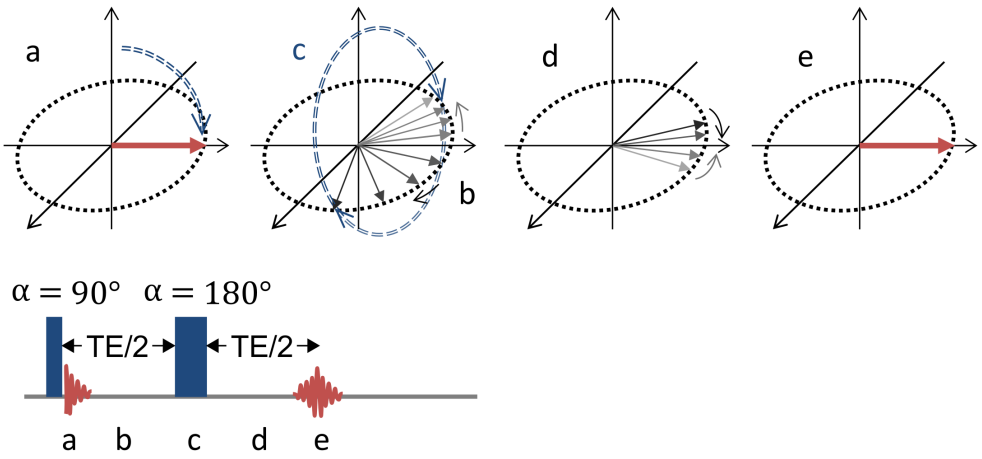

Figure 2.1: Spin echo experiment. (a) After a 90° RF pulse, the magnetization is flipped to the xy-plane. (b) After that the natural relaxation process begins, meaning the spins begin to dephase. (c) With the 180° refocusing pulse faster precessing spins (dark gray) and slower precessing spins (light gray) are flipped around one transverse axis so that the faster precessing spins end up behind (negative phase difference) the slower precessing spins. (d) Thus, the faster precessing spins start to outrun the slower precessing spins and (e) an echo is formed after an echo time TE.

In case of **gradient echo** (GE) experiments, the magnetization is excited with a single RF pulse (Figure 2.2). Subsequently, the spins begin to dephase. The natural dephasing is accelerated by an additional spatially inhomogeneous magnetic field, referred to as gradient $\boldsymbol{G}$ (section 2.1.5). Due to this gradient, the precession frequencies of the spins are locally different. Switching the gradient to the opposite polarity corresponds to a reversal of the direction of this additional magnetic field. This forces the spins to rephase by slowing down the previously faster precessing spins and accelerating the previously slower ones until an echo is generated [25].

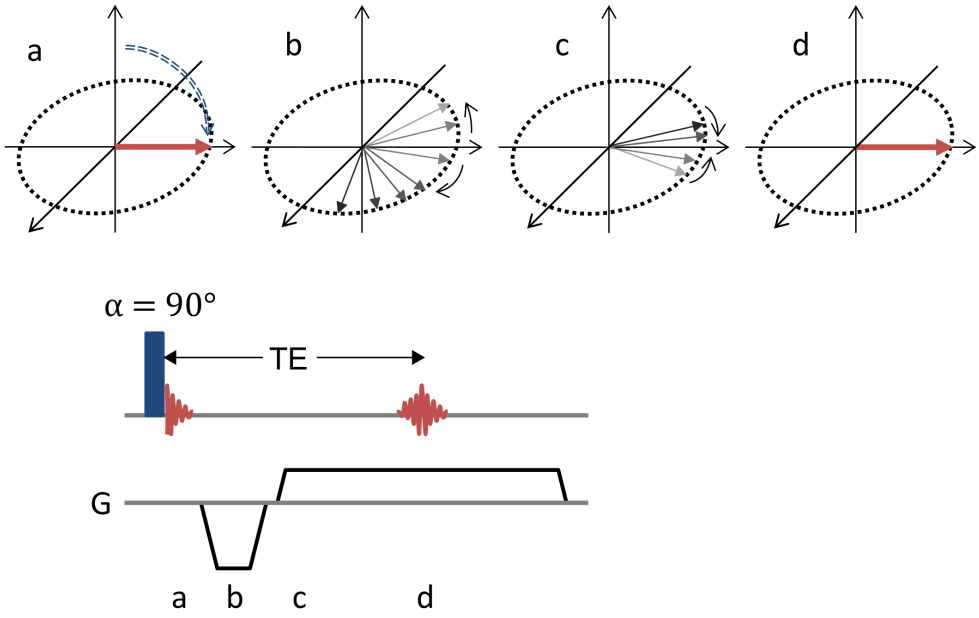

Figure 2.2: Gradient Echo Experiment. (a) After a 90° RF pulse, the magnetization is flipped onto the xy-plane. (b) The natural dephasing process is accelerated by the gradient G. (c) After the gradient is changed to opposite polarity; the previously faster precessing spins (dark gray) are slowed down (light gray) and the previously slower precessing spins (light gray) are accelerated (dark gray), leading to rephasing. (d) The gradient echo is formed after the time period TE.

2.1.5 Image Acquisition

After RF excitation, during the relaxation process, radiofrequency waves are emitted by the nuclear spins. They induce a signal without any spatial information in the scanner receiver coil. For spatial encoding, three additional magnetic field gradients in direction of $\boldsymbol{B_0}$ are applied, which generate linear variations in the static magnetic field strength along the three coordinates in space (x, y, z). In the following, it is assumed that the z-gradient is used for slice selection; x- and y-gradients specify frequency and phase encoding direction, respectively. Slice selection exploits that spins can only be excited using an RF pulse with a frequency identical to the Larmor frequency of the spins. Since the precession frequency of the spins depends on the magnetic field strength, once the z-gradient G_z is switched on, the resonant frequency at position z is $\omega(z) = \gamma(\boldsymbol{B_0} + G_z z)$. By using an RF pulse with the frequency $\omega(z)$ and a bandwidth of $\Delta\omega$, it is possible to target only spins in a slice of thickness Δz. At position z, the precession frequencies in the x-direction are spatially dependent on the x-gradient, which is turned on during readout. The third dimension can be encoded by the y-gradient, which is switched on for a defined time with a specific strength prior to readout. This procedure is repeated many times, where the number of repetitions characterizes the number of

measured points (resolution) in y-direction. During the time this gradient is on, the precession frequency of the spins changes along the gradient leading to different phases along the y-axis. After turning off the gradient, the frequencies are the same as before but the phase of the spins remains different, allowing encoding of the phase. The result of the encoding process is a raw signal that consists of a superposition of the spatially varying frequencies. This frequency distribution with the corresponding amplitudes is stored in k-space. The signal represented in k-space is the inverse Fourier transformation of the transverse magnetization in the rotating frame. The coordinates of k-space can be expressed in dependence on the gradients: $k_x = \frac{\gamma}{2\pi} G_x \Delta t\, m$ and $k_y = \frac{\gamma}{2\pi} \Delta G_y \tau\, n$, with the sampling interval Δt between the m sampling points during the frequency encoding gradient G_x and τ the duration of the gradient G_y for each of the n phase encoding steps. Figure 2.3 shows the basic principle of filling the k-space line per line, where every line represents one phase-encoding step. With a two-dimensional Fourier transform, a conversion to the spatial distribution of signal intensities (magnitudes), the actual image, is possible [25].

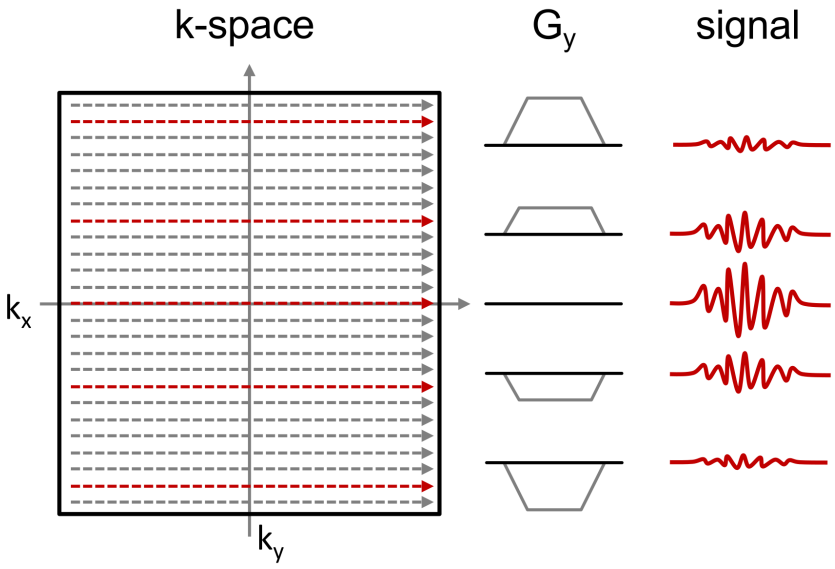

Figure 2.3: Standard filling trajectory of k-space. Each line corresponds to the superpositon of signals with different frequencies and phases from the entire slice (see right column) that is generated after one RF excitation. The phase encoding gradient G_y changes from negative (bottom) to positive values (top). k_x = frequency encoding direction, k_y = phase encoding direction.

One of the fastest acquisition techniques is **Echo Planar Imaging (EPI)** [26]. With this sequence, it is possible to collect all data for one slice after one single RF excitation (single-shot EPI). This is done by rapidly reversing the gradient in frequency encoding direction. The phase encoding is done for each echo separately, using either a constant-

amplitude gradient lobe or small 'blip' gradients. EPI is the method of choice for diffusion, perfusion and functional brain imaging [25].

2.2 Basics of Positron Emission Tomography

Positron emission tomography (PET) is a technique that visualizes metabolism using positron (β+) emitting nuclides. Prior to imaging, the radioactively labeled substance is injected into the venous system. Because of the high specific activities and the physical properties of the emitted positrons, high-quality quantitative images of low tracer concentrations are possible. This section gives a short overview of the basic principles. For more detailed information please refer to [27].

β+ decay: During the β+ decay, one proton of the nucleus converts into a neutron and emits a positron (and a neutrino). Depending on its kinetic energy, this positron travels some way through the tissue, slowing down before it finally annihilates with a shell electron. If the positron has nearly no residual kinetic energy, the annihilation is most probable. Two photons of 511 keV, which equals the rest energy of positrons and electrons, are emitted in opposite directions. If both particles completely lost their kinetic energy, they separate each other collinear. A residual kinetic energy will decrease this collinearity.

Photon detection: Most modern PET systems are 3D scanners, consisting of several detector rings. They convert the absorbed photon energy into an electrical impulse using scintillators and photomultiplier marking it with a time stamp. To detect only annihilation and reject scatter photons, their energies have to exceed a predefined threshold (energy collimation). The time and the position of the detectors that registered two photons simultaneously (coincidence) will give a line of response on which the annihilation event took place. For qualitative and quantitative evidence, corrections for individual detector efficiencies, detector dead times and for the physical decay of the radioactive substance have to be made. In addition, background events, like random and scattered coincidences, decrease image quality. Random coincidences occur if by chance two single photons are simultaneously detected and counted as coincidence event. Scattered coincidences arise from scattered photons that changed their direction, but still have enough energy to exceed the predefined threshold. Thus, the incorrectly determined lines of response lead to a decreased signal-to-background ratio. Scattering and absorption further attenuate the signal yield. The probability of detecting a photon decreases if its traveling distance through the tissue increases because interactions with atoms become more probable. Thus, the activity inside the body is underestimated compared to that from the periphery of the body. To correct this, a map of attenuation coefficients is acquired for quantitative reconstruction. Possible acquisition methods are a transmission scan with a rotating radioactive source, a computer tomography or special MR sequences that allow a discrimination of different tissue types. For each tissue,

corresponding attenuation coefficients are either measured or later assigned. This allows an intensity correction for each line of response. After all these corrections and a scanner calibration with the injected activity, absolute measurements of activity concentrations in decays per second and milliliter are possible.

Reconstruction: In order to obtain 3D images, the measured lines of response must be reconstructed. For this purpose, all lines of response running parallel to each other are summed up to one intensity profile. That results in one projection for every angle. With a filtered back-projection of the intensity profiles, the origin of the annihilation processes can be located and depicted as an activity distribution. Besides this simple reconstruction algorithm, iterative methods become more common. In principal, they iteratively compare the measured projections with forward projected intensity profiles of an estimated image. This estimated image is altered until the deviations between measured and expected projections are minimized.

2.3 Cerebral Perfusion

2.3.1 Physiology

Cerebral perfusion is a rather general expression, specifying the process of blood delivery from the arteries to the capillary bed of tissue, supplying nutrients as glucose and oxygen. To cover the nutrition consumption of the brain, 15 % of the total cardiac output of blood is delivered to the head [28]. Within the brain, perfusion is heterogeneous depending on the local construction of the vascular network (vessel radii, length and number) and the blood velocity (Figure 2.4).

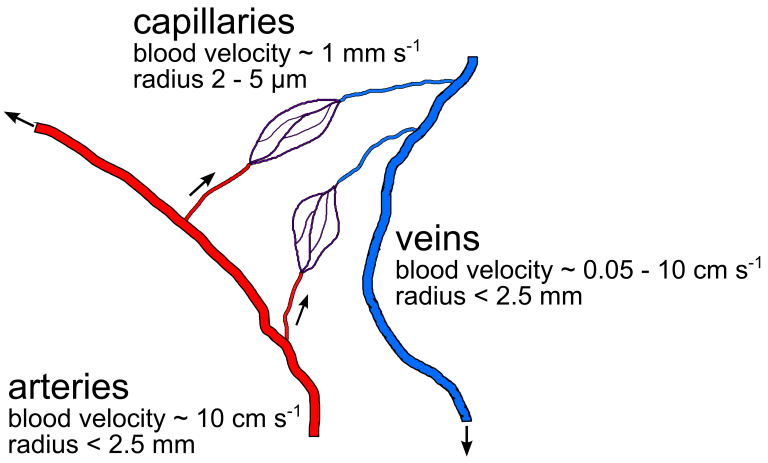

Figure 2.4: Schematic illustration of a capillary bed figured as an artery (red), vein (blue) and the capillaries (magenta) with typical vessel radii and blood velocities [29]. Adapted from [Fig. 2.2 A in 28] Figure 2.2 A.

In simplified terms, the biological tissue consists of cells, vessels and the extracellular-extravascular space (EES). Considering a defined tissue volume in brain, the volume belonging to vessels is the cerebral blood volume (CBV), the volume of arterial blood, that is delivered per minute to the considered tissue, represents the cerebral blood flow (CBF) and the time the blood needs to travel through the capillary bed on average is called mean transit time (MTT). These three parameters are linked by the central volume principle [28]:

$$MTT = \frac{CBV}{CBF} \tag{2.6}$$

In general, CBV is stated in ml per 100 g tissue, CBF in ml per 100 g tissue and per minute and MTT in seconds. In some applications, CBV is determined in percent as a volume fraction. This can be assumed to be equivalent to ml per 100 g because the mass density of tissue is close to 1 g/ml [28]. Typical perfusion values in healthy human brain are different for gray and white matter (Table 2.1). Values in Table 2.1 represent empirical data for healthy brain and alter for example under stress, inflammation or hypoxia.

Table 2.1: Typical perfusion parameter values in healthy brain: cerebral blood volume (CBV) in % or ml/100 g, cerebral blood flow (CBF) in ml/100 g/min and mean transit time (MTT) in s. [+] [30], * [28]

	gray matter[+]	white matter[+]	normal brain[*]
CBV	5.2 ± 1.2	2.7 ± 0.5	4.0
CBF	55.0 ± 12.0	22.0 ± 5.0	50.0
MTT	5.6 ± 2.0	7.2 ± 3.0	6.0

2.3.2 Imaging Perfusion: Pharmacokinetic Modeling and Curve Characterization

Since the 1980s, it is possible to image hemodynamic parameters [31]. The first techniques were xenon-enhanced computed tomography (XeCT) and PET. With technical improvement, also single photon emission computer tomography (SPECT), MRI and dynamic perfusion CT (PCT) became reliable for perfusion imaging [31, 32]. All these techniques need a specially labeled imaging agent for visualization. The underlying technology determines the kind of labeling. For PET imaging the injection of a positron-emitting radionuclide (^{18}Fluor, ^{15}Oxygen) is necessary. In MRI the injected agent contains paramagnetic (gadolinium) or superparamagnetic (iron oxide) particles. An alternative is arterial spin labeling, where the blood water is used as an endogenous tracer that is magnetically labeled using radiofrequency pulses [33]. Even though in

principle the image analysis is similar for all techniques, this work focuses on dynamic methods using MRI and PET.

In biochemical and physiological imaging the aim of labeling is to have an agent that behaves metabolically equivalent to the unlabeled substance. The agent's physical and biochemical properties, as size, coating, bonding behavior or metabolization, define its distribution volume in tissue. In the case of perfusion imaging, two types of agents are commonly used: mainly diffusible (e.g. labeled water) and mainly intravascular agents (e.g. superparamagnetic iron oxide particles).

Freely diffusible tracers distribute homogeneously over the complete tissue volume, taking some time until blood and tissue concentrations reach equilibrium. During this time, the concentration is mainly determined by the delivered arterial tracer concentration, which is proportional to the CBF. Contrary, a completely intravascular tracer only distributes within vessels with a fast venous clearance. In this case, the concentration of the tracer is primarily determined by the distribution volume, which allows a robust measurement of CBV. In fact, mixed forms are typically present [28].

The theory of tracer kinetics includes plenty of models. Most of them define the tissue as a combination of individual subsystems, called compartments [34]. A general description of the tracer distribution in tissue (concentration over time) can be mathematically expressed by a convolution:

$$C_{tis} = \int_0^t CBF\ C_p(t')\ R(t-t')dt' = CBF \cdot C_p(t) * R(t) \qquad \textbf{(2.7)}$$

This relation between the arterial input of the tracer, determined as concentration in blood plasma (C_p), and the tissue concentration (C_{tis}) is only valid if the blood flow (CBF) is constant over time and each molecule of the agent has the same possibility to distribute over the volume at time t [28]. All kinetic properties of the agent are condensed in the residue function $R(t)$. This function describes the probability that a molecule of the agent that entered the voxel at time $t = 0$ is still there at time $t = t'$. Figure 2.5 shows ideal residue functions of three possible tracer behaviors, which are described in the following. One common kinetic model is the two-compartment model that consists of one vessel and one tissue compartment. Therefore, it is often referred to as one-tissue compartment model. Within each compartment, the contrast agent (CA) is assumed to be freely diffusible. This absence of spatial concentration gradients specifies a well-mixed compartment and the corresponding residue function is represented by the dotted curve in Figure 2.5 [34].

An alternative to the standard two-compartment model is the tissue homogeneity model [35]. It adopts the EES as a compartment and assumes validity of the plug-flow model within the capillary bed. The main difference between compartment and plug-flow models lies in the concentration evolution of the agent. In compartments the

concentration changes over time and is uniform over the volume. Using a plug-flow model, an additional concentration gradient along the capillaries is allowed. The adiabatic approximation of the tissue homogeneity model [36] assumes a slow change of the EES concentration relative to the fast change of concentration in the intravascular space. It approximates the tissue homogeneity model best for weakly vascularized or slow indicator exchange regimes and allows a separation of the dynamic time course in a fast vascular phase and a slow extravasation phase [13, 37]. For intravascular tracers modeled with plug-flow, all tracer particles have identical velocity and trajectories through the capillaries. Hence, only a single transit time exists and the residue function is represented by a box (solid line, Figure 2.5). The capillary transit time T_c therefore equals the MTT. If the capillary bed allows multiple transit times, $R(t)$ behaves like the dashed curve [28].

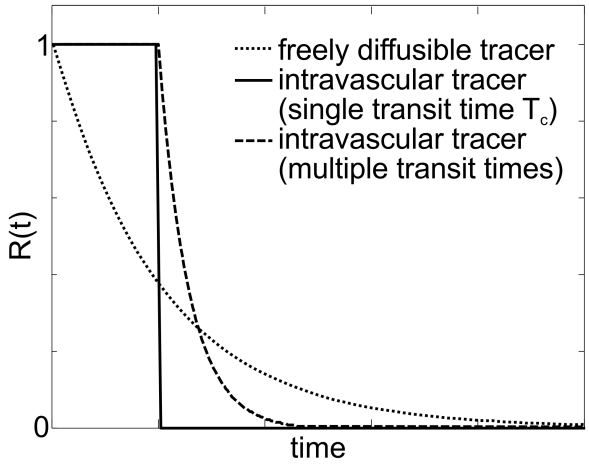

Figure 2.5: Ideal residue functions R(t) for three different systems: freely diffusible agent and intravascular agent with a single and multiple capillary transit times.

For all of these models, the relation between the MTT of the agent and $R(t)$ is given by [37]:

$$MTT = \int_0^\infty R(t)dt \tag{2.8}$$

In PET, common tracers for perfusion quantification are ^{15}O, $C^{15}O_2$ and $H_2{}^{15}O$. They are freely diffusible and allow quantification of CBF using two-compartment models [34, 38]. Most other tracers have a specific binding mechanism or metabolism behavior. Using a suitable model assumption, the vascular space, i.e. CBV, is included as a fitting parameter. In the simplest form, CBV is the ratio between C_{tis} and C_p at equilibrium. This ratio specifies the volume of blood that contains the same activity as 1 ml of tissue [38].

For intravascular tracers, e.g. MRI contrast agents in brain, the distribution volume can be assumed equivalent to the blood volume. Combining the central volume principle (Eq. (2.6)), Eq. (2.7) and Eq. (2.8) it follows [28]:

$$CBV = \frac{\int_0^\infty C_{tis}(t)\,dt}{\int_0^\infty C_p(t)\,dt} \tag{2.9}$$

This equation holds under the assumption of a fast bolus injection, whereby the concentration rapidly reaches zero level after the first passage of CA through the vasculature.

In reality, for bolus experiments a second peak, the recirculation term, follows. This recirculation is partly caused by the second passage of CA through the brain. The greater contribution to this phenomenon is due to CA that first circulates through kidneys, thyroids and lymph nodes before it reaches the brain [39]. The recirculation term can confound the determination of perfusion parameters, especially if acquisition time is short. However, because the effect is the same in the arterial input and the tissue, its impact on CBV should be small [40]. More problematic is the definition of the arterial input function (AIF). Imaging specific problems (partial volume effects (PVE), selection of appropriate voxels) and problems due to physiological properties (dispersion or delay between arteries and regional tissue) make perfusion estimation complex. To avoid AIFs, reference region models [38, 41] or summary parameters can be used as alternatives [42]. Using a bolus injection, signal-time curves of the first pass of the tracer allow a rather simple extraction of curve shape characteristics (summary parameters). Such parameters are the time-to-peak (TTP), peak height, arrival time and washout or signal recovery. Their stability enables a fast assessment of perfusion abnormalities, i.e. delayed perfusion via TTP. Widely used in MRI is the area under the curve (AUC). Under the assumption that the area of the AIF is constant for all voxels, a direct proportionality to CBV exists. However, an absolute quantification of hemodynamic parameters is impossible without an AIF.

The advantage of PET is the possibility to convert signal (decays per second) directly to absolute concentration. In MRI several indirect mechanisms contribute to the signal complicating the conversion of signal to concentration and thus absolute quantification (section 2.4).

2.4 Signal Contrasts in MR Imaging

Tissue properties (intrinsic factors) and acquisition parameters (extrinsic factors) together determine the contrast in MR images. Basic intrinsic tissue properties are the proton density and the relaxation times T1 and T2 (section 2.1.3). Furthermore, effects of magnetic susceptibility, flow and diffusion control the contrast between tissues.

2.4.1 Impact of Sequence Design

The actual image contrast between tissues with different properties is determined by the field strength and pulse sequence. Figure 2.6 shows the relaxation behavior of three tissue types. Depending on the progression of relaxation during a defined time, the image is more T1-, T2- or proton density-weighted. The MR signal is always proportional to the proton density. By modifying echo time (TE), repetition time (TR) and flip angle (FA) the initial contrast can be adapted. The impact on the contrast is sequence specific. Generally, the following rules exist for SE and GE experiments. A T1-weighted image is achieved by reducing TE (TE << T2) and TR. This suppresses T2/T2*-weighting and enhances T1-weighting. The other way around, a T2/T2*-weighted image features long TE and long TR (TR >> T1). If T2/T2*- and T1-weighting is suppressed (short TE, long TR) the image is proton density-weighted. For GE experiments, further the interaction of TR and FA is important [25, 28]. With larger flip angles the T1-weighting increases. The shorter the TRs, the smaller the FAs that already result in predominantly T1-weighted images. With increasing field strength, the transversal relaxation times (T2/T2*) decrease and T1 increases. Hence, the contrast changes with field strength for identical sequence parameters.

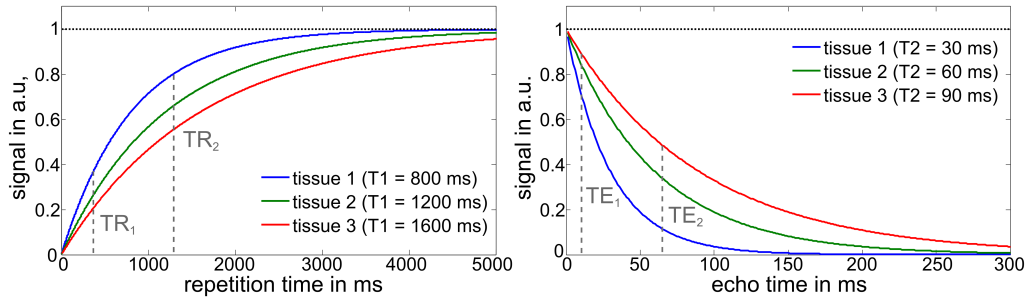

Figure 2.6: Spin echo signal changes depending on T1 and T2 relaxation for three different tissues. Change in T1 contrast for different TRs (left) and change in T2 contrast for different TEs (right).

For high quality, anatomical brain images, a Turbo-FLASH (Fast Low Angle Shot) [43] GE sequence can be acquired. As the name implies low flip angles and short TRs are used to accelerate imaging. The T1 contrast can be enhanced, when an inversion pulse (180°) is introduced a certain time before the excitation pulse. With an appropriate time delay, the desired T1-weighting can be generated. A 3D variant of this sequence is the MP-RAGE (Magnetization Prepared Rapid Gradient Echo). A common neuroimaging sequence based on SE imaging is the Fluid-attenuated inversion recovery (FLAIR) sequence. In these T2-weigthed images the signal of cerebrospinal fluid (CSF) is suppressed. Again, this is obtained with an inversion pre-pulse and an inversion time of about 70 % of the T1 in CSF [25].

2.4.2 Magnetic Susceptibility

The magnetic susceptibility χ describes to which extent a tissue becomes magnetized due to the influence of an external magnetic field $\boldsymbol{B}$ [28, 44]:

$$\chi = \frac{\mu \boldsymbol{M}}{\boldsymbol{B}} \tag{2.10}$$

Here, $\boldsymbol{M}$ denotes the magnetization and μ the magnetic permeability of the tissue. The susceptibility depends on the arrangement of electrons within this tissue. Substances with an even number of electrons exhibit a negative susceptibility and are referred to as diamagnetic. Most tissues in body are diamagnetic with a weak magnetic susceptibility. Dense bone and air have almost zero susceptibility. Paramagnetic substances are characterized by at least one unpaired electron. They have a stronger, positive susceptibility and produce a magnetic field in direction of the applied field. This field, generated by the magnetized material itself, is additive to $\boldsymbol{B_0}$ and locally increases the net field inside the material. In MRI most external contrast agents (gadolinium) as well as deoxygenated hemoglobin (iron-containing metalloprotein of red blood cells) are paramagnetic. The third group, ferromagnetic material (e.g. metal alloys), is not important for tissue contrast. When placed in an external field it experiences a large force and stays magnetized after removing the outer field. However, if the size of ferromagnetic particles is reduced below a critical value, the material becomes superparamagnetic. Examples in medical imaging are contrast agents based on iron oxide and endogenous ferritin. Their properties are similar to the properties of paramagnetic materials but with a much higher susceptibility.

Even though the susceptibility differences between distinct tissues are small, they are sufficient to introduce local magnetic field gradients and thus accelerate the dephasing between protons of both tissues. In some regions, for example around the nasal cavity, this can introduce macroscopic field inhomogeneities, which lead to signal loss and image distortions. However, if inhomogeneities appear at a micro- or mesoscopic scale, they can be used to identify bleedings and measure changes in the blood oxygenation level.

2.4.3 Susceptibility Differences of Blood and Tissue

In the previous section (2.4.2) it was mentioned that most biological tissues are diamagnetic, while deoxygenated blood is paramagnetic. This difference creates magnetic field gradients between blood and tissue and introduces signal dephasing around venous vessels. Completely oxygenated blood is also diamagnetic, but with a slightly different susceptibility than tissue [45]. In blood, the red blood cells (RBCs) are responsible for the susceptibility difference. The volume fraction of RBCs in blood is termed hematocrit level (Hct). RBCs are mainly composed of the oxygen transporting protein hemoglobin.

The blood oxygenation level dependent (BOLD) susceptibility difference is a consequence of the oxygen binding to hemoglobin that reduces the unpaired electrons of the complex. The maximum susceptibility difference between fully oxygenated and fully deoxygenated blood is termed $\Delta\chi_0$. Because partly deoxygenated blood is typically present in venous vessels, the oxygen saturation Y determines the actual susceptibility difference. This means that the magnetic susceptibility within blood χ_{blood} is not homogeneous, but arises from different susceptibilities of individual blood compartments (χ_{plasma}, χ_{RBC}) [45]:

$$\Delta\chi_{vessel} = \chi_{blood} - \chi_{tissue} = \Delta\chi_0 \,\mathrm{Hct}\,(1 - Y) \tag{2.11}$$

These susceptibility differences introduce magnetic field inhomogeneities within (intravascular) and around vessels (extravascular). The differences inside blood $\Delta\chi_{blood}$ or tissue are generally neglected for the determination of the resulting field disturbances and the accompanying shift in Larmor frequency ($\Delta\boldsymbol{\omega}$). Thus, for an infinitely long cylinder with radius R, representing the vessel, $\Delta\boldsymbol{\omega}$ is given by [45]:

$$\Delta\boldsymbol{\omega_{in}} = \gamma \boldsymbol{B_0} \Delta\chi_{vessel} \left(\cos^2\theta - \frac{1}{3}\right) \tag{2.12}$$

$$\Delta\boldsymbol{\omega_{ex}} = \gamma \boldsymbol{B_0} \Delta\chi_{vessel} \left(\frac{R}{r}\right)^2 \sin^2\theta \cos 2\phi \tag{2.13}$$

Depending on the observation point r, $\Delta\boldsymbol{\omega}$ is computed for intra- ($\Delta\boldsymbol{\omega_{in}}$) and extravascular ($\Delta\boldsymbol{\omega_{ex}}$) conditions. The azimuthal angle ϕ is the angle between the observation point and a plane orthogonal to the cylinder axis. Around vessels, the scale of these mesoscopic susceptibility effects further depends on the vessel size compared to the water diffusion length and the vessel direction (θ) with respect to the main magnetic field ($\boldsymbol{B_0}$). Around venous vessels, oriented orthogonally to $\boldsymbol{B_0}$, this can affect distances up to five times the vessel radius [10].

In imaging, susceptibility effects result in a reduction of T2* (faster dephasing). Hence, the signal in a voxel containing blood and tissue in T2*/T2-weighted images is directly correlated with the oxygenation level. This relationship is the origin of the BOLD effect. One way to use this BOLD effect is to image the OEF. The OEF allows to estimate how much of the delivered oxygen is metabolized by the tissue cells. If the arterial oxygen saturation is 100 %, OEF equals 1-Y. The extent of the BOLD susceptibility effect depends also on the total amount of deoxyhemoglobin in the voxel. Therefore, the deoxygenated blood volume (dCBV) and Hct in the voxel will strongly influence

conclusions about the oxygenation level. A clinically applicable method to measure an apparent OEF is described in section 3.5.

2.5 Mechanism of Action of MR Contrast Agents

2.5.1 General Effect on Relaxation

The most widely used MR contrast agents are gadolinium-based complexes. Gadolinium has seven unpaired electrons and therefore shows a strong paramagnetic effect. In the immediate vicinity of the contrast agent, T1 and T2 are shortened due to a direct interaction between the water protons and the fluctuating local magnetic field generated by the unpaired electrons of gadolinium (dipole-dipole interactions). The strong paramagnetic effect of the gadolinium ion affects the directly coordinated water protons and the bulk water in the near environment of the complex. Due to diffusion, affected protons interchange with others and consequently effect T1 and T2 shortening in a larger distance to the agent [46]. The efficiency of these processes depends on the number of water molecules in direct interaction with the agent (hydration number), the exchange rate between water protons directly interacting with the agent and its molecular tumbling. Long rotational correlation times and fast water exchange relate to a higher efficiency of the agent.

To quantify the relaxation efficiency, it is useful to deal with relaxation rates, i.e. reciprocal values of relaxation times. The change in relaxation rate in dependence on the concentration of the contrast agent (C_{CA}) is specified by its relaxivity r_i:

$$\frac{1}{T_i} = \frac{1}{T_{i0}} + r_i C_{CA}, \quad i = 1,2 \tag{2.14}$$

Here $1/T_i$ $(= R_i)$ is the relaxation rate with CA and $1/T_{i0}$ the relaxation rate in absence of CA. Equation (2.14) assumes a linear relationship between CA concentration and relaxation rate. For typical ΔR1 this is satisfied for a fast water exchange (exchange rate < ΔR1). This means all water protons have equal and unrestricted access to the CA. In reality, biological tissue consists of different compartments. If water moves fast between the compartments, CA acts as if it is uniformly distributed over the volume of interest. This assumption is applicable within blood [47, 48]. In tissue, an intermediate water exchange is more probable, resulting in a multi-exponential relaxation behavior (depending on the number of biological compartments). For ΔR2*, susceptibility effects additionally alter the relaxation behavior similar to the BOLD effect. In tissue, the relationship between CA concentration and ΔR2* was found to be reasonably linear [49], but this is not true in blood. For higher CA concentrations in blood, gadopentetat

dimeglumin (Gd-DTPA) follows a quadratic [49] and gadofosveset trisodium a parabolic relaxivity behavior [47]:

$$\Delta R2^* = q_2 {C_{CA}}^2 + r_2 C_{CA} \quad \textbf{(2.15)}$$

$$\Delta R2^* = q_2 {C_{CA}}^2 + r_2 C_{CA} + s_2 \quad \textbf{(2.16)}$$

The parameters q_2, r_2, s_2 are empirically determined, field strength dependent constants [47, 49].

For clinical doses, paramagnetic contrast agents predominantly lead to a T1 enhancement in T1-weighted images. Although the absolute relaxation related changes caused by contrast agents are comparable for both relaxation rates, the percentage effect is much smaller for R2. The reason is the large difference between typical tissue relaxation rates (R1 << R2). When the concentration of the paramagnetic agent exceeds a particular value, the effect on T2 dominates the T1 effect and the signal decreases. This particular concentration depends on initial tissue relaxation rates and sequence parameters. In T1-weighted images (short TR), a T2 dominated contrast occurs for concentrations larger than about 10 mmol/kg. In T2/T2* weighted images (long TE, large TR), the T1 effect is already saturated, and susceptibility effects become more important, resulting in an immediate signal loss [25, 50].

2.5.2 Contrast Agents in Brain: Advantages and Drawbacks

A special feature of the vasculature in brain is the blood-brain-barrier (BBB). Therefore, most of MRI CAs stay intravascular. This causes three effects. First, the distribution volume of CA is rather small, only about 4 % of the brain [28]. Second, the water exchange between vascular space and EES is slow (exchange rate ~ 1 s^{-1}) compared to typical measurement times (TE) and can be neglected. Following, a direct interaction of gadolinium and water over dipole-dipole interactions is restricted to the vascular space causing the third point: locally limited T1 enhancement. Thus, in brain tissue T1-related signal changes due to contrast agent are rather small, because T1 effects are essentially restricted to blood. However, similar to deoxygenated blood, intravascular paramagnetic contrast agents can introduce a susceptibility contrast, but with a much larger effect. In and around vessels the magnetic field gradients lead to enhanced T2* relaxation within a mesoscopic scale. This susceptibility-related contrast is used in T2*-weighted bolus-based perfusion imaging and termed dynamic susceptibility contrast (DSC), which is explained in detail in section 3.1.

In brain lesions with disrupted BBB (tumors, stroke), gadolinium can distribute over the EES. This phenomenon is known as extravasation or leakage. In EES the CA causes a shortening of T1, T2 and T2* due to direct interactions with tissue water. T2* is further reduced because susceptibility differences between EES and vessels or intracellular spaces introduce additional mesoscopic magnetic field gradients. The signal loss due to CA, therefore, depends on the tissue structure [51]. The impact of susceptibility effects (T2*) decreases with reduced cell size, increased cell density and increased initial T1 of the tissue. The impact of both effects (direct interaction, susceptibility effect) on signal also depends on the type of sequence (GE, SE) as well as acquisition parameters (TR, TE, flip angle) and field strength. Generally, the extent of T2* effects (mainly susceptibility related) increases while that of T1 effects (based on direct interaction) decreases with increasing field strength, TR and TE and decreasing FA. In T1-weighted images such as anatomical MP-RAGE and dynamic contrast enhanced (DCE) bolus perfusion imaging, the extravasation-accompanying increase in distribution volume leads mainly to a visible T1 enhancement (section 3.4). In T2*-weighted perfusion imaging using DSC, extravasation changes the signal according to the predominant relaxation effect (T1 or T2/T2*). While predominant T1 effects lead to a signal overshot after CA bolus passage, T2/T2* effects prevent the signal from returning to the baseline. Therefore, results of perfusion imaging are highly variable and depend on tissue properties as well as acquisition techniques.

3 Materials and Methods

3.1 Quantification of Perfusion with DSC-MRI

Dynamic susceptibility contrast (DSC) magnetic resonance imaging allows perfusion measurements by tracking a bolus of intravascular contrast agent (CA) during its passage through the vascular system. The paramagnetic CA introduces local magnetic field inhomogeneities in and around blood vessels, leading to a T2* shortening. With the aid of fast T2 or T2*-weighted imaging, a signal drop is noticeable over circulation time (chapter 2.5.2).

3.1.1 Summary Parameters

As mentioned in chapter 2.3.2, stable, perfusion related measures can be obtained via summary parameters. Figure 3.1 shows a typical concentration-time curve (CTC) including the definition of evaluated parameters.

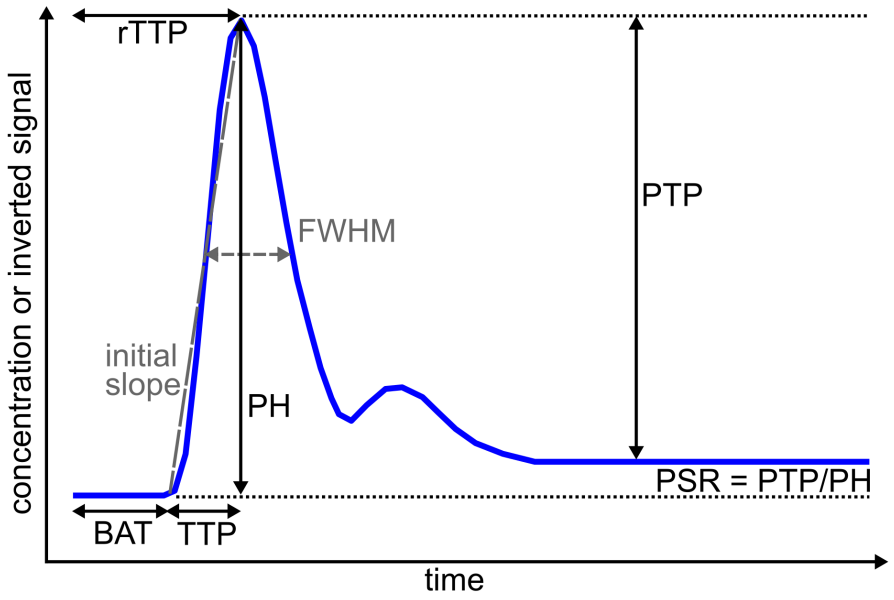

Figure 3.1: Definition of summary parameters. rTTP = relative time-to-peak, TTP = time-to-peak, BAT = bolus arrival time, FWHM = full width at half maximum, PH = peak height, PTP = peak-to-post bolus signal and PSR = percentage signal recovery calculated by PTP/PH. The dotted lines represent baseline (bottom) and peak (top) signal or concentration.

Especially in stroke patients a fast diagnosis and treatment are highly important for patient outcome [52]. Therefore, time to peak (TTP) maps, which indicate delayed perfusion and correlate with hypoperfusion [53], can be used for a quick evaluation. In

patients with other brain lesions, e.g. tumors, relative peak height (rPH) and relative percentage signal recovery (rPSR) are more interesting. rPH was shown to correlate with relative CBV and the capillary blood volume and allows to distinguish between radiation necrosis and recurrent tumor [54]. A potential indicator for vascular permeability in interaction with cell size and cell volume fraction is rPSR [55]. It enables a distinction between metastasis, lymphoma and high-grade glioma, where these physiological properties differ. Both, rPH and rPSR, are calculated from the signal (Figure 3.1). The 'r' indicates the ratio between the values of the actual tissue curve and that of a healthy white matter curve [11]. Further, bolus arrival times (BAT) can give suggestions on perfusion abnormalities or can serve as a correction factor to account for tracer delays (chapter 3.2.2). Most of these parameters are used to select and evaluate the quality of an AIF from the perfusion images, including full width at half maximum (FWHM) and initial slope. The latter one is none of the common AIF criteria. However, in [42] it was found to be one of the most important shape characteristics.
Even though these parameters are useful in finding perfusion abnormalities within one patient, most of the values are individual for each person. Thus, the use of summary parameters to quantify perfusion should be handled with care [56].

3.1.2 CBV Estimation Using intravascular Contrast Agents

One of the most important and critical steps in CBV quantitation is the transformation of MR signal into CA concentration. In order to achieve this, first, the signal is converted to a concentration (C) dependent change of the effective transverse relaxation rate $\Delta R2^*$:

$$C(t) \propto \Delta R2^*(t) = -\frac{1}{TE}\ln\left(\frac{S(t)}{S(0)}\right) \tag{3.1}$$

In tissue and for sufficiently small CA concentrations $\Delta R2^*$ should be proportional to the concentration [49]. From the known proportionality between CBV and concentration integral (Eq. (2.9)) it follows:

$$\text{CBV} \propto \int_0^\infty \Delta R2^*(t)dt \tag{3.2}$$

This relationship allows relative measurements of CBV. Absolute quantitation additionally requires determination of an arterial input function (Eq. (2.7)), a valid relation between concentration and transverse relaxation rate change and the hematocrit level (Hct) (chapter 2.5.1). In this work, voxels for an AIF were automatically selected with a method based on singular value decomposition, described in sections 3.3.2 and 3.3.4. Because the conversion of $\Delta R2^*$ to concentration is non-linear for pure blood and high CA concentrations (chapter 2.5.1), AIF voxels were selected in tissue near arterial

vessels as recommended by [57] and explained in section 3.3. Therefore, CA concentrations of tissue (C_{tis}) and blood plasma (C_p) were calculated assuming a linear dose dependence. The relaxivities were set to r_2 = 0.0053 ms^{-1} mM^{-1} for Gd-DTPA [48] and r_2 = 0.0915 ms^{-1} mM^{-1} for gadofosveset trisodium [47]. Because the agent only distributes over the blood plasma volume, a correction factor k_H was further introduced to account for the volume occupied by RBCs [58]:

$$k_H = \frac{1 - Hct_{large}}{\rho(1 - Hct_{small})} \tag{3.3}$$

Here Hct_{large} and Hct_{small} is the hematocrit in large and small vessels, respectively, and ρ is the tissue mass density. Since Hct could not be measured in this study, a common value of $k_H = 0.733/(1.04\ \mathrm{g\ cm^{-3}})$ was used [58]. According to the theory of tracer kinetics described in chapter 2.3.2, absolute CBVs in this work were calculated in two ways:

(1) by simply integrating the ratio of the CA concentration time courses in tissue and blood plasma:

$$CBV_{unc\,1} = k_H \int_{t1}^{t2} \left(\frac{C_{tis}(t)}{C_p(t)} \right) dt \tag{3.4}$$

(2) by deconvolution of the tissue CTCs with the arterial input function, and subsequent integration of the resulting impulse response function $H(t)$:

$$CBV_{unc\,2} = k_H \int_{t1}^{t2} H(t)dt \tag{3.5}$$

$$H(t) = f \cdot R(t) \tag{3.6}$$

where f is the initial amplitude of the impulse response, $k_H \cdot f$ specifies the hematocrit corrected blood flow and $R(t)$ the residue function. Please note, the subscript 'unc', i.e. uncorrected, refers to the fact that the calculated CBV values may be biased in the presence of contrast agent leakage (section 3.1.3).

In both cases, the integration intervals ($t1, t2$) were set automatically and identical for all voxels of one patient. Because in theory the assumptions for CBV calculation are only valid for the first pass of the CA bolus without recirculation (section 2.3.2), but currently a 120 s integration is recommended [55], two integration intervals were used and the results were analyzed. The lower integration interval $t1$ was fixed at one time point, shortly before the signal of the averaged tissue curve drops. The upper integration level $t2$ was set once to the end of acquisition (full integration) and once to the end of the first

pass of the averaged tissue curve (first pass integration). Both are common techniques, but in terms of absolute quantification potentially introduce differences [59].
Because the conversion of MR signal to CA concentration is critical due to distortions and PVEs (section 3.3) and no individual hematocrit levels were measured, all CBVs were additionally normalized. For this purpose, we assumed that CBV of healthy white matter is 1.5 % [60, 61].

3.1.3 Effects of Contrast Agent Extravasation on CBV Estimates

The extravasation of CA violates one of the basic assumptions of CBV quantitation, namely that of the agent being a purely intravascular tracer. In addition, it changes the signal evolution during the bolus passage as stated in section 2.5.2, introducing errors in CBV calculation. Figure 3.2 shows a typical signal behavior without and with T1- and T2/T2*-based leakage effects.

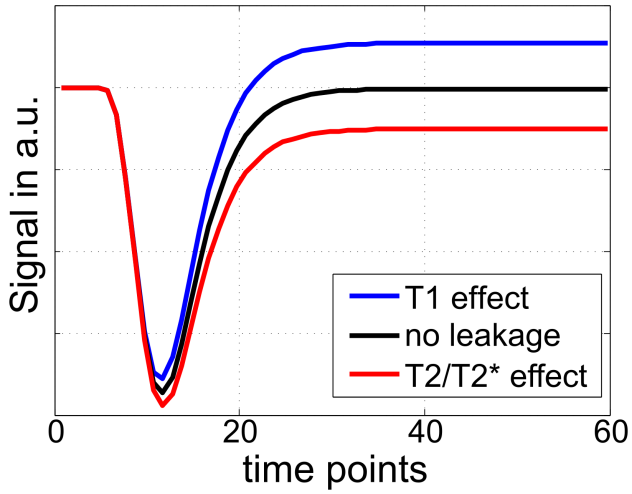

Figure 3.2: Effect of contrast agent extravasation on signal behavior during a DSC bolus experiment. In the ideal fast bolus experiment, the signal rapidly returns to baseline after the initial signal drop during the first pass of the CA (black). T1 effects lead to a signal overshoot (blue) after the first pass, while the signal confounded by T2/T2* effects (red) does not return to baseline.

Depending on the dominating contrast effect either an under- or overestimation of CBV occurs. Predominant T1 effects (reduced post-bolus $\Delta R2^*$) decrease the area under the $\Delta R2^*$ time course, leading to a CBV underestimation (Eq. (3.2)). If T2/T2* effects (enhanced post-bolus $\Delta R2^*$) prevail, CBV is overestimated. The degree and direction of those leakage-based signal alterations depend on tissue geometry [51] and sequence parameters [62], as described in section 2.5.2.

Due to CA extravasation, CBV estimates are biased and the examination of tumor grade, the distinction between brain lesion types as well as rOEF measurements are directly affected. To address this problem, several correction possibilities exist. In this thesis, the most frequently used methods were implemented, analyzed, extended and optimized to establish a fast and robust clinical analysis tool.

3.2 Extravasation Correction for DSC-based CBV Measurements

3.2.1 Pre-bolus Technique

One common method to reduce predominant T1 leakage effects in DSC is the pre-bolus (PB) acquisition scheme [19] using an initial pre-dose of CA to saturate the tissue. Consequently, the initial tissue T1 (T10) and the concentration gradient between blood plasma and EES are reduced. During a second CA bolus, the DSC perfusion images are acquired. This technique leads to an efficient reduction of T1-related leakage effects. However, the T2/T2*-based effects of contrast agent extravasation become more prominent [63, 64] and a higher CA dose is necessary.

3.2.2 Post-processing Techniques

To account not only for T1 effects, but also for the counteracting T2/T2*-effects, four post-processing models with a maximum of three free parameters were implemented and evaluated in MATLAB R2013a (MathWorks, Natick, US).

Method I: In the approach of Weisskoff et al. [65], later elaborated by Boxerman et al. [12], it is assumed that $\Delta R2^*$ in tissue with intact BBB is proportional to the average concentration of CA in vessels. Accordingly, the voxel-wisely measured $\Delta R2^*(t)$ is expressed by a linear combination of the relaxivity due to T2/T2* (first term) and T1 (second term) dominated effects as a function of the mean time course $\overline{\Delta R2^*(t)}$ over all voxels belonging to healthy appearing tissue (reference curve) [12],

$$\Delta R2^*(t) \approx K_1 \, \overline{\Delta R2^*(t)} - K_2 \int_0^t \overline{\Delta R2^*(\tau)} \, d\tau \qquad (3.7)$$

where K_1 is a susceptibility scaling factor and K_2 a permeability related parameter. In this work, the reference curve was calculated by averaging all voxels within the whole brain mask subtracted by CSF and diseased tissue regions (section 3.7.2). K_2 is obtained from a linear least-square fit of Eq. (3.7) to the measured $\Delta R2^*$ and is then used to calculate a corrected relaxation curve $\Delta R2^*_{corr}$ for each voxel:

$$\Delta R2^*_{corr}(t) = \Delta R2^*(t) + K_2 \int_0^t \overline{\Delta R2^*(\tau)}\, d\tau. \quad (3.8)$$

To account for both extravasation effects (chapter 3.1.3), the parameter K_2 was allowed to become positive and negative. The parameter K_1 was not considered further.
This approach neglects back-diffusion of CA to the vessels, assumes a fast water exchange, small T1-based enhancement (< 30 %) and comparable MTT in healthy and diseased tissue. This means that $\Delta R2^*$ in diseased tissue is considered a scaled version of that in healthy tissue. In most pathologies this assumption does not hold true [13, 16] and the fit returns wrong values.
Method II: To account for tissue-specific MTT variations, Leigh et al. [16] extended method I by introducing a time offset b and a temporal scaling factor c, as well as a magnitude scaling factor a, alternatively to K_1:

$$\Delta R2^*(t) \approx \overline{a\, \Delta R2^*\left(\frac{t+b}{c}\right)} - K_2 \int_0^t \overline{a\, \Delta R2^*\left(\frac{\tau+b}{c}\right)}\, d\tau. \quad (3.9)$$

Using this equation, a set of modified reference curves ($\overline{a\, \Delta R2^*((t+b)/c)}$) was calculated for a predefined range of physiologically reasonable values of the three parameters. The smallest sum of the squared differences between the numerous reference curves and the measured data determined the most appropriate parameters.
For both approaches, the leakage corrected CBV ($CBV_{method\ I}$, $CBV_{method\ II}$) is usually obtained according to Eq. (3.4) using $\Delta R2^*_{corr}(t)$ instead of $\Delta R2^*(t)$ for calculation of concentration. The literature recommends an integration over 120 time points [55]. In this study, two limits were tested as described in section 3.1.1, to analyze the differences between first pass (CBV_{fp}) and full integration (CBV_{full}) interval.
Method III: Bjørnerud et al. [13] developed a method based on the adiabatic approximation of the tissue homogeneity model [36] (chapter 2.3.2) using the convolution theorem (Eq. (2.7)) to calculate a flow- and extravasation-weighted impulse response $H(t)$ [13]:

$$H(t) \approx \begin{cases} f\, R(t), & 0 \le t < T_c \\ K^{trans}\, e^{\left(-\frac{K^{trans}(t-T_c)}{v_e}\right)}, & t \ge T_c \end{cases} \quad (3.10)$$

Here, t is the imaging time, f is proportional to blood flow, $R(t)$ is the residue function, v_e the EES volume and K^{trans} the transfer constant, characterizing CA leakage. Determined by the capillary transit time T_c, which is equivalent to the MTT for the plug-flow model, Eq. (3.10) discerns two cases, the early perfusion dominated phase and the late extravasation dominated phase of the CA distribution. When Eq. (3.10) is

written in matrix notation [13], the system of linear equations can be solved by singular value decomposition (SVD), where the $\Delta R2^*$ of tissue and the image-derived AIF (IDAIF) serve as initial parameters. T_c can be obtained by fitting the first portion of $R(t)$ with a Lorentzian function [13]:

$$R(t) = \left[1 + \left(\frac{\pi\, t}{2\, T_c}\right)^2\right]^{-1} \tag{3.11}$$

For later dynamic images (t >> T_c) the extravasation effect dominates the impulse response [13] and allows to derive extravasation related parameters. Because the extravascular CA changes the signal behavior, an apparent transfer rate K_2, that includes T1 and T2/T2* leakage effects, is measured rather than K^{trans} [13]. When a limited reflux ($K^{trans}/v_e \rightarrow 0$) is assumed during the measurement time, Eq. (3.10) can be simplified to $H(t) \approx K_2$ for t >> T_c. In the original work of Bjørnerud et al. [13] K_2 was thus obtained by averaging $H(t)$ between $t = T_c$ and the end of the measurement time. Since own simulation outcomes (section 3.6) indicated optimal results for K_2, when the values of $H(t)$ were averaged between $t = 8\, T_c$ and the end of the measurement time, this range was averaged in the actual implementation. If the averaging interval fell below a minimum of ten time points, the starting time was shifted to earlier time points accordingly. The corrected blood volume $CBV_{\text{method III}}$ was then calculated according to [13]:

$$CBV_{method\ III} = CBV_{unc\,2} - \left(k_H\, K_2\, \Delta t\, (N - N_c)\right) \tag{3.12}$$

with the sampling interval Δt, the number of acquisitions N and the time index N_c corresponding to the capillary transit time. The uncorrected CBV ($CBV_{\text{unc 2}}$) was calculated per Eq. (3.5). Finally, the MTT was determined by numerical integration of the residue function $R(t)$ over the whole scan time (tracer dilution theory) [66], and the CBF was obtained by multiplication of the maximum amplitude of $H(t)$ with k_H. For consistency with the other methods (where T1 effects have positive K_2) the sign of K_2 was inverted compared to [13]. Further, the leakage term includes k_H following from the derivation and being different to the original implementation, where only $1/\rho$ was used.
A known limitation of this approach is the sensitivity of the standard SVD algorithm to image noise [66]. In general, this sensitivity is reduced by regularization. In this work, for standard regularization (sSVD) a global, SNR (signal-to-noise ratio) dependent cut-off value as recommended in [67] was used. As an alternative, Tikhonov regularization (TiSVD) was applied. This should be less sensitive to MTT alterations [68, 69]. By using the L-curve criterion [69] to find the optimal regularization value, a trade-off could be

achieved between the size of the regularized solution and its fit to the given data. However, this algorithm is more time consuming and for initial tests the implemented Tikhonov regularization [69] was not sufficient. Hence, a combined regularization was done by applying a cut-off value to exclude the smallest value of the diagonal matrix before Tikhonov regularization.

Physiological conditions, acquisition schemes or technical implementations can delay or disperse the observed AIF against the perfect AIF. This confounds the SVD process and introduces additional oscillations. Therefore, an arrival time correction (ATC) was introduced for method III. This ATC method is described in detail in section 3.3.5.

Method IV: The fourth leakage correction method, which is based on the publication of Quarles et al. [17], represents a two-step approach. First, the residue function is calculated via SVD using an extended matrix notation of the tracer dilution theory [17]:

$$\Delta R2^*_{meas}(t_n) \approx \Delta t \sum_{i=1}^{M} C_p(t_{n-i}) R'(t_i) + \beta_2 I_p(t_n) \quad , with\ n = 1 \dots N \tag{3.13}$$

Here, Δt is the temporal resolution, $C_p(t_i)$ is the concentration of the AIF, $R'(t_i) \approx \beta_1 R(t)$ is the susceptibility scaled residue function, I_p is the cumulative sum of the IDAIF concentration, β_1 and β_2 reflect the initial estimates of the susceptibility and permeability weighting factors K_1 and K_2. M and N are the index number defining the end of the IDAIF and the number of temporal positions used for the fit of the voxel-wise $\Delta R2^*(t)$ curve, respectively. Then, convolution of the susceptibility scaled residue function $R'(t)$ with C_p facilitates a voxel-wise estimation of relaxation-time curves ($\Delta R2^*_{est}$). Instead of a global healthy tissue reference curve like in method I, these calculated $\Delta R2^*_{est}$ curves are used as voxel-wise fitting references. The estimation of leakage (K_2), the calculation of $\Delta R2^*_{corr}$ (Eq. (3.14)) and the calculation of CBV are equivalent to the procedure of method I.

$$\Delta R2^*_{corr}(t) = \Delta R2^*_{meas}(t) + K_2 \int_0^t \Delta R2^*_{est}(\tau)\, d\tau \tag{3.14}$$

3.3 Selection of the Image-derived Arterial Input Function

For quantitative perfusion imaging, a correct and stable estimate of an appropriate arterial input function is one of the most important requirements. Therefore, a central part of this work was to optimize the process of AIF selection. Throughout this thesis, a differentiation is made between the AIF, i.e. the real input function at a specific tissue voxel, and the IDAIF, the image-derived input function. A stable and correct estimate of

the real AIF is difficult to achieve because it could be different for each brain region or even each voxel. Therefore, separate, local IDAIFs determined from smaller arteries are partly recommended [70, 71]. If properly selected, they would better represent the true input of the microvasculature because they are situated closer to the capillary bed. Problems of this approach are the larger partial volume effect as pure blood voxels become more improbable [72] and the largely increased processing effort. The alternative is the selection of one global IDAIF in larger vessels. In this case, errors can be induced by an earlier, later, broader or narrower IDAIF in comparison to the real AIF of the corresponding tissue voxel. Earlier and narrower IDAIFs are possible if the tissue is far away from the large vessels so that the real tissue input of the CA bolus is delayed, dispersed or both after its way through the vasculature. Further, all shape deformations as well as scaling problems could arise from PVE [73]. Because of the limited spatial resolution of DSC-MRI, PVE are practically always present. Inside the artery the higher CA concentration reduces T2, and the phase of the MR signal is changed due to altered susceptibility differences. Also outside the artery, local magnetic field changes lead to dephasing and phase shifts. The phase evolutions are different in the vasculature and in tissue. An intersection of the complex signals due to PVE non-linearly alters the shape of the time curves. To avoid this problem, Bleeker et al. [57] suggest selecting global IDAIFs completely outside the middle cerebral artery. The optimal locations depend on the sequence used, whereby more usable voxels have been found for PRESTO and segmented EPI compared to single shot EPI (ssEPI) [57].
The majority of IDAIF selection procedures, either automatic or manual, consider the known characteristics of a perfect AIF: early BAT, early TTP and a large and narrow peak. This study tested the reproducibility of one manual and two automatic selection methods to define an automatic, reproducible and global IDAIF.

3.3.1 Manual Selection

The manual selection was supported by highlighting voxels with a small time-to-peak and a fast, strong and narrow signal drop on the coregistered T1-weighted post-contrast images. For each patient, voxels close to the basilar, internal carotid or middle cerebral arteries were chosen manually and averaged.

3.3.2 Selection of Suitable Relaxation Time Curves

For both automatic algorithms, the selection of initial suitable arterial-like relaxation time curves was identical. To find the most appropriate relaxation time curves, the original perfusion images were filtered.
First, five slices were selected. Using the whole brain mask, only the first five slices with a brain area larger than two-thirds of the area of the middle slice were included. This

criterion was found to reliably select the region where basilar, internal carotid and middle cerebral arteries can be discerned best, and it excludes lower slices with large susceptibility artifacts from the paranasal sinuses. Further, the masks that represent hyperintense regions in FLAIR and contrast-enhanced T1-weighted images were subtracted, excluding diseased tissue and large vessels. Because the passage of the contrast agent through the vessels also changes the MR signal in the direct vicinity of those vessels (if oriented ∦ $\boldsymbol{B_0}$), voxels outside arteries can be used to estimate IDAIFs [57]. Reasons to select IDAIF voxels outside arteries were the reduced distortion artifacts, the reduced chance for signal drop saturation and that a linear dose response between $\Delta R2^*$ and CA concentration can be assumed (section 2.5.1).

Artifacts due to PVE could be minimized with the approach proposed by Bleeker et al. [73]. The method is based on the theory that perfusion parameters can be estimated equally well from the first pass (fp) of the CA and the post-bolus steady-state (ss) concentrations of tissue (C_{tis}) and blood plasma (C_p):

$$CBV = \frac{\int_{start\ fp}^{end\ fp} \mathrm{C}_{tis}(t)dt}{\int_{start\ fp}^{end\ fp} \mathrm{C}_p(t)dt} = \frac{\mathrm{C}_{tis}(t_{ss})}{\mathrm{C}_p(t_{ss})} \tag{3.15}$$

The time t, when post-bolus equilibrium is reached, is denoted with t_{SS}. This equation is only valid if the CTCs are known. Under the assumption of a linear relation between signal and CA concentration and negligible leakage effects on the post-bolus signal, the relation between first pass and steady-state values holds true for $\Delta R2^*$, which yields:

$$\frac{\Delta R2^*_{tis}(t_{SS})}{\int_{start\ fp}^{end\ fp} \Delta R2^*_{tis}(t)dt} = \frac{\Delta R2^*_{aif}(t_{SS})}{\int_{start\ fp}^{end\ fp} \Delta R2^*_{aif}(t)dt} \tag{3.16}$$

$\Delta R2^*(t_{SS})$ was determined by averaging the last ten images of the time course. The ratio, further referred to as SS:AUC_{fp} (steady-state: area under first pass curve) was calculated for each voxel. The SS:AUC_{fp} of every voxel was compared to the mean SS:AUC_{fp} of gray matter (GM). In case of shape errors due to PVE and inside vessels where CA concentrations are higher, a non-linear behavior between signal and concentration occurs and thus the validity of Eq. (3.16) is not maintained [74, 75]. Thus, voxels with ratios outside the range of ± 20 % SS:AUC_{fp} of GM were excluded because they were considered to be located inside arteries or to be affected by PVE or leakage. Normal tissue voxels, unaffected by field perturbations due to the CA inside the vessels, were evaded by omitting time courses with AUC_{fp} < 90 % of the maximum AUC_{fp}. According to the study by Mouridsen et al. [70], voxels affected by physiological pulsation, signal distortions or PVE show irregular time curves. Therefore, also time

courses with a roughness factor (Eq. (3.17)) larger than 25 % were excluded. The roughness factor f_{rough} was calculated according to:

$$f_{rough}(n\Delta R2^*) = \int_0^T \left(n\Delta R2^{*\prime\prime}(t)\right)^2 dt, \tag{3.17}$$

after a normalization of all $\Delta R2^*$ curves to identical areas ($n\Delta R2^*$).
The resulting mask (see example in Figure 3.3) was applied to the parameter maps of BAT, TTP, peak height (PH), peak width (FWHM) and initial slope as well as to the temporal images of $\Delta R2^*$.

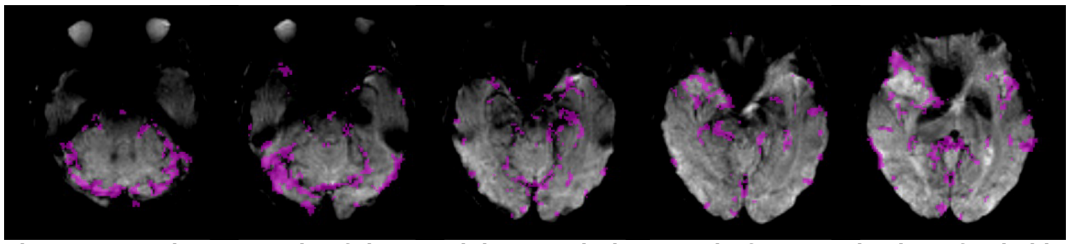

Figure 3.3: Patient example of the remaining voxels (magenta) after preselection of suitable relaxation time curves for IDAIF selection. Overlay on echo planar images at the maximum signal drop during CA bolus passage, thus vessels are dark.

3.3.3 Automatic IDAIF Selection Using Cluster Analysis

The five masked parameter maps (BAT, TTP, PH, FWHM, initial slope) were used for clustering, which was done in two steps. First, a clustering using a Gaussian mixture model (GMM) was done [76]. In initial simulations, clustering algorithms (k-means, fuzzy c-means, GMM, hierarchical, normalized cut) described in the literature [70, 77-79] were tested to find arterial voxels placed within a 32 × 32 matrix of time courses representing three different tissue types (chapter 3.6.1). Using noisy data (SNR ≈ 80), the GMM was found to be the best approach to identify arterial voxels. According to the literature [70], the number of clusters was always set to five. To detect the cluster which represents the best AIF, a quality factor Q, adapted from Mouridsen et al. [70], was maximized:

$$\mathrm{Q} = \frac{|\ln(PH)|}{(TTP \cdot FWHM \cdot BAT)} \tag{3.18}$$

The best cluster curve (largest Q) was checked against the normal appearing GM curve, comparing the individual parameters with each other ($BAT_{cluster} < BAT_{GM}$, $TTP_{cluster} < TTP_{GM}$, $FWHM_{cluster} < FWHM_{GM}$, $PH_{cluster} > PH_{GM}$). If the criteria for an AIF were not met, the clustering was redone up to five times, to account for the variability during the initialization of cluster centers. However, if still not all criteria were met, fewer criteria

were used ($TTP_{cluster} < TTP_{GM}$, $PH_{cluster} > PH_{GM}$). The best cluster was then used as input for a second clustering with a normalized cut algorithm [80, 81] to stabilize results. This algorithm is slower, but should be more reproducible [77, 78]. However, the smaller number of voxels in this second step enabled a fast processing. The most suitable cluster (out of five) was again selected using the quality factor Q and comparing the IDAIF curve characteristics with those of normal GM.

3.3.4 Automatic IDAIF Selection Using Singular Value Decomposition

The masked $\Delta R2^*$ time courses were converted from a 4D dataset to 3D datasets, with x voxels in each slice and t time points. Using singular value decomposition [82] the time courses were divided in two orthonormal bases (U, V^T) and a diagonal matrix (D) according to:

$$\Delta R2^*(x,t) = UDV^T \tag{3.19}$$

The SVD is often used to distinguish signal from noise and further allows to separate individual components of an array of curves [83]. In dynamic contrast-enhanced MRI (section 3.4) those properties were used to robustly extract arterial voxels in the prostate [84]. Further, related methods like the factor analysis and independent component analyses demonstrated a good discrimination of arterial and venous voxels [85] with the possibility to identify local IDAIFs [71, 86]. In this study, the SVD was utilized to find a global IDAIF. To this end, the decomposition (Eq. (3.19)) was done for each of the previously selected five slices separately. While V^T characterizes a set of basic time courses or components, U represents their contribution to the voxel values of the image. The diagonal matrix D contains singular values in a descending order and was used to eliminate noise with a cut-off value of 0.05. In general, this reduced the data to the first three components. Accordingly, only these three basic time courses (Figure 3.4) contained signal information and were used to select the IDAIF.

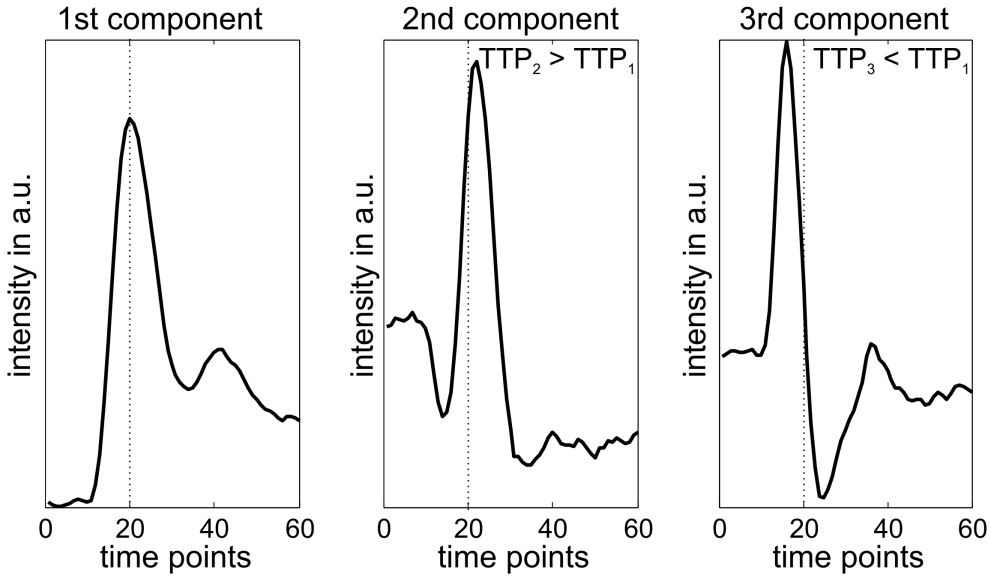

Figure 3.4: Typical example from a patient dataset showing the first three components of V (v_1, v_2, v_3) after SVD of a single voxel $\Delta R2^*$ time course. The dotted line displays the time-to-peak (TTP) in the first component. While the TTP of the second component is later than that of the first, TTP of the third component is earlier.

Each of the k basic time courses $v_k(t)$ had a particular shape (Figure 3.4). The recombination of these curves (Eq. (3.20)) either favors or penalizes the arterial characteristic of the $\Delta R2^*_{SVD}$ curves depending on the sign of the $u_{x\,k}$ values (Figure 3.5):

$$\Delta R2^*_{SVD}(x,t) \approx \sum_{k=1}^{3} u_{x\,k}\, d_k\, v_k(t) \qquad \textbf{(3.20)}$$

The minima and maxima of the basic time courses as well as the ratios between their extrema were used to characterize their shape. If the maximum of the second or third components curve was earlier than the peak in the first curve, voxels with corresponding positive $u_{x\,2/3}$ were selected. Analogous to this, if the TTP of component two or three was later than the TTP of component one, voxel with negative $u_{x\,2/3}$ were picked. For the first component, only the largest 25 % of the amplitudes $u_{x\,k}$ were included. Within this mask, amplitudes of the components two and three were selected if they were part of the largest (if positive) or smallest (if negative) 5 %. Within this mask, noise suppressed $\Delta R2^*_{SVD}$ curves were calculated, multiplying UDV^T using the truncated D. Next, the time courses were averaged to get a potential IDAIF for each of the five slices. Maximization of the quality parameter Q (Eq. (3.18)) and comparison of the shape characteristics with those of healthy GM were used, as described above to select the best arterial-like curve.

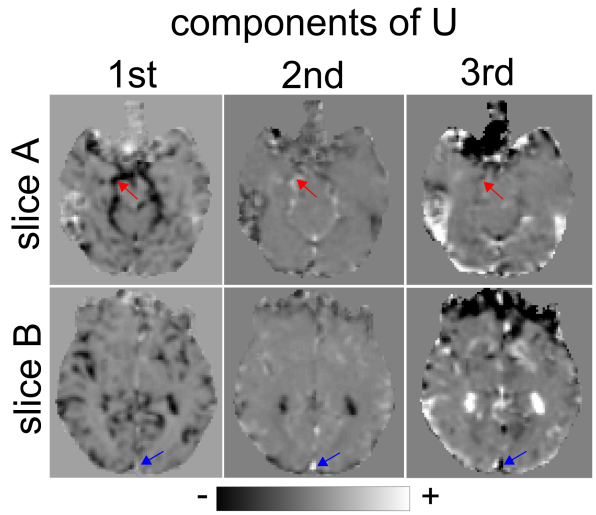

Figure 3.5: Typical example from a patient dataset showing the first three components of U after SVD of two slices. The red arrow displays a possible artery, while the blue arrow points to a vein. The gray level indicates the range of values in arbitrary units.

3.3.5 Arrival Time Corrections of IDAIF

CBV quantification methods that use deconvolution are prone to timing errors of the IDAIF [87]. In comparison to the real arterial input, IDAIF dispersions and delays can occur due to transit time differences between large and small vessels, acquisition timings or an improper selection of the IDAIF. To minimize the variance, an arrival time correction was established in this work. Related approaches were mainly used to optimize CBF and did not investigate the impact on CBV [88-90]. To analyze the impact of ATC on CBV results, the globally selected IDAIF was individually shifted for each voxel before deconvolution, until it was aligned with the voxels tissue curve. To align the curves, either the TTP (ATC_{TTP}) or the BAT (ATC_{BAT}) could be used. Both possibilities were investigated in this work.

3.4 Quantification of Cerebral Blood Volume with DCE-MRI

Alternative methods, exploiting contrast agent-induced changes of the longitudinal relaxation times (T1) for perfusion imaging, are termed dynamic contrast-enhanced (DCE) MRI. DCE data were acquired in one accessible patient study during application of the pre-bolus. These data were evaluated for plasma volume v_p (Eq. (3.22)) that served as an independent measure of CBV for comparisons with corrected and uncorrected DSC-derived CBV values.

DCE techniques show a rather small signal change in areas with intact BBB because T1 decreases only in the direct proximity of the CA, and the implementation of fast T1-weighted techniques with sufficient volume coverage is more challenging. However, this technique is known to be quantitative [91]. The original intention of this method was the characterization of the vascular permeability. To this end, a one-compartment model that includes CA transitions between blood plasma and EES was introduced by Tofts and Kermode [92]:

$$C_{tis}(t) = v_p C_p(t) + K^{trans} e^{\left(-\frac{K^{trans}}{v_e} t\right)} \int_0^t C_p(\tau)\, e^{\left(-\frac{K^{trans}}{v_e} \tau\right)} d\tau \qquad \textbf{(3.21)}$$

Here, C_p is the concentration of CA in blood plasma and v_e the volume of the EES.
In brain tissue with intact BBB the permeability of vessels, represented by the transfer constant (K^{trans}), is low and back-diffusion can be neglected ($K^{trans}/v_e \rightarrow 0$). This allows the use of a simplified model version: the Patlak method or Patlak plot [93]. Here the problem is linearized, dividing Eq. (3.21) by $C_p(t)$ and including the above assumptions, technically converting the bolus experiment into a constant infusion [34]:

$$\frac{C_{tis}(t)}{C_p(t)} = v_p + K^{trans} \frac{\int_0^t C_p(\tau)\, d\tau}{C_p(t)} \qquad \textbf{(3.22)}$$

3.5 Quantification of an Apparent Oxygen Extraction Fraction

Since the primary motivation for this work was to improve the accuracy of the CBV values for the measurement of tissue oxygenation in patients with brain tumors, the apparent or relative oxygen extraction fraction (rOEF) was quantified as described in [10, 60, 61] using CBV values obtained from different correction approaches.
The rOEF approach is based on separate measurements of T2 and T2* [60, 94], from which the reversible transverse relaxation rate $R2' = 1/T2^* - 1/T2$ can be received. When CBV is additionally measured as a first approximation for the venous fraction of CBV [95], rOEF can be calculated according to:

$$rOEF = \frac{R2'}{\left(\frac{4}{3}\pi\, \gamma\, \Delta\chi_0\, Hct_{small}\, B_0\, CBV\right)} \qquad \textbf{(3.23)}$$

In this study, the field strength B_0 was 3.0 T. All other parameters could be attained from literature and were identical to those used in [10, 60, 61]. The susceptibility difference $\Delta\chi_0$ between fully oxygenated and fully deoxygenated blood was $0.264 \cdot 10^{-6}$

[96], the small-vessel hematocrit (Hct_{small}) 0.36 [97] and the gyromagnetic ratio γ was $2.675 \cdot 10^8$ $s^{-1}T^{-1}$.

3.6 DSC Simulation Study

As a primary assessment of post-processing methods for extravasation corrected DSC-MRI, a simulation study was done. In a first step, an optimized determination of the extravasation phase and the arrival time correction (TTP or BAT) was done for SVD-based methods. The optimized parameters were used for subsequent simulations and analyses of patient data. Several factors known to influence CBV quantitation [58, 67] were separately investigated with regard to the different leakage correction methods. It is to be expected that individual leakage correction approaches benefit more or less from the underlying assumptions of the simulation. Focus was therefore a relative rather than absolute comparison between methods and their individual dependencies on input parameters. Further, it was simulated whether the results in patient data, which were obtained with different imaging protocols known to influence CBV [51, 62], are comparable.

3.6.1 Simulation of Signal-Time Curves

All simulation studies needed synthetic signal-time courses, which mimic the real behavior as closely as possible. Therefore, the simulations included information about sequence type and parameters, properties of tissue and contrast agent as well as physiological behavior. Their interplay governs the signal evolution.

For the assessment of the different leakage correction methods, sequence parameters for simulated time courses were identical to those used in most of the patient examinations (TR = 1500 ms, TE = 30 ms, α = 90°). The resulting signal-time course S was calculated with the equation for a spoiled gradient echo sequence [25]:

$$S(t) = S_0 \frac{\left(1 - e^{-TR\,R1(t)}\right) e^{-TE\,R2^*(t)} \sin\alpha}{1 - e^{-TR\,R1(t)} \cos\alpha} \qquad \textbf{(3.24)}$$

The baseline signal S_0 depends on the proton density and scanner hardware and was chosen so that a suitable signal drop could be observed. The acquisition time t was 120 s, corresponding to 80 dynamic images. This is in line with the available patient data and recommendations from literature [55].

The initial pre-contrast relaxation times of tissue were defined according to values measured in glioma patients [10]. Pre-contrast T1 (T10) was also set to shorter values to simulate a small pre-dose of contrast agent. Used relaxation times were $T2^*$ = 50 ms and T10 = 1200 ms or T10 = 500 ms. Values for T10 allowed to simulate conditions with

predominant T1 (T10 = 1200 ms) and T2/T2* (T10 = 500 ms) leakage effects (section 2.5).

Incorporated tissue compounds comprised blood plasma, EES and intracellular space (ICS). The corresponding volumes (v) and other specific values are summarized in Table 3.1. The pure CA concentration time course of the arterial input function ($C_{aif}(t)$) was modeled similar to that in [62], using the parameters A = 5, B = 0.01 and a time to peak concentration t_p of 2 s:

$$C_{aif}(t) = \begin{cases} 0, & t \leq t_0 \\ A\left(\frac{t}{t_p^2}\right) e^{-t/t_p} + B\left(1 - e^{-t/t_p}\right), & t > t_0 \end{cases} \quad \textbf{(3.25)}$$

By convolution of $C_{aif}(t)$ with an exponential residue function the CA amount in blood plasma ($v_p C_p(t)$) was determined. The EES concentration $C_e(t)$ was calculated with the Kety-Tofts model [98] as described in Quarles et al. [Eq. 16 in 62]. The extraction rate (E) of CA from blood plasma to EES was specified by the permeability-surface area product (PS) of the vessel wall and the CBF. Using the plug-flow model, the dependence of the transfer constant K^{trans} on physiological parameters can be stated as follows [98]:

$$K^{trans} = E\ CBF\ \rho\ (1 - k_H) \quad \textbf{(3.26)}$$

A transition of CA into ICS was not permitted, i.e. $C_i(t) = 0$, because Gd-DTPA is not internalized in cells. The changes in tissue and arterial relaxation rates $R1(t)$ and $R2^*(t)$ were calculated from the respective CTCs using Eqs. (3.27) and (3.28) [62]:

$$R1(t) = r_1 \left(v_p C_p(t) + v_e C_e(t)\right) + R10 \quad \textbf{(3.27)}$$

$$\begin{aligned} R2^*(t) &= r_2 \left(v_p C_p(t) + v_e C_e(t)\right) \\ &+ K_p v_p \left(v_e \left|C_p(t) - C_e(t)\right| + v_i C_p(t)\right) + K_e v_e v_i C_e(t) \\ &+ R20^* \end{aligned} \quad \textbf{(3.28)}$$

This conversion assumes a fast water exchange between the compartments and includes microscopic and mesoscopic susceptibility effects following CA injection. An overview of the individual variables is given in Table 3.1.

Table 3.1: Overview of tissue and contrast agent specific input parameters for signal simulations. * [99]; # [48]

Parameter	Description	Value
v_p	distribution volume of blood plasma	0.02 ... 0.08
v_e	distribution volume of EES	0.25
v_i	distribution volume of ICS	$v_i = 1 - (v_p + v_e)$
PS	product of permeability and surface area of the vessel wall in ml/100 g	0 ... 50
K_p, K_e	susceptibility calibration factors for blood plasma and EES, chosen to get a suitable signal drop, in $mM^{-1}\ s^{-1}$	$K_e = 0.50\ K_p$
r_1, r_2	T1 and T2 relaxivity of Gd-DTPA in $mM^{-1}\ s^{-1}$	r_1 = 3.3 *, r_2 = 5.3 #

The signal-time courses were simulated for different representative tissue types. To achieve this, the input values for CBV (CBV_{in}) and CBF (CBF_{in}) were chosen appropriately. For white matter, input values were CBV_{in} of 2 ml/100 g and CBF_{in} of 20 ml/100 g/min. For gray matter, CBV_{in} was set to 4 ml/100 g and CBF_{in} to 60 ml/100 g/min. For tumor tissue, a range of CBV_{in} (2 to 8 ml/100 g) and CBF_{in} (20 to 120 ml/100 g/min) values were chosen, which generated different MTTs in the range of 2 s to 12 s according to the central volume principle (Eq. (2.6)). The different CBFs also directly changed the degree of extravasation (Eq. (3.26)). All hemodynamic input parameters together with T10s determine the signal behavior in the presence of leakage effects (Eq. (3.24)). Those influences on CBV could thus not completely be separated.
Time curves for all simulated situations were replicated 1024 times and added with random noise. As SNR in patients, after smoothing the data was commonly about 80 (76 ± 20), this value was used for the following simulations unless indicated otherwise.
In order to compare different sequence parameters, as used in patient data (section 3.7.1), two additional signal-time courses with alternative sequence parameters were simulated. This contains a GE-EPI experiment with a flip angle of 70° and a PRESTO (principles of echo-shifting with a train of observation) sequence with TR = 17 ms, TE = 25 ms and α = 7° (section 3.7.1). The signal evolution for the latter was calculated according to the equation for spoiled gradient echo experiments with echo-shifting [Eq. 16.36 in 100].

The generated signal-time curves were processed as described in chapters 3.1.2 and 3.2.2, respectively calculating uncorrected and corrected CBVs. Since different leakage correction methods show a distinct sensitivity to different influences, some dependencies were only tested for a part of the methods.

3.6.2 Optimizing Input Parameters of SVD-based Methods

Validation of arrival time corrections: Methods that use SVD for CBV quantification are sensitive to timing alterations of the IDAIF [66, 87, 89]. To reduce effects due to dispersions and delays of the IDAIF, an arrival time correction (ATC) was established as described in section 3.3.5. Both alternative versions (alignment to TTP (ATC_{TTP}) and BAT (ATC_{BAT})) were tested and compared. To validate the effectiveness and accuracy of ATC, simulated signal-time courses (section 3.6.1) with a CBV of 4 ml/100 g, a CBF of 60 ml/100 g/min and without leakage were converted into concentration time courses (section 3.6.1, Eqs. (2.15), (3.1)). The IDAIF was modified by introducing delays (-3.0 s to +3.0 s) and dispersions (FWHM: 0.8 to 2.3 times broader than the real AIF) while keeping the area under the curve constant. Deconvolution of the resulting IDAIFs and tissue time curves was done for all timings with sSVD and TiSVD, either without ATC or after the IDAIF had been shifted with the respective ATC method. CBV values were calculated according to Eq. (3.5).

Optimal definition of the extravasation phase: Leakage correction with method III needs the discrimination between a perfusion and an extravasation phase during the course of the impulse response. In this simulation, the influence of the defined threshold between both phases on $CBV_{method\ III}$ was investigated. In its original implementation, the beginning of the extravasation phase was set to T_c [13]. The averaging of $H(t)$ for the estimation of K_2 was consequently started at T_c. However, previous own work demonstrated that method III showed rather small K_2 values for T1 effects and predominantly underestimated CBVs, irrespective of leakage effect [63]. When using T_c, the start of the averaging interval is usually located at the initial downslope of the residue function, which means that the average is probably systematically too high (stronger T2* effects, weak T1 effects). Hence, in the actual work the beginning of this averaging interval was varied between T_c and 10 times T_c, to investigate its impact on $CBV_{method\ III}$ and to optimize results with the goal to reproduce the input parameters as accurately as possible. All other parameters were kept constant.

3.6.3 Dependencies of Extravasation Correction Methods

SNR: In perfusion imaging, the stability of methods plays an important role in clinical interpretation. Therefore, the noise sensitivity of the different leakage correction methods was analyzed by comparing the resulting CBV values with the respective input values at

different noise levels. In patient data at 3.0 T, typical SNRs of 80 are observed (previous section). Most studies in literature analyzed data from 1.5 T scanners and found SNRs of 40 [67]. Based on this information, in addition to the noiseless reference, SNRs of 40, 60, 80 and 125 were simulated, and results were compared among all correction methods.

Strength of extravasation: Next, the dependence of the correction algorithms on the strength of extravasation, determined by the transfer constant K^{trans}, was investigated. According to Eq. (3.26), K^{trans} directly interacts with CBF and thus, via the central volume principle, also the MTT needed to be changed in order to keep the CBV constant for different values of K^{trans} (Table 3.2). The effectiveness of the correction methods for different K^{trans} values was tested for both leakage effects. The leakage correction was done with ideal IDAIFs and reference curves to minimize interaction with other effects.

Table 3.2: Range of evaluated transfer constants (K^{trans}) and corresponding cerebral blood flow (CBF) and mean transit time (MTT) values to keep a constant cerebral blood volume (CBV) of 4 ml/100 g.

K^{trans} in min^{-1}	CBF in ml/100 g/min	MTT in s
0.06	20	12
0.11	40	6
0.18	60	4
0.33	120	2

There is a known evidence in the literature that SVD-based methods themselves and the leakage correction method of Boxerman et al. [12] are sensitive to MTT differences between the IDAIF or reference curve and the individual tissue time courses [63, 101]. From [68, 87] it could be suspected that the standard truncated SVD approach should be more sensitive than the TiSVD approach. To investigate these assumptions, temporal alterations of reference curves and IDAIFs were analyzed separately for AUC- and SVD-based approaches.

Reference curve: Three of the correction methods are based on reference curves. While method IV generates an individual reference for each voxel, method II temporally scales the global reference curve for each voxel, and method I uses only one single reference curve. Therefore, the latter two methods are indirectly affected by MTT alterations. Because the quality of fitting (Eq. (3.7)) and thus of the leakage estimation depends on this initial curve, its impact on CBV was studied. To this end, four different reference curves were investigated. Typically, the reference curve is selected from healthy tissue without obvious leakage [12, 21, 102]. Thus, three reference curves were represented by simulated white matter, gray matter (section 3.6.1) and the average of both, similar to the one used for analysis of patient data. The leaky (K^{trans} = 0.18 min^{-1}) tumorous tissue

was simulated with CBV_{in} = 8 ml/100 g and CBF_{in} = 60 ml/100 g/min, typical for the characteristically higher CBV in high-grade gliomas [55]. The ideal reference curve was simulated as tumorous tissue without leakage because it had otherwise the same hemodynamic properties.

IDAIF delays and dispersions: Methods I and II depend only on the area of the IDAIF and thus delays and dispersion do not alter CBV results. Consequently, the impact of IDAIF delays and dispersions on leakage affected data was only tested for SVD-based methods. Delays (-3.0 s to +3.0 s) and dispersions (FWHM: 0.8 to 2.3 times broader than the real AIF) were identical to those used in section 3.6.2. Affected leakage correction approaches were in this case methods III and IV, while only method III was tested with different SVD approaches (sSVD, TiSVD), with and without ATC.

3.7 Evaluation of Methods in Patient Data

3.7.1 Patient Collective and Data Acquisition

All data acquisitions were performed on human 3.0 T scanners. Data from two patient studies were included in the CBV analysis.

(1) On a 3.0 T Siemens mMR Biograph (Siemens Medical Solutions, Knoxville, TN) patients with glioma underwent a simultaneous MRI and PET protocol with the aim to investigate tumor hypoxia and dynamic uptake of a tumor-specific amino acid tracer [^{18}F] O-(2-fluoroethyl)-L-tyrosine (FET). MR acquisitions were performed using a 16-channel head and neck coil.

(2) On a 3.0 T Philips Achieva system (Philips Healthcare, Hamburg, Germany), two DSC perfusion acquisitions with two different contrast agents were performed on different days in patients with brain lesions. This double perfusion study used an eight-channel phased-array head coil (receive-only) and a whole-body transmit coil.

In all studies, anatomical images were acquired according to the standard clinical protocol. This included T2-weighted FLAIR and T1-weighted (MP-RAGE) post-contrast images.

Hypoxia study: Twenty-six patients (62 ± 15 years, 17 male) with histologically confirmed primary high grade glioma (WHO°IV), five patients (46 ± 5 years, 3 male) with WHO°III and five (44 ± 20 years, 4 male) with low-grade glioma (WHO°II) were examined preoperatively.

DSC perfusion imaging was done using a 2D dynamic single-shot gradient-echo EPI sequence (TR = 1500 ms, TE = 30 ms, FA = 70°/90°, 60/80 dynamics, voxel size: 1.80 × 1.80 × 4 mm³). In total 20 slices were acquired in an interleaved ordering scheme. A bolus of 15 ml Gd-DTPA (Magnevist, Bayer Vital, 0.5 mmol/ml) was injected 3 to 5 minutes after a pre-bolus of 7.5 ml, both with 4 ml/s injection rate. In eight of the patients, the first CA dose was used for a second DSC acquisition. For the other 28

patients, this pre-dose was used to acquire a DCE time series with a saturation recovery Turbo-FLASH sequence (TE = 1.2 ms, TR = 149 ms, FA = 30°, saturation delay = 100 ms, voxel size: 3.1 × 3.1 × 8 mm³, matrix: 64 × 64, GRAPPA[1] factor 2, phase partial Fourier of 6/8, 90 dynamics, temporal resolution: 2.2 s). A T1 map was acquired with the same Turbo-FLASH sequence using eight saturation delays between 100 ms and 3000 ms. The protocol contained quantitative T2 and T2* mapping for determination of tissue oxygenation (see previous work for details: [10, 60, 61]).

Parallel to MRI dynamic [^{18}F]FET-PET data were acquired over 40 min. Three static images and 37 dynamic time frames were reconstructed (3D ordered subset expectation maximization, matrix: 192 × 192, voxel size: 1.16 mm).

Double perfusion study: Eleven patients (57 ± 20 years, 8 male) with contrast-enhancing tumors were examined in a double perfusion study. Eight patients had a histologically confirmed primary high-grade glioma (WHO°IV), one patient had a ganglioglioma, one an anaplastic glioma °III and one a metastasis. For perfusion imaging a T2* weighted 3D PRESTO sequence (TR = 17 ms, TE = 25 ms, FA = 7°, 40 dynamics, temporal resolution: 1.94 s, voxel size: 1.80 × 1.80 × 4 mm³, 30 slices) was used. This acquisition was repeated on two consecutive days, once with gadofosveset trisodium (0.12 ml/kg body weight, 0.25 mmol/ml), once with Gd-DTPA (Magnevist, Bayer Vital, 0.20 ml/kg body weight, 0.50 mmol/ml). The injection rate was 4 ml/s in each case.

Table 3.3 lists characteristics of all contrast agents used during this work.

Table 3.3: Description of used contrast agents for MRI (Magnevist and VASOVIST) and PET ([^{18}F]FET).[*] [103]; [#] [104, 105]

Label	Distribution and Binding
Magnevist® (Gd-DTPA, gadopentetat dimeglumin)	acyclic, ionic; intravascular in brain if BBB is intact, elimination half-live: 1.6 ± 0.13 hours [*]
VASOVIST® (gadofosveset trisodium)	binds reversibly to endogenous serum albumin; intravascular in brain if BBB is intact, elimination half-life: 16.3 ± 2.6 hours [*]
[^{18}F]FET (O-(2-fluoroethyl)-L-tyrosine)	artificial amino acid, specific uptake by several tumor cells via upregulation of L-type amino acid transporters [#]

[1] GeneRalized Autocalibrating Partial Parallel Acquisition

3.7.2 Image Processing and Volumes of Interest

Image processing was done in MATLAB R2013a (MathWorks, Natick, US) with SPM12 (http://www.fil.ion.ucl.ac.uk/spm/) and customized programs.

Segmentation of masks: The T1-weighted post-contrast images and the FLAIR images were both segmented with SPM12 to obtain probability maps of white matter (WM), gray matter (GM) and cerebrospinal fluid (CSF). Both data sets were segmented because pathological tissue in different ways confounds the estimation of tissue types for FLAIR and T1-weighted images. Via thresholding (probability > 0.75), six binary masks (2 × WM, 2 × GM, 2 × CSF) were generated. The combination (logical disjunction) of all six masks was used to create a meaningful whole brain mask. Potentially pathological areas, including areas with contrast enhancement in T1-weighted images (regions with disrupted BBB and large vessels) and FLAIR hyperintensity (solid tumor, edema), were identified by histogram-based thresholding [10]. To this end, the intensity values of the T1-weighted post-contrast images belonging to the binary WM mask and all values of the FLAIR images belonging to the GM mask were fitted with a normal distribution. The thresholds were set to μ_{WM} + 2.576 σ for the T1-weighted and μ_{GM} + 1.288 σ for the FLAIR image intensities. A combined mask (logical disjunction) was used to define the pathological tissue region.

Volumes of interest: Volumes of interests (VOI) in gray and white matter, VOI_{GM} and VOI_{WM}, were generated from the binary masks of GM and WM segments of the T1-weighted post-contrast images by subtracting the diseased tissue regions. Tumor VOIs were manually contoured with VINCI (Max-Planck-Institut für Neurologische Forschung, Cologne, Germany) based on threshold-segmented volumes by an experienced researcher. These included areas of edema (VOI_{EDE}), solid tumor (VOI_{T2T}) and contrast enhancing tissue (VOI_{CET}). VOI_{EDE} and VOI_{T2T} were contoured on FLAIR images, while VOI_{CET} was delineated on T1-weighted post-contrast images. An overlap between VOIs was not permitted. In patients with [^{18}F]FET accumulation in tumors, additionally the active tumor was identified in the 30-40 min sum image. A contralateral circular normal tissue region (radius = 1.5 cm) was drawn to calculate a tumor-to-brain ratio (TBR). For the VOI_{TUMOR} an isocontour of 1.6 TBR was used.

Image registration and timing: All images and masks (including VOIs) were registered to the first image of the DSC time course using the 'Coregister: Estimate & Reslice' option and standard parameters of SPM12. If two DSC acquisitions were made, either the second bolus (hypoxia study) or the Gd-DTPA (double perfusion study) DSC scans were used as the reference dataset on which all images were registered.

For the eight patients of the hypoxia study with two consecutive DSC acquisitions, an additional analysis was done, investigating the effect of prior slice time correction (STC) using SPM12. Classically, this method is used in functional MRI studies with 2D multi-slice data acquisition to compensate problems of timing assignment due to the slice

acquisition scheme [106, 107]. In DSC data it was rather seldom used [53], even though it has a potential impact on perfusion results. In this work, 2D EPI data with interleaved slice ordering were acquired, leading to a maximum time difference of 1.425 s between slices of the same acquisition. After STC, the complete 3D volume of one acquisition (temporal position) corresponded to the same time.
Each slice of the DSC time courses was smoothed with a Gaussian convolution kernel (3 × 3 × 3 voxels).

3.7.3 Determining Robustness and Quality of IDAIFs

This study tested the quality and reproducibility of one manual (section 3.3.1) and two automatic (sections 3.3.3 and 3.3.4) IDAIF selection methods using the known characteristics of a perfect AIF: early BAT, early TTP and a large and narrow peak. The manual selection was done exemplary for two patients. The intention of this study was to define an automatic, reproducible and global IDAIF.
The stability of the algorithms was investigated by repeating the manual selection with four observers and the automatic selection 100 times (N). Afterwards, the curves were compared using a robustness factor f_{robust} [108]:

$$f_{robust} = \frac{1}{MN}\sum_{i=1}^{M}\sum_{j=1}^{N}\left[AIF_{i,j} - \frac{1}{N}\sum_{j=1}^{N} AIF_{i,j}\right]^2 \quad (3.29)$$

Here, M is the number of time points and AIF denotes the selected arterial $\Delta R2^*$ curve. A high robustness correlates with a small f_{robust}, for identical curves $f_{robust} = 0$. The deviation between curves increases with increasing f_{robust}.

3.7.4 Calculation of Parameter Maps

CBV values were generated by modeling DSC-MRI, DCE-MRI and dynamic [^{18}F]FET-PET data. If these algorithms produced unphysiological negative CBV values, they were set to zero.
CBV_{DSC}: Absolute CBV_{DSC} values were calculated according to the methods described in sections 3.1.2 and 3.2.2. For each DSC scan, five uncorrected CBV values were calculated, including one $CBV_{unc\,1}$ and four $CBV_{unc\,2}$. These latter four combination possibilities resulted from the two SVD methods (sSVD, TiSVD) and the introduction of the ATC. For patients, the ATC_{TTP} was used because simulations demonstrated better performance (section 4.1.1). Further, six leakage corrected CBVs per DSC scan were calculated, including all leakage correction methods (I to IV) and the modifications of method III with regard to SVD algorithm (sSVD, TiSVD) and ATC_{TTP} (with and without). For each of those methods an additional K_2 map was created. For $CBV_{unc\,1}$ and

correction methods I, II and IV, the full (CBV_{full}) and first pass (CBV_{fp}) integration was done for all patients. The same CBV values were generated for both contrast agents of the double perfusion study group, gadofosveset trisodium (CBV_{Vaso}) and Gd-DTPA ($CBV_{Gd\text{-}DTPA}$). For each of the eight patients of the hypoxia study, where two consecutive DSC scans were acquired, all CBV variants were generated for both boli (CBV_{1st}, CBV_{2nd}). Further, also all method III variants were calculated with both integration ranges (full and first pass) and the ATC was analyzed in combination with STC (section 3.7.2). For the corrected $CBV_{method\ I}$, the correlation between both scans was additionally tested under the assumption of a non-linear relationship (Eq. (2.15) with $q_2 = 2615.9 \cdot 10^{-6}$ (ms mM^2)$^{-1}$, $r_2 = 0.4929 \cdot 10^{-3}$ (ms mM)$^{-1}$) between IDAIF signal and concentration. For this purpose, the areas of the IDAIFs were recalculated using the quadratic relationship for conversions to concentration. Additionally, concentrations of the reference curve (mean over healthy WM and GM) and the corresponding IDAIF were recalculated using two different tissue relaxivities (r_2 = 0.0053 ms^{-1} mM^{-1} [48], r_2 = 0.0870 ms^{-1} mM^{-1} [49]) in combination with the quadratic relationship for the IDAIF. CBV is calculated from the ratio of the areas under the tissue curves and the IDAIFs (Eq. (3.4)).

Within each patient, each CBV value was additionally normalized to the same automatically segmented healthy white matter region (segmented with SPM12, probability > 0.90, subtracted by CSF mask and the diseased tissue region). By normalizing all CBVs (nCBV) the results were forced to the range of physiologically reasonable values, which made CBVs more comparable between subjects and methods.

CBV_{DCE}: For patients of the hypoxia study CBV_{DCE} was calculated as described in Hirsch et al. [10]. The relevant models were briefly explained in section 3.4. Primarily, the Patlak plot was applied to quantify CBV and K^{trans} within the whole brain. In areas with potential extravasation a recalculation with the extended Tofts model was done. The AIF was determined manually for each patient by selecting four voxels in visible arteries. As for DSC, the signal had first to be converted to concentrations. Again, a linear relation between $\Delta R1$ and concentration was assumed. To obtain the initial longitudinal relaxation rates $R1$, an additional T1 quantitation was done as described in [10]. In this way, absolute CBV_{DCE} values could be obtained. In addition, CBV_{DCE} was in each patient normalized ($nCBV_{DCE}$) to the same healthy WM region that was applied on CBV_{DSC} values. The resulting absolute and normalized maps were used to classify DSC results.

CBV_{PET}: For most patients of the hypoxia study, a dynamic [^{18}F]FET-PET was acquired parallel to MRI. Dynamic PET requires pharmacokinetic modeling to achieve quantitative physiological parameters (chapter 2.3.2). The exploited method [109] is based on a two-tissue compartment model. Whereby, the distribution volume of the specific binding defined the blood volume. After a hierarchical cluster analysis of the data, a voxel-wise fitting was done. The initial parameters and fitting boundaries of each

voxel were defined by the mean curve of the corresponding cluster. The CBV_{PET} maps were provided by the nuclear medicine department and served as a second independent measure for CBVs.

rOEF: The rOEF was exemplary calculated according to section 3.5 for two patients. To analyze the impact of alterations (PB and post-processing) in CBV on the quality of rOEF maps, $CBV_{unc\,1}$ and the corresponding corrected values of method I achieved from the first and second bolus acquisitions were used for rOEF calculation.

3.7.5 Data Analysis and Statistical Methods

All calculated maps (different CBVs, K_2's) were once analyzed voxel-based within each patient, directly comparing the results of different correction methods and the effects of correction. Secondly, with respect to VOIs, values were averaged across tumor and healthy tissue regions and analyzed for all patients. Furthermore, the median and standard deviations within the VOIs were considered. In order to characterize the curve shapes in particular for comparisons of different acquisitions, rPH and rPSR values were also evaluated.

Sequence design: The impact of sequence parameters and designs (FA 70° versus FA 90° and PRESTO versus 2D EPI) on correction methods was examined in relation to simulations.

Comparison of correction methods: The combination of different procedures and acquisition schemes (only pre-bolus, only post-processing, pre-bolus and post-processing) applied to data from the hypoxia study was used to evaluate the most reliable and stable correction method. The amount and direction of corrections were investigated and compared with each other, and differences and agreements of the methods were evaluated. Since for reliable results, an accurate fitting is one of the basic prerequisites, the fitting residuals and individual curves were inspected carefully. Further, the impact of integration intervals (full versus first pass integration) on these correction methods was examined (section 3.7.4). Though both intervals are equally used in the literature [55], in leakage affected data a direct comparison has not yet been performed. Thus, the effect on absolute and normalized CBV values in presence of CA leakage was investigated.

The eight patients, where two DSC scans were acquired in one session, were used to evaluate the correction methods. The first dose served as a pre-bolus to minimize T1 leakage effects in the second acquisition (section 3.2.1). In case of appropriate post-processing, the significance of this technique should be reduced. The hypothesis that adequate post-processing would homogenize CBV results between the first and the second bolus, should allow figuring out the most reliable and stable correction methods. Likewise, using the accordance of results from both boli as an indicator for processing quality, further investigations concerning the integration range, the relationship between MR signal and CA dose and timing corrections were done.

Impact of contrast agent: All correction methods were further investigated using DSC-MRI acquired with different contrast agents (Gd-DTPA, gadofosveset trisodium). The more intravascular contrast agent gadofosveset trisodium (Vasovist) is generally used for angiography. Its usefulness for perfusion and extravasation imaging has not been investigated so far. Vasovist does not reenter (reflux = 0) the vasculature once extravasated. In case of disrupted BBB, it should better fit model assumptions for CBV leakage correction methods. Further, its relaxivity is higher and thus, a lower contrast agent dose should be necessary. Analyzed were all different leakage correction methods, ATCs and integration ranges. Here, the accordance between CBV results obtained with both contrast agents was used as an indicator for the validity of CBV estimates. Furthermore, results were used to better assess the meaning of K_2 values.

Validation of CBV_{DSC} with DCE and PET: DCE-MRI and PET provided independent reference values for CBV (CBV_{DCE} and CBV_{PET}). Theoretically, both methods allow a more accurate conversion of the measured signal into CA concentration. With PET, it is possible to create images of absolute CA concentrations (section 2.2). DCE is based on T1 enhancement, and thus the linear relationship between concentrations and $\Delta R1$ is valid for a wider value range (section 2.5). Since the spatial resolution of both techniques is lower than in DSC, for voxel-wise comparisons CBV_{DSC} was smoothed with a Gaussian kernel (5 × 5 × 5 voxels). Since modeled CBV_{PET} values are only reliable within the area of [^{18}F]FET accumulation, these comparisons were focused on VOI_{TUMOR}.

Potential usefulness of permeability related values: An additional output of all DSC-based leakage correction methods is the parameter K_2, that was used to study the heterogeneity of tumors. This was done by calculating the percentage of the tumor volume (VOI_{CET}) showing predominant T1 effects ($K_2 > 0$). In detail, the distribution of both effects and their extent were studied. Additionally, the influence of the PB was investigated and two different contrast agents were compared against each other. The relation between K_2 and vessel permeability was investigated using the K^{trans} values. Since DCE-MRI is the method of choice for permeability imaging, K^{trans} was used as a reference, even though in these patients only DSC data acquired after a pre-bolus were available, which potentially confounds the analysis.

Impact of CBV variability on rOEF: In a numerical study, the impact of altered CBV values on rOEF estimation was evaluated using Eq. (3.23) inserting realistic CBV deviations found in this study (-100 % to +200 %). In healthy brain tissue, a typical deoxygenated CBV of 3 ml/100 g, which corresponds to a total CBV of approximately 4 ml/100 g [110], can be assumed and therefore was used as reference CBV. Considering further a homogeneous OEF of about 0.4 in healthy brain tissue [111], at 3.0 T $R2'$ has to be 3.8 s^{-1}. Using Eq. (3.23) the change of rOEF according to the CBV variations due to different analyses methods, as observed in patient data, could be estimated. Further,

the quality of rOEF maps, calculated with four different CBVs ($CBV_{unc\ 1}$ and $CBV_{method\ I}$, each with and without pre-bolus acquisition) was visually inspected for two exemplary patients.

Statistical tests: The Wilcoxon signed rank test was used for statistical test regarding the comparisons between parameter maps of the same patient as well as for comparisons within the same patient cohort. For comparisons between different patient groups (hypoxia group versus double bolus group), the Wilcoxon-Mann-Whitney test was used. The consistency of different methods was described by the reproducibility coefficient (RPC = 1.96 standard deviations). A small RPC corresponded to high reproducibility or accordance of methods. Boxplots were used for group comparisons. VOI- and voxel-wise correlations were done with Pearson (CBV) and Spearman (K_2) correlation, unless stated otherwise. The correlation coefficient r thereby served as quality parameter.

4 Results

Some preliminary results of an initial method comparison have already been published [63]. The following results are based on more extended simulations as well as evaluations of a larger and an additional patient group.

4.1 Simulations

Simulations were performed to investigate the influence of image quality, physiological variations and processing parameters on the performance of individual extravasation correction methods and the resulting CBVs. The focus was thereby primarily on the individual dependence of methods on different parameters and their relation to other methods. Prior to this, the preferred type of the arrival time correction (ATC) and the optimal definition of the extravasation phase for method III variants have been investigated with regard to more accurate CBV values. The basis for all CBV calculations were perfusion curves simulated without and with contrast agent extravasation (section 3.6).

4.1.1 Effectiveness of Arrival Time Corrections prior to SVD

Two versions of an arrival time correction (ATC) for method III and its variants were investigated for several IDAIF delays and dispersions of simulated data without extravasation (section 3.6.2). Before SVD, the IDAIF was shifted for each voxel to correct delays, once in reference to TTP (ATC_{TTP}) and once to BAT (ATC_{BAT}).

Without ATC, the $CBV_{unc\,2}$ values decreased with increasing simulated delays of the IDAIF. Deviations of the median $CBV_{unc\,2}$ (sSVD) ranged from +13 % for the earliest IDAIF (-3.0 s) to -24 % for the latest IDAIF (+3.0 s) compared to the CBV calculated without IDAIF delay (perfect AIF). For $CBV_{unc\,2}$ (TiSVD), the deviations ranged from +12 % (-3.0 s) to -29 % (+3.0 s). Using ATC_{BAT} as well as ATC_{TTP} the maximal deviations from the CBV, obtained with the ideal AIF, were reduced to 3 % for each regularization technique (sSVD, TiSVD).

Deviations due to IDAIF dispersions, ranging from 0.8 times smaller to 2.3 times broader curves, followed no clear trend. A broadening up to 1.3 times the original FWHM increased the $CBV_{unc\,2}$ by 2 % (sSVD) and 6 % (TiSVD). A broadening of 2.3 times the FWHM resulted in deviations of up to 12 % (sSVD) and 50 % (TiSVD). Neither of the ATC techniques could reliably improve these results. Partly they even induced a slight worsening.

Both ATC methods corrected delays similarly well and failed for dispersion effects. In presence of both, delay and dispersion, the latter restricted the efficacy of correction. Since in patient data TTP can be determined more reliable than BAT, further studies were done with ATC_{TTP}.

4.1.2 Optimal Definition of Extravasation Phase

For correction method III, the impulse response $H(t)$ of the concentration time course needs to be separated in two components: an initial perfusion phase and a late extravasation phase (section 3.2.2). In the original publication of the method [13], the capillary transit time T_c, estimated with a Lorentzian fit of the residue function, defined the time point from which $H(t)$ was started to be averaged for estimation of K_2.
Figure 4.1 shows the influence of the starting point for $H(t)$ averaging, which was varied between the commonly used threshold T_c [13] and ten times T_c (section 3.6.2), on $CBV_{method\ III}$ (sSVD). With decreasing averaging interval (later threshold), the calculated CBV better approximates the input CBV (CBV_{in}), but the variance increased. The best accordance between the calculated CBV and CBV_{in} was found for eight times T_c. A shift of the threshold to ten times T_c showed no further improvement. Because a decreasing interval also increased the variance of CBV, for patients and further simulations the threshold was chosen to ensure that the extravasation phase at least contained ten time points. If possible, a threshold of eight times T_c was used; otherwise, it was reduced accordingly (section 3.2.2).
Using TiSVD, the estimated T_c was approximately two times longer than using sSVD. Thus, an increasing threshold had a minor effect on results.

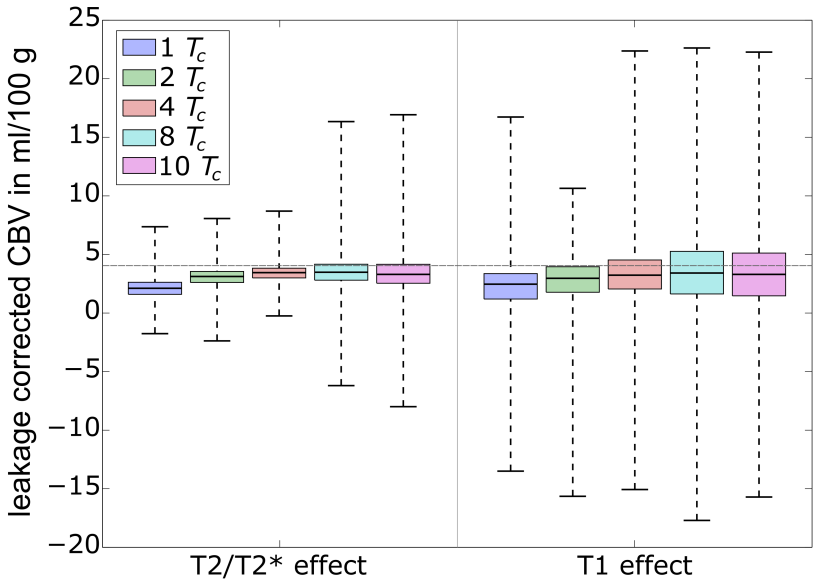

Figure 4.1: Influence of the definition of the extravasation phase, i.e. *H*(*t*) averaging interval: corrected CBV (method III – sSVD) for predominant T1 and T2/T2* effects with changing starting time (1 T_c to 10 T_c) for the averaging interval over *H*(*t*). Estimation from simulated data, with SNR = 80 and CBF = 60 ml/100 g/min. Gray line indicates reference CBV_{in} (4 ml/100 g). T_c = capillary transit time. The boxes contain all values between the first and third quartile, the black line inside marks the median, and the whiskers reach from minimum to maximum.

4.1.3 Influence of Noise

The SNR in clinical DSC perfusion studies is variable. It depends on hardware and sequence factors, but can be considerably deteriorated by physiological noise (respiration and cardiac pulsation) and patient motion. The impact of image noise on leakage correction methods was tested by adding Gaussian noise to the simulated signal curves. As described in section 3.6.3, this resulted in SNRs between 40 and 125.

Figure 4.2 shows an increased variance of normalized CBV_{calc} values with decreasing SNR in the presence of T2/T2*-based leakage effects. Similar behavior is observed in the presence of T1-based effects (data not shown). For both extravasation effects and all correction methods, CBV_{calc} was mainly underestimated. One exception was correction method II, which overestimated CBV for T1 effects (data not shown). A general difference of simulations with T1-based leakage effects as compared to simulations with T2/T2* leakage effects was the less pronounced underestimation of CBV. For all SNR levels, results of method I demonstrated the smallest variances and those of method III (sSVD) the largest. The Tikhonov regularization (TiSVD) reduced the variance of method III compared to standard truncation, but caused more severe underestimation. Using simulated data without delays or dispersions, additional ATC_{TTP} generally increased the variance, especially for CBV_{sSVD}.

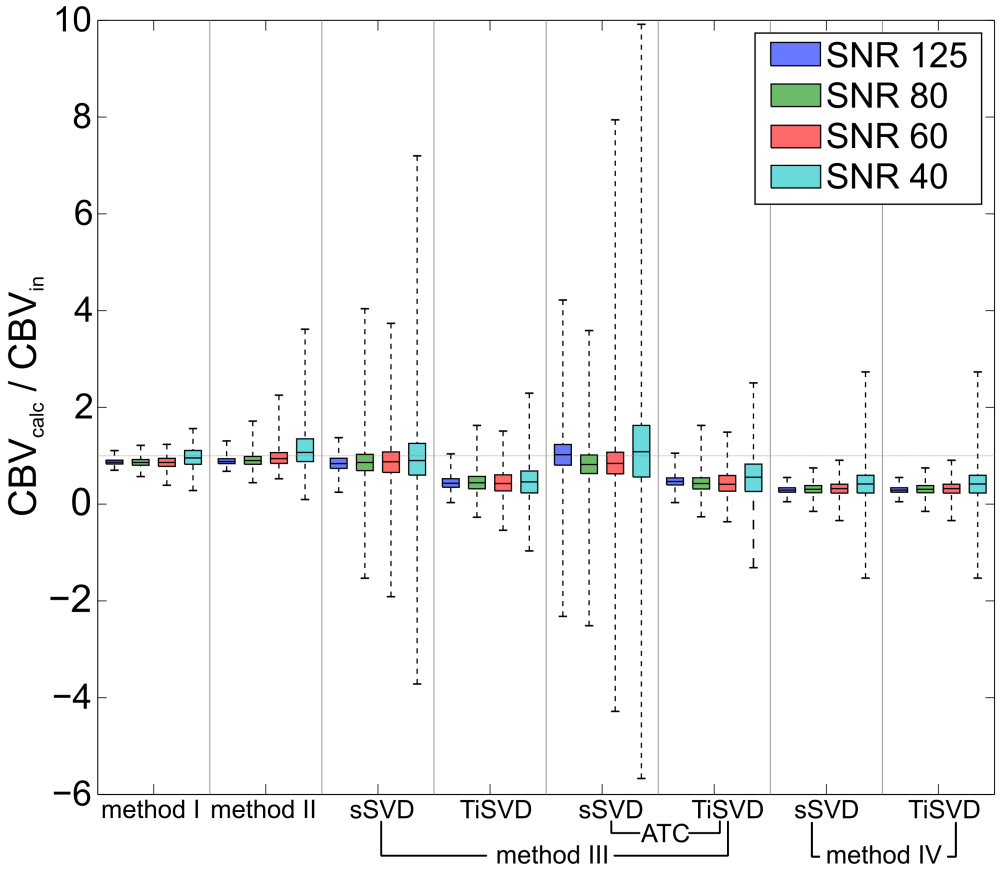

Figure 4.2: Influence of SNR on corrected CBV for T2/T2* effects. Calculated CBV (CBV_{calc}) normalized to input CBV (CBV_{in} = 4 ml/100 g) for all extravasation correction methods. CBF_{in} = 60 ml/100 g/min. The horizontal gray line equals 1.

4.1.4 Influence of the Strength of Extravasation

Simulations of different tissue types included a variation of CBF and MTT (section 3.6.3). One of the consequences is a concomitant change of the transfer constant K^{trans} because it interacts directly with the blood flow (Eq. (3.25)). Thus, K^{trans} values between 0.06 min^{-1} and 0.33 min^{-1} resulted from CBF values between 20 and 120 ml/100 g/min and MTT values between 2 and 12 s.

Nearly all methods showed at least some dependence on K^{trans}, which characterizes CA leakage, except for method II (Figure 4.3). The deviations from input CBV_{in} mostly decreased with increasing leakage, and again methods I and II showed the smallest absolute deviations. CBV variations with changing transfer constants were clearly different between the opposite leakage effects. For instance, deviations of methods I and III without ATC monotonically decreased with increasing leakage for T1, but not T2/T2* effects. For method IV, this effect was opposed. Further, the dependence seemed to get stronger after ATC, at least for sSVD, where the strongest dependence on K^{trans}

was found. A similar range between smallest and largest K^{trans} was observed only for method I in the presence of T1 effects. Less prone were methods III (TiSVD) and IV, which generally showed larger deviations.

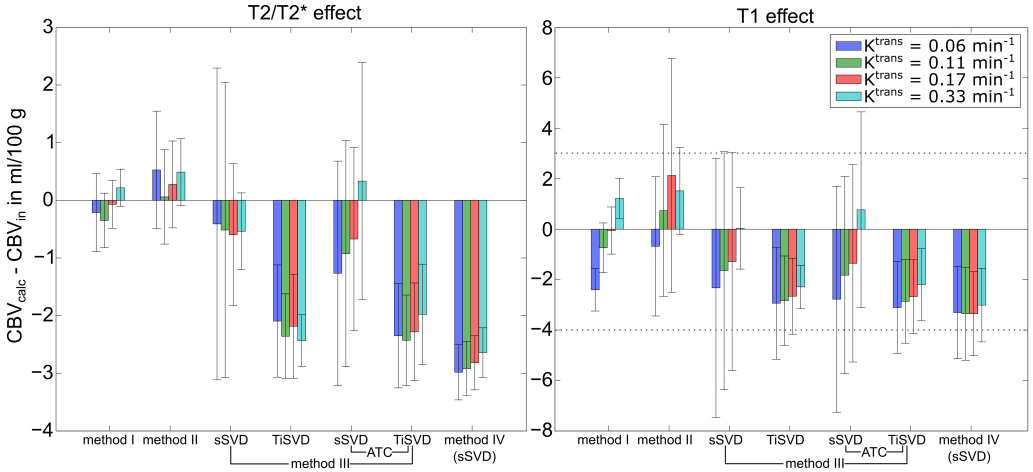

Figure 4.3: Influence of the transfer constant K^{trans}: difference between calculated CBV (CBV_{calc}) and input CBV (CBV_{in} = 4 ml/100 g) for T2/T2* (left) and T1 (right) effects, for a range of K^{trans} values between 0.06 and 0.33 min^{-1}. The dotted lines in the right graph indicate the range of values in the left graph. Results of method IV are only shown for sSVD because results were identical with TiSVD. Please note that the absolute difference rather than the ratio between CBV_{calc} and CBV_{in} is shown to better illustrate the effects in the presence of large variances between methods.

4.1.5 Reference Curve Dependence

For methods I and II, the tissue-derived reference curve is most important for extravasation correction. The reference curve serves as the basis for the curve-fitting procedure that determines K_2 (Eqs. (3.6), (3.8)) and is for those methods more relevant than the IDAIF (section 3.2.2).

Figure 4.4 shows CBV values calculated with methods I and II, in dependence on reference curves representing four different tissue types as defined in section 3.6.3. Even the perfect reference curve, corresponding to tumorous tissue without leakage, led to a deviation from input CBV_{in}, being generally overestimated. With decreasing MTT of the reference tissue, the ratio between calculated CBV_{calc} and input CBV_{in} increased for T2/T2* effects and decreased for T1 effects. Compared to method I, method II showed comparable deviations from CBV_{in}, but a higher variance over all reference tissues.

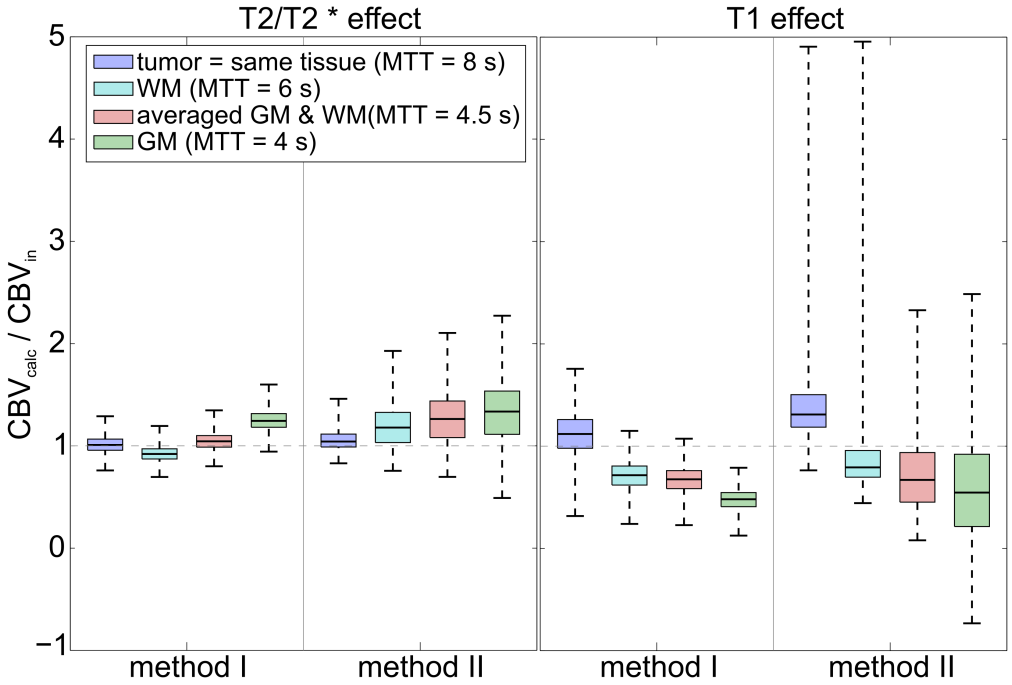

Figure 4.4: Dependence on reference curve for methods I and II, for both extravasation effects. CBV_{calc} values were normalized to the input CBV_{in} (8 ml/100g). CBVs of reference tissues were: CBV_{Tumor} = 8 ml/100 g (blue), CBV_{WM} = 2 ml/100 g (cyan), $CBV_{GM\&WM}$ = 3 ml/100 g (red), CBV_{GM} = 4 ml/100 g (green). CBF was 60 ml/100 g/min, leading to different mean transit times (MTT). GM = gray matter, WM = white matter. Note: the normalized CBVs for the actually perfect reference curve are generally larger (compared to other simulations) because of prolonged MTTs.

4.1.6 Effect of IDAIF Delays and Dispersions

The extravasation correction methods III and IV require an IDAIF for CBV quantitation in order to deconvolve the tissue curves and generate the residue functions (section 3.2.2). Therefore, the effect of delayed and dispersed IDAIFs on CBV values was investigated for standard and Tikhonov regularization (section 3.6.3). Finally, the effect of correcting the IDAIF shift (ATC_{TTP}) on leakage corrected $CBV_{method\ III}$ was determined.

Figure 4.5 shows the dependence of CBV_{calc} on IDAIF delays and dispersions for predominant T1 effects. Most notably, the TiSVD reduced the variance of CBV and its dependence on delay and dispersion compared to the sSVD. For both regularization techniques, the variance of $CBV_{method\ III}$ decreased with increasing delay (Figure 4.5-left). Additional arrival time correction (ATC_{TTP}) eliminated this dependence on delay for both regularization methods. CBV values calculated with method IV did hardly depend on delays, but showed an increased variance if the IDAIF was dispersed. A similar behavior was observed for T2/T2* leakage effects (data not shown).

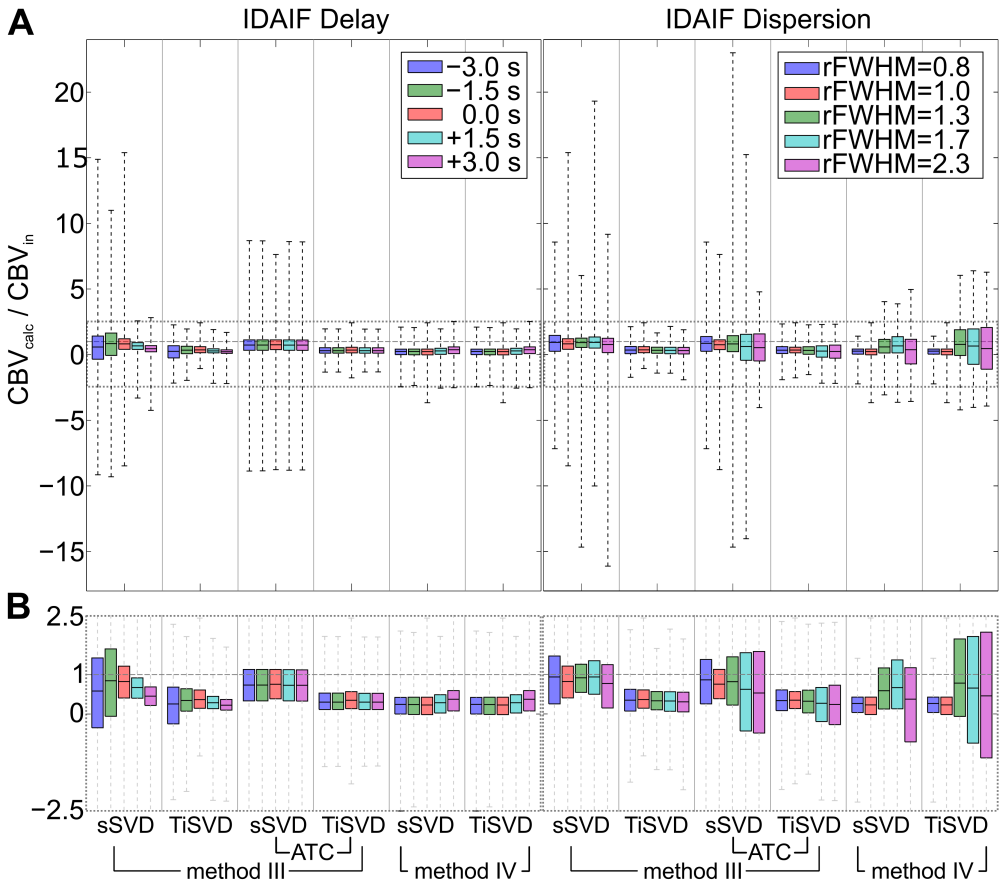

Figure 4.5: Effect of IDAIF delays and dispersions: ratio of calculated (CBV_{calc}) and input CBV (CBV_{in}) for simulated data with varying IDAIF delays (left) and dispersions (right) relative to the real AIF. Simulations for T1 extravasation effects, with SNR = 80 and CBF = 60 ml/100 g/min, dashed gray line = 1. (A) Full range ordinate, (B) zoomed area indicated by dotted gray boxes in (A). The colored boxes comprise all values between the first and third quartile, the black line inside marks the median and the whiskers reach from minimum to maximum.

4.2 Influence of Sequence Parameters

Three different sequence variants were used in patient studies analyzed in this work (section 3.7.1). While the hypoxia study used a 2D single shot EPI sequence, the double perfusion study used a 3D PRESTO sequence. The FAs, TRs and TEs were different for both sequences. Additionally, two FAs, 90° and 70°, were used within the hypoxia group. In simulations (section 3.6.1), the reduction of FA from 90° to 70° (at identical TR = 1500 ms) somewhat reduced the degree of T1 effects. Within the hypoxia study group, data from eight patients were acquired with a flip angle of 70°, while 28 data sets were acquired with a flip angle of 90°. Data acquired with PB demonstrated neither a difference in the extent (percentage of affected tumor area) nor the strength (absolute

values of K_2) of T1 leakage effects between both flip angles. Further, in none of the VOIs a significant difference of rPSR values ($p > 0.05$) was found.
In simulations, the 2D ssEPI (TR = 1500 ms, $\alpha = 70°$) and the 3D PRESTO (TR = 17 ms, $\alpha = 7°$) displayed no differences in signal characteristics. A comparison of patient data acquired without a PB (in different patient groups) yielded a larger extent of T2/T2* effects for the PRESTO acquisition (about 30 %, depending on the correction method), compared to ssEPI. With respect to the strength of the predominant leakage effect, both groups showed similar rPSR values. In contrast, data acquired with PRESTO (without PB) showed somewhat more extended T1 effects than ssEPI acquisitions with PB and 70° FA, except for correction method III (sSVD). In accordance to that, rPSR values for ssEPI with PB were smaller.

4.3 Robustness and Quality of IDAIF Selection Algorithms

The selection of an image-derived arterial input function (IDAIF) is vital for CBV quantification [73, 112], either for scaling or as deconvolution input. In patient data taken from the hypoxia study, three selection algorithms (section 3.3) were tested and rated with regard to their reproducibility and shape characteristics.
The automatic IDAIF selection algorithms clearly improved the quality and stability compared to manual IDAIF selections. Figure 4.6 shows two patient examples. The manual curves (blue) display a clear variance between the four observers and the two different selections of observer 1. Further, their peak heights were smaller than that of the SVD selected curves and similar to the peak height of the curves selected by the cluster algorithm. With a large robustness measure f_{robust} of about 10^{-4} ms^{-2} the manual selections were significantly less robust than automatic selection algorithms ($f_{robust} < 10^{-6}$ ms^{-2}).

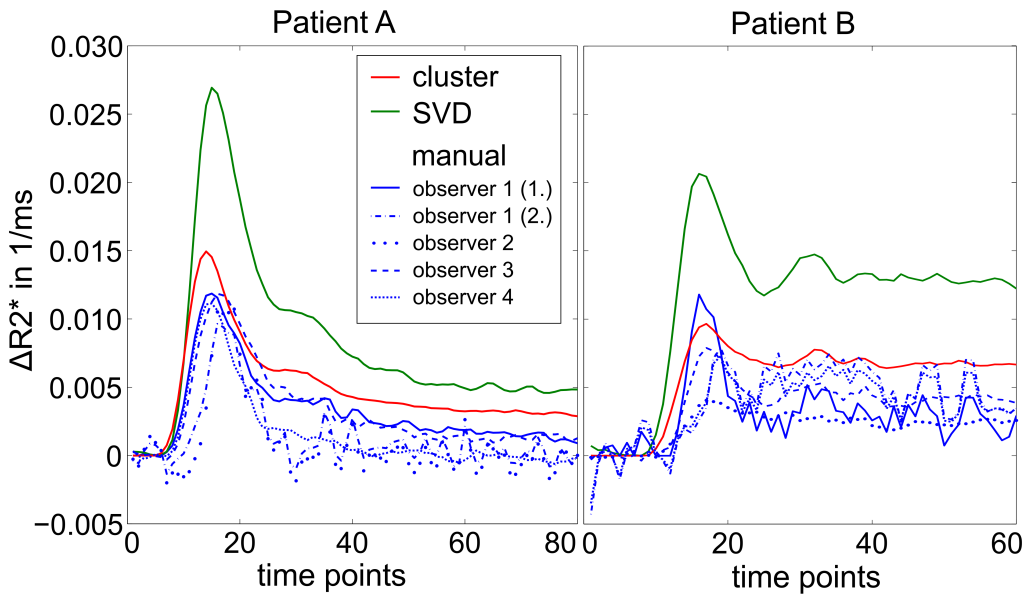

Figure 4.6: Quality of IDAIF selection algorithms illustrated in two patient examples. Manually selected curves from four different observers (blue). Observer 1 selected the curve at two different times. Automatically selected IDAIFs using the cluster- (red) and SVD-based method (green).

Comparing 100 repetitions of the automatic IDAIF selection algorithms for each dataset, the SVD-based method was more stable ($f_{robust} \approx 0$) than the clustering algorithm ($f_{robust} \approx 10^{-9}$ - 10^{-6} ms^{-2}). In 41 of 44 datasets, the SVD-based method achieved higher, narrower or earlier peaks than the clustering approach. For both algorithms, computation time was comparable (about 60 s), and the selected voxels were located in reasonable regions around large vessels. Figure 4.7 shows locations of selected IDAIF voxels (upper part) and the corresponding time courses (lower part) for two patient examples.

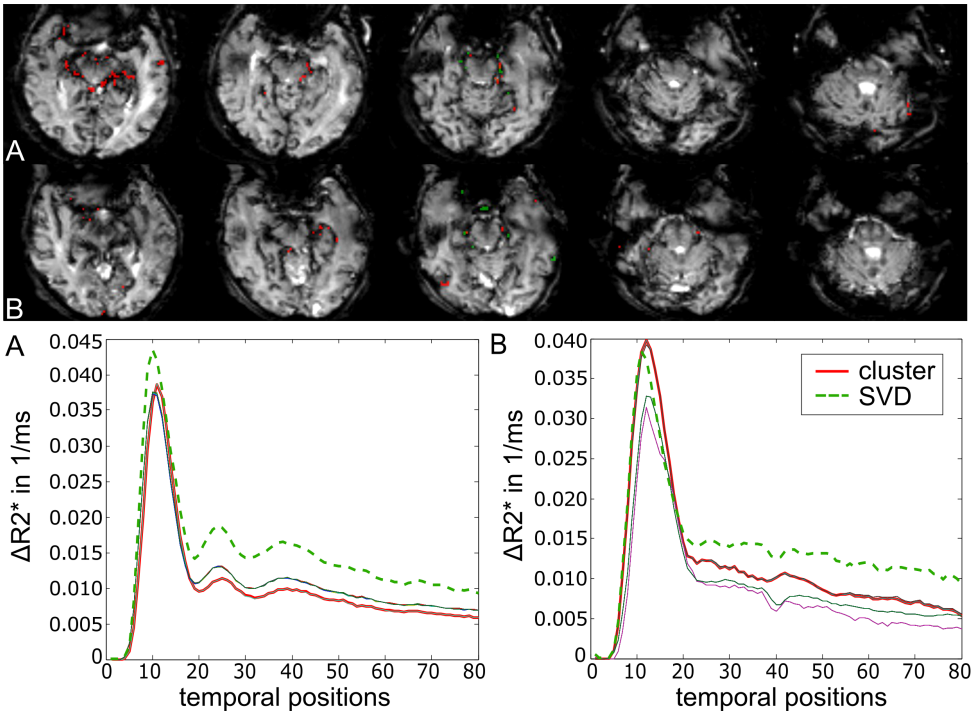

Figure 4.7: IDAIF locations (top panels) and corresponding curves (bottom panels) of IDAIFs selected by clustering (red) and by SVD (green) from two representative patient examples (A and B). The thin solid colored curves represent all individual cluster selected AIFs of the 100 repetitions.

4.4 Comparison of Multiple Extravasation Correction Methods in Patient Data

The impact of extravasation correction techniques on CBV values was primarily analyzed for patient data acquired with a PB taken from the hypoxia study group (section 3.7.5).

4.4.1 Stability of Fitting Procedures

For methods I, II and IV, the fit of Eq. (3.6) directly quantifies K_2. The numerical fitting procedures worked properly for all methods. Figure 4.8-A shows an example of fitting results for methods I and II within one voxel together with the estimated parameter K_2. Generally, method II had lower fitting residuals than methods I and IV. Since for method IV (data not shown) each voxel's individual reference curve was obtained via SVD, this algorithm was prone to noise-related artifacts, e.g. oscillations at the end of the curve and negative $\Delta R2^*$ curves.

For variants of method III, the fit of $R(t)$ with a Lorentzian function (Eq. (3.10)) worked also reasonably well. Similar to simulation results (section 4.1.2), the estimated

T_c was larger if deconvolution was done with TiSVD. Figure 4.8-B displays one example of the voxel–wisely calculated and fitted $R(t)$. The fit of $R(t)$ generated by TiSVD showed lower residuals than the one generated with the sSVD due to larger oscillations in the latter one. If ATC was done before SVD, the residuals were generally reduced and became more homogeneous across the brain.

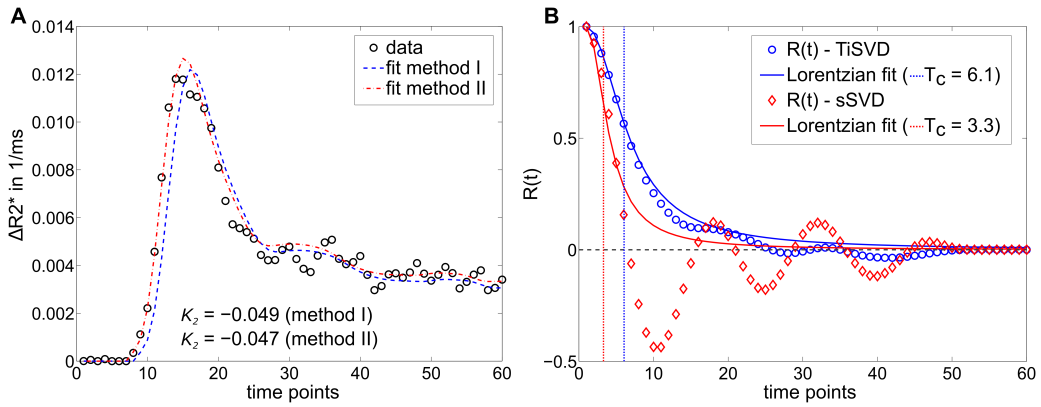

Figure 4.8: Illustration of the numerical fit quality in a typical single voxel data example. (A) Fit of the ΔR2* time course (o) with methods I (blue) and II (red). (B) Fit of the residue function R(t), generated with TiSVD (blue) and sSVD (red), with a Lorentzian function (method III). Please note that methods I and II yield comparable values for the fitting parameter K_2, while the fitted mean transit time (T_c), in units of time points, is nearly doubled for TiSVD compared to sSVD.

4.4.2 Effect of Post-Processing Extravasation Correction Methods on CBV

Generally, absolute CBV values were highly heterogeneous and clearly higher than expected. The correction methods based on post-processing did alter CBV values in healthy and diseased tissue. By far the largest correction effect for all tissue types was observed for method IV. While methods I, II and III (sSVD) mostly increased CBV values, correction methods III (TiSVD) and IV rather reduced CBV values. Furthermore, the leakage correction mainly reduced the standard deviations of CBV values compared to those of uncorrected CBV values.

The leakage corrected, absolute CBV in healthy tissue ranged between 2.4 ± 0.9 ml/100 g and 15.3 ± 4.1 ml/100 g in WM and between 3.9 ± 1.3 ml/100 g and 24.0 ± 5.1 ml/100 g in GM. The smallest values were found by method IV, the largest by method II. In contrast, averaged normalized CBV (nCBV) values in WM (1.7 ± 0.1 %) and GM (2.7 ± 0.1 %) were stable among post-processing correction methods. Here, values in WM ranged from 1.6 ± 0.1 % to 1.7 ± 0.2 % and in GM from 2.5 ± 1.6 % to 2.9 ± 0.4 % for the different correction methods. In healthy tissue, the correction effect was statistically significant for all methods, except for method III (sSVD,

ATC). Nevertheless, in VOI_{WM}, VOI_{GM} and VOI_{EDE} differences between uncorrected and corrected CBV values were relatively low.

Averaged absolute CBV and nCBV values in tumorous tissue (VOI_{CET}, VOI_{T2T}, VOI_{EDE}) of all patients with a pre-dose are summarized in Table 4.1, whereby asterisks mark significant corrections. After normalization, the CBVs in tumorous tissue were also more homogeneous, but still showed significant correction effects. The nCBV was predominantly lowered after correction. Exceptions were method III (TiSVD) and method III (sSVD, ATC). However, the slight increase in those nCBVs was not significant. Generally, correction effects of method III variants were small compared to those of methods I, II and IV.

Table 4.1: Averaged absolute CBV and normalized nCBV (normalization to CBV of healthy WM = 1.5 %) values (acquired with PB) in edema (VOI_{EDE}), solid tumor (VOI_{T2T}) and contrast enhancing tumor tissue (VOI_{CET}). Significant differences to corresponding uncorrected CBVs are indicated with *, if $p < 0.001$ and $^{+}$, if $p < 0.05$.

method	VOI_{EDE} (n = 35)		VOI_{T2T} (n = 31)		VOI_{CET} (n = 31)	
	CBV in ml/100 g	nCBV in %	CBV in ml/100 g	nCBV in %	CBV in ml/100 g	nCBV in %
unc 1	13.6 ± 5.7	1.9 ± 0.8	17.8 ± 7.0	2.9 ± 2.2	35.5 ± 13.6	6.1 ± 5.3
method I	15.1 ± 6.6*	1.8 ± 0.6*	20.1 ± 7.2*	2.5 ± 0.8+	35.6 ± 12.2	4.7 ± 1.9 *
method II	17.8 ± 7.1*	1.8 ± 0.7	22.5 ± 7.7*	2.5 ± 0.8+	41.8 ± 13.6*	4.8 ± 2.0 *
method IV sSVD	2.7 ± 1.2*	1.8 ± 0.7+	3.5 ± 1.5*	2.5 ± 0.7+	6.1 ± 2.1*	4.4 ± 1.4*
-unc 2	11.0 ± 5.4	2.0 ± 0.9	14.0 ± 7.7	2.7 ± 1.0	30.6 ± 18.2	5.6 ± 2.4
-method III TiSVD	12.3 ± 6.3	2.0 ± 0.8	15.8 ± 6.8+	2.6 ± 0.9	32.8 ± 12.7	5.6 ± 2.1
-unc 2	7.1 ± 3.0	2.0 ± 0.8	9.0 ± 3.9	2.6 ± 0.9	19.2 ± 9.4	5.4 ± 2.1
-method III sSVD, ATC	6.2 ± 2.6*	2.0 ± 0.8+	7.9 ± 3.3*	2.6 ± 1.0+	17.3 ± 7.6*	5.8 ± 2.2+
-unc 2	12.2 ± 7.8	2.1 ± 1.0	14.4 ± 7.7	2.7 ± 1.1	33.2 ± 23.3	5.8 ± 2.7
-method III TiSVD, ATC	12.2 ± 5.9	2.1 ± 1.0	16.0 ± 7.0	2.7 ± 0.9	33.3 ± 13.5	6.0 ± 2.8
-unc 2	9.9 ± 11.6	2.5 ± 2.9	10.7 ± 9.5	3.1 ± 2.5	23.9 ± 20.6	6.7 ± 7.4
-method III	6.3 ± 3.3*	2.2 ± 1.4+	8.3 ± 3.6*	2.7 ± 1.0	18.1 ± 7.6*	6.3 ± 3.0*

4.4.3 Correlations between Methods

The correlation between absolute CBV values obtained by different methods was moderate to strong for all investigated VOIs. The best correlations were found between averaged CBVs obtained by methods I and II ($r_{CET} = 0.91$) and between those obtained by the four variants of method III ($r_{CET} = 0.85 \pm 0.08$). Figure 4.9 shows correlations between averaged CBV values obtained by method I and those obtained by all other methods. For all patients, CBV values averaged over VOI_{WM}, VOI_{GM} and VOI_{CET} are

displayed. While CBVs of methods I, II and III (sSVD) were in the same order with regard to absolute values, method III (TiSVD) generated smaller and method IV lowest absolute CBVs.

Slightly stronger correlations were seen for normalized CBVs. The worst correlations with $nCBV_{method\ I}$ and the largest variances were observed for arrival time corrected nCBV values of method III variants (Table 4.1, section 4.5.2). Figure 4.10 shows the correlation of averaged $nCBV_{CET}$ for all patients with three visible outliers. The red arrow indicates the only grade II patient with CET. The blue and green arrows indicate patients where either the ATC or the SVD itself introduced artifacts. A similar behavior demonstrated voxel-wise correlations.

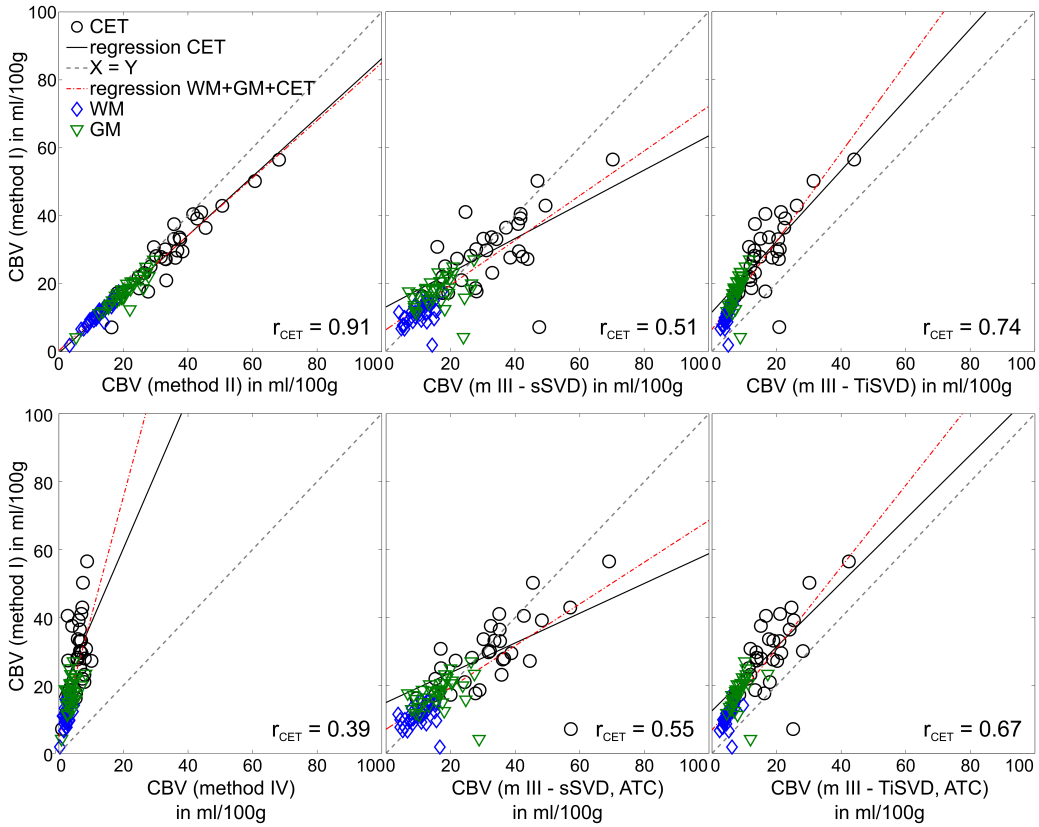

Figure 4.9: Correlation plots of absolute VOI averaged CBV values for VOI_{CET} (black circle), VOI_{WM} (blue diamond) and VOI_{GM} (green triangle) and all patients. Methods II to IV are compared to method I. The black solid line represents the regression for CET values only; the red dashed-dotted line represents the regression of all values; the gray dashed line indicates the unity line of complete equality. r_{CET} = correlation coefficient for the regression of CET values.

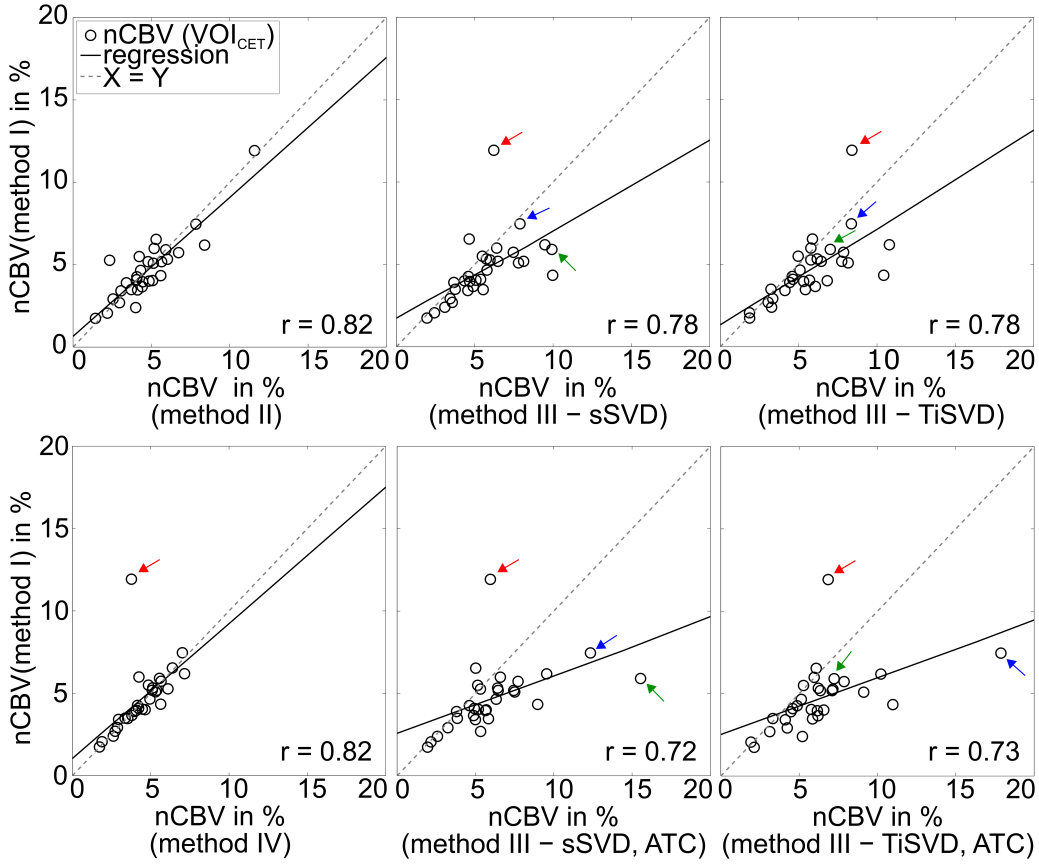

Figure 4.10: Correlation plot of normalized VOI averaged nCBVs in VOI_{CET} (black circles) for all patients. Methods II to IV are compared to method I. Arrows indicate data from individual patients: the only grade II tumor with CET (red), patients with analysis errors introduced by the arrival time correction (ATC, blue) and sSVD (green), respectively. r = correlation coefficient.

4.4.4 Effect of Integration Interval on CBV Acquired with Pre-dose

The influence of the integration interval was studied primarily for CBV computations based on the integration of the concentration-time curves (CTCs) including all patients that received a pre-dose (section 3.1.2). This comprised uncorrected $CBV_{unc\,1}$ and corrected CBVs of methods I, II and IV.

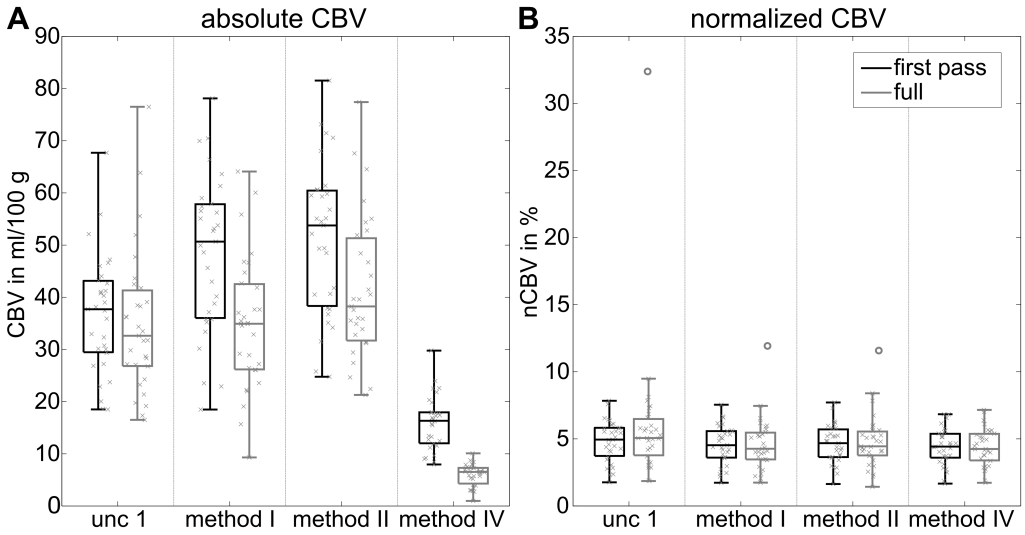

Figure 4.11: Effect of integration interval on CBV calculations based on the integration of the concentration-time curve. Boxplot of (A) absolute CBV and (B) normalized CBV values averaged in VOI_{CET} for all patients (n = 31). Individual patient values are indicated by crosses. The boxes contain all values between the first and third quartile, the line inside marks the median, the whiskers reach from minimum to maximum, and outliers are indicated by circles.

For absolute CBV values, the integration over the first pass of the curve yielded higher values than the integration of the complete time course (Figure 4.11-A). In tissue with CA extravasation (VOI_{CET}) this resulted in a mean difference of -1.8 ± 6.1 ml/100 g (-9 %) for uncorrected $CBV_{unc\,1}$, -13.5 ± 8.7 ml/100 g (-50 %) for method I, -9.7 ± 8.2 ml/100 g (-27 %) for method II and -10.0 ± 4.9 ml/100 g (-230 %) for method IV. Because $CBV_{method\,IV}$ was small compared to the CBVs of all other methods, values of CBV_{full} (VOI_{CET}: 6.0 ± 2.2 ml/100 g) were almost tripled when first pass integration was used instead (CBV_{fp} in VOI_{CET}: 16.0 ± 4.3 ml/100g).
With regard to means of normalized CBV_{CET}, the integration interval only had a minor impact (Figure 4.11-B). The largest difference was detected for the uncorrected nCBV ($nCBV_{unc\,1}$) with a percentage deviation of 7 ± 17 %. However, on visual inspection, differences in parameter maps were evident for nearly all methods (Figure 4.16, Figure 4.14).

4.5 Evaluation of Post-Processing Methods Using Two Boli

In a small subgroup of patients from the hypoxia study (n = 8), CBV could be derived from two sets of DSC data acquired during two consecutive CA boli. At the same time, the first dose served as a pre-bolus to minimize T1 leakage effects in the second acquisition (section 3.2.1). Using these data, the relationship between signal and CA

concentration as well as the impact of slice time (section 3.2.1) and arrival time correction were analyzed. If not stated otherwise, the complete time courses were integrated by default, however, a possible positive impact of first pass integration on the consistency of both boli was also investigated. Hypothesizing that appropriate post-processing reduces the significance of the pre-bolus technique, the agreement between CBV values derived from the first and second bolus was used as a quality criterion to identify the best-suited leakage correction technique.

4.5.1 Conformity between First and Second Bolus

In order to characterize the curve shapes of time series acquired during the first and second dose, the summary parameters rPH and rPSR (section 3.1.1) were compared in CET. A weakly significant difference was found for rPSR, which is an indicator for extravasation effects. Figure 4.12-B shows that rPSR values of the first and the second bolus are higher and lower than one, respectively. With respect to the evolution of rPSR, this indicates a signal overshoot (T1 effects) for the first bolus acquisition. For rPH, being proportional to CBV, values were comparable between both acquisitions (Figure 4.12-A).

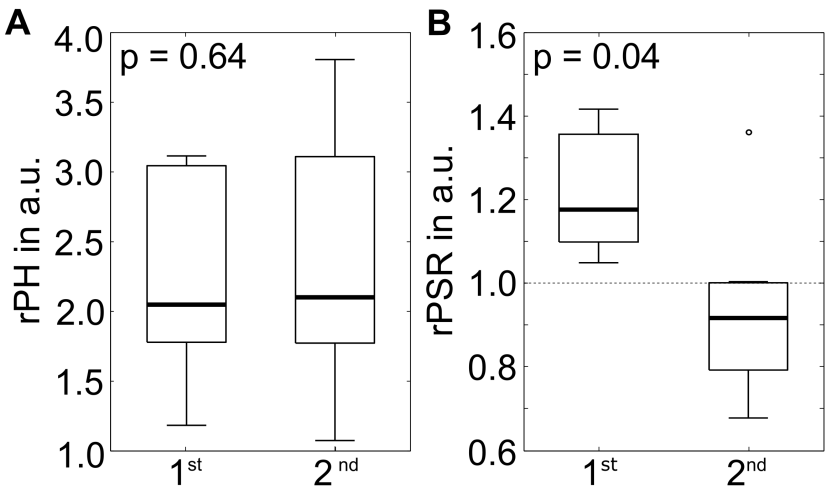

Figure 4.12: Boxplots of rPH (A) and rPSR (B) in VOI_{CET} for the first and second bolus (n = 8). A significant difference was only found for rPSR ($p < 0.05$, Wilcoxon signed rank test). The bold line indicates the median, the box covers the range between the 25th and 75th quantile, and the whiskers reach from minimum to maximum.

With regard to CBV, the use of a pre-bolus reduced the variance across patients. In nearly all VOIs and patients, the absolute CBV values were higher for data acquired with PB (CBV_{2nd}). The post-processing reduced, but did not eliminate this difference between CBVs of both boli. Therefore, after leakage correction the CBV values calculated from the first bolus (CBV_{1st}) were still smaller than the CBV values calculated from the second bolus (CBV_{2nd}). VOI- and voxel-wise correlations between CBV values, obtained using

the first and the second bolus, were improved after post-processing ($r_{CET,before} \leq 0.5$, $r_{CET,after} \geq 0.6$), except for method IV.

Similar to absolute CBV, $nCBV_{1st}$ (without PB) was smaller than $nCBV_{2nd}$ (with PB). The post-processing methods reduced the variance of nCBV within the tumor regions as well as between patients compared to the corresponding uncorrected nCBV values. Applied to data without PB, post-processing predominantly increased nCBV values. Uncorrected nCBV maps calculated from the first bolus acquisition demonstrated many zeros (clipped negative values). The leakage correction eliminated or at least reduced the amount of those zero values (Figure 4.13). Following, in VOI_{CET} the averaged nCBV values of all patients (n = 8) and methods increased by about 52 % from 2.1 ± 1.2 % (without correction) to 3.2 ± 0.7 % (with post-processing correction). For acquisitions with PB, nearly all correction methods reduced nCBV values. Averaged over all correction methods of the same patients, $nCBV_{CET}$ was 6.0 ± 0.8 % before and 5.3 ± 1.0 % (-12 %) after leakage correction.

Figure 4.13 shows one example of voxel-wise correlations between $nCBV_{CET}$ of the first and second bolus for three correction methods and the corresponding uncorrected data. The correlation coefficient r increased after post-processing correction from 0.67 to 0.98 (A), 0.46 to 0.92 (B) and 0.49 to 0.71 (C). In most comparisons of $nCBV_{1st}$ and $nCBV_{2nd}$, voxel values correlated significantly with each other ($p < 0.001$). The worst correlations were encountered for method IV. The strongest correlations combined with the highest accordance between nCBV values obtained from both boli (RPC < 2.8 %) were found for method I (Figure 4.15-B).

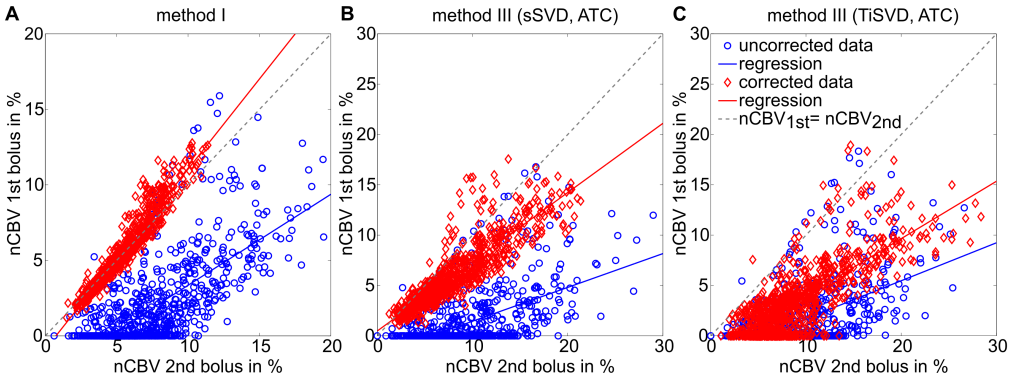

Figure 4.13: Effect of post-processing leakage correction for one representative patient. Voxel-wise correlations of nCBV values (normalized to healthy WM) in contrast enhancing tissue (CET) between 1st and 2nd bolus before (blue) and after leakage correction (red) with different methods: (A) method I, (B) method III (sSVD, ATC), (C) method III (TiSVD, ATC).

Figure 4.14 represents a single slice of one exemplary patient for all acquisitions and all post-processing methods. On the one hand, the described discrepancies can be observed

between methods and acquisition modes. On the other hand, also the homogenizing effects of the second bolus and the first pass integration range are visually perceptible.

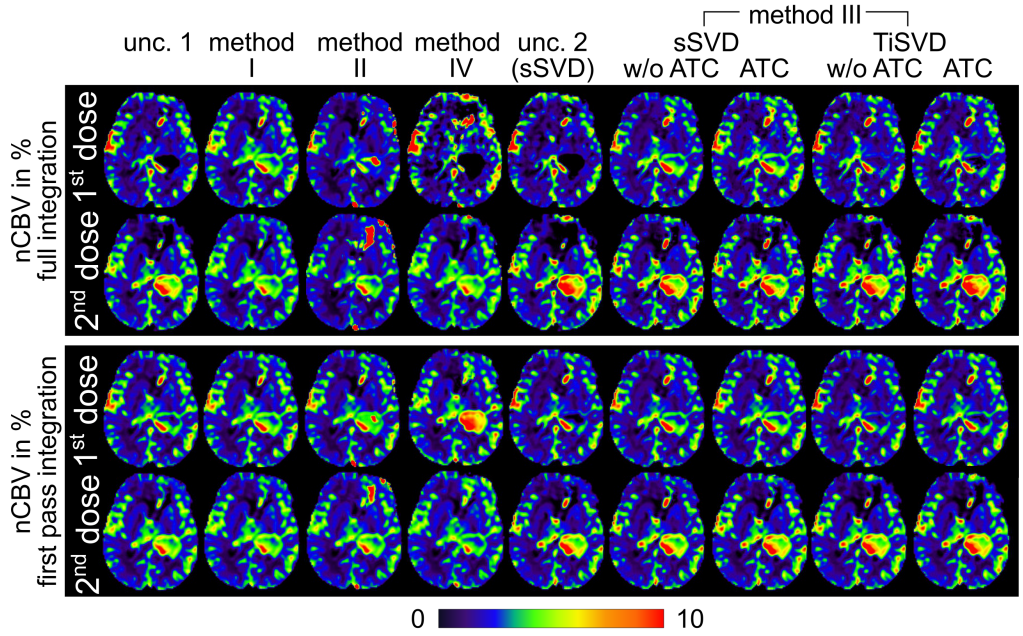

Figure 4.14: One slice of an exemplary patient with glioblastoma. The rows present complete overviews of all investigated leakage correction methods. Upper two rows: full time course integration range for the first and second bolus acquisitions. Bottom two rows: first pass only integration range for the first and second bolus acquisitions. $nCBV_{unc\,2}$ is only shown for sSVD calculation (other three maps were visually similar). w/o ATC = without arrival time correction. Colorbar shows nCBV values in %.

For DSC acquisitions with PB, the integration range was shown to have a high impact on absolute CBV (chapter 4.4.4). Without an initial pre-dose (CBV_{1st}) the differences were much higher. Generally, absolute CBV_{fp} values were again larger than CBV_{full} values, irrespective of whether they were uncorrected or corrected for leakage. In healthy tissue, the integration range affected SVD-based techniques to a lesser extent.

In CET, if uncorrected for leakage, estimated CBVs integrated over the full time course were smaller for both boli. Exceptions were values of $CBV_{unc\,2}$ that were based on TiSVD. Here, CBV_{1st} increased and CBV_{2nd} decreased using first pass integration. Although differences between both boli diminished for all uncorrected CBVs using first pass integration, TiSVD-based methods showed the smallest absolute deviations. Furthermore, the correlation coefficient between $CBV_{unc\,1}$ values of the first and second bolus increased from $r_{full} = 0.34$ (full integration) to $r_{fp} = 0.86$ (first pass integration). The correlation coefficient between $CBV_{unc\,2}$ values of the first and second bolus also slightly increased with first pass integration, but remained below 0.1.

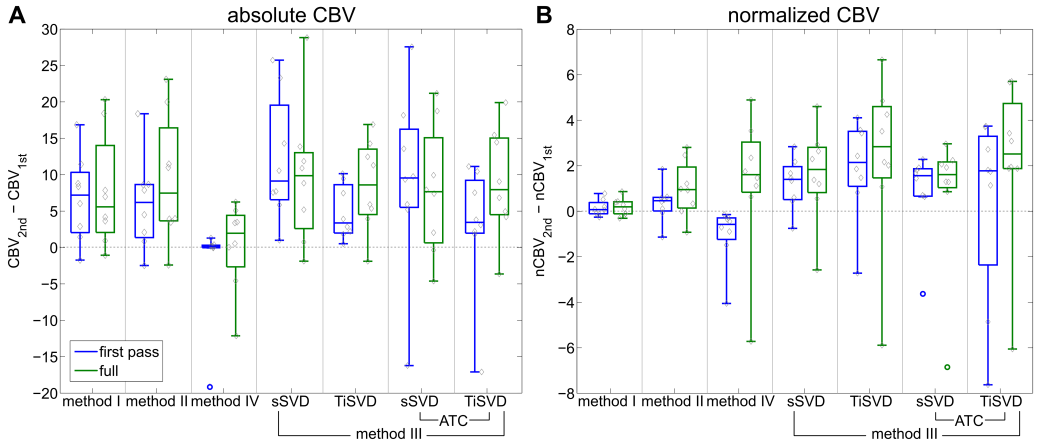

Figure 4.15: Boxplots of differences between extravasation corrected CBV values of 1st (CBV_{1st}) and 2nd bolus (CBV_{2nd}) for two integration intervals in VOI_{CET}. (A) Differences of absolute CBVs and (B) normalized CBVs for first pass integration (blue) and full time course integration (green). The boxes contain all values between the first and third quartile, the line inside marks the median, the whiskers reach from minimum to maximum and circles are outliers. The gray diamonds indicate individual patient averages (n = 8) and the horizontal dashed gray lines indicate zero difference.

Combining leakage correction and first pass integration usually improved the accordance between absolute CBV values obtained from both boli (Figure 4.15-A). Only methods I and III (sSVD, ATC) resulted in increased median differences if integration was restricted to the first pass. CBV_{1st} and CBV_{2nd} agreed best with method IV using the first pass integration. Here, besides the similarity of absolute values also the correlation increased compared to that obtained with full integration (r_{full} = 0.14 to r_{fp} = 0.72).

The first pass integration also homogenized nCBV values, especially $nCBV_{1st}$, among all correction methods. Figure 4.14 illustrates this for one exemplary slice of one patient. For all correction methods, the differences between first and second dose $nCBV_{CET}$ values were clearly reduced (Figure 4.15-B). Normalized $CBV_{method\ I}$ values showed nearly no difference between both integration ranges. Overall, using the first pass integration, nCBV maps seemed to be less noisy, especially for data acquired with the smaller first CA dose (Figure 4.16).

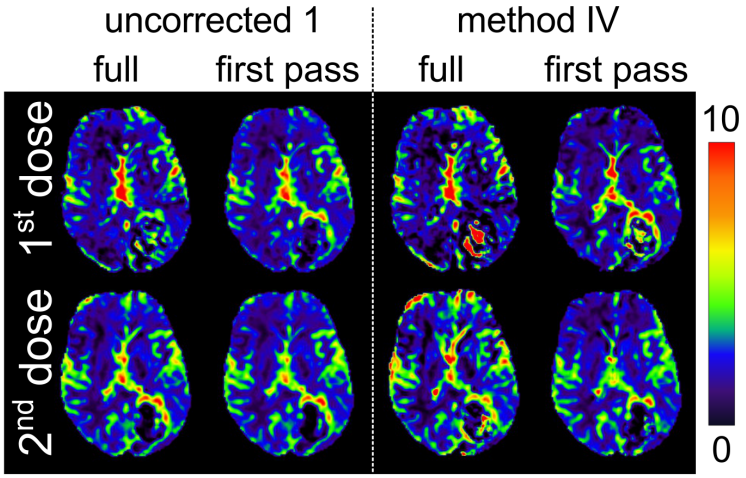

Figure 4.16: One slice of an exemplary patient with glioblastoma showing the influence of the integration intervals (full time course versus first pass only) on normalized CBV. First row: $nCBV_{unc\ 1}$ and $nCBV_{method\ IV}$ for the first bolus. Second row: $nCBV_{unc\ 1}$ and $nCBV_{method\ IV}$ for the second bolus.

4.5.2 Effects of Timing Problems

The interleaved acquisition scheme of the 2D EPI sequence introduced artifacts due to significant timing differences between neighboring slices. This is most evident in time-to-peak (TTP) parameter maps (Figure 4.17), but also plays a role in the CBV evaluation. For the eight patients with two boli, a slice time correction (STC) technique was tested (section 3.7.2).

Figure 4.17 demonstrates the effect of slice timing and its correction on TTP maps. The obviously reduced variation of TTP between neighboring slices confirmed the correct assignment of acquisition times and the corresponding quality improvement after STC.

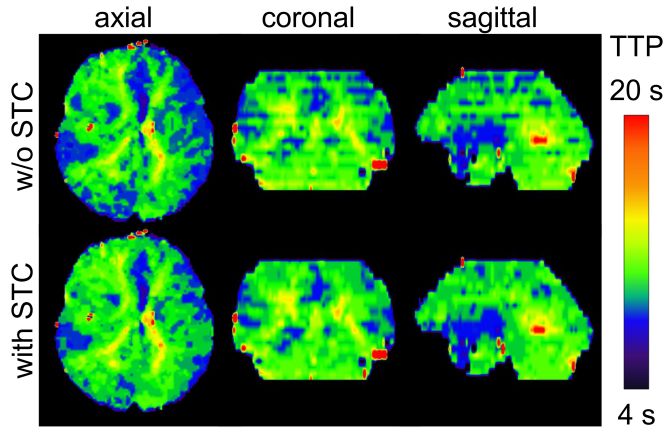

Figure 4.17: Influence of slice timing in interleaved acquisitions. Time-to-peak (TTP) maps of one patient in three orthogonal cuts (axial, coronal and sagittal slices from left to right), once without (w/o) and once with slice time correction (STC).

Besides STC, the effectiveness of TTP-based arrival time corrections (ATC_{TTP}) was analyzed with respect to the correction of slice timing effects for variants of method III (section 3.7.5). Although method II was introduced as a timing independent variant of method I (section 3.2.2), simulations demonstrated no benefit for CBV stability (section 4.1.5). Furthermore, the accordance between first and second bolus CBV values worsened with method II. Hence, the following section mainly focuses on variants of method III.

With respect to CBV calculations without any timing corrections, a less obvious but similar intensity pattern as in TTP maps was observed, and the fitting residuals of the SVD generated residue functions demonstrated similar alternating intensity patterns as TTP maps with every second slice that vanished using ATC. Figure 4.18 displays the difference between leakage corrected CBVs (TiSVD) with and without ATC, once analyzed without (upper row) and once with (bottom row) prior STC, for one exemplary patient. While without prior STC, the difference demonstrates an alternating intensity pattern, with STC only differences between WM and GM remained between arrival time corrected and uncorrected data. This indicates that ATC compensates timing differences between neighboring slices similar to STC and additionally those between WM and GM. However, the ATC can introduce instabilities in calculated perfusion maps as can be seen in Figure 4.10 (outliers), Figure 4.19 (sharply defined hotspots in less perfused areas) and simulation results (section 4.1.3).

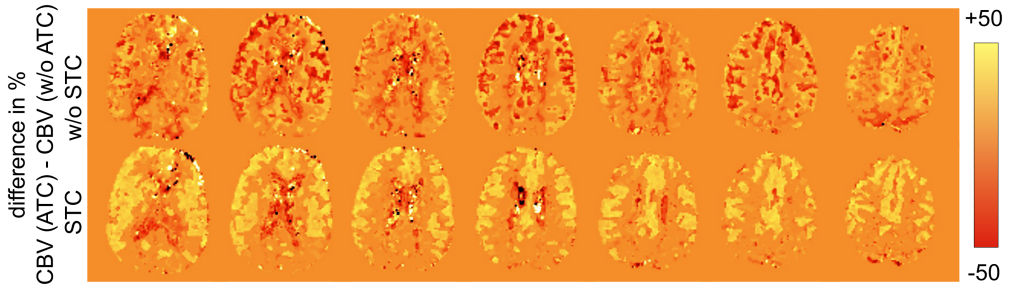

Figure 4.18: Impact of ATC without STC (upper row) and with a prior STC (bottom row). Shown are the percentage differences between absolute CBV values of method III (sSVD) with ATC minus without ATC. Colorbar in %.

Correlations of CBV_{CET} between first and second bolus demonstrated again a large variability across processing strategies. After STC, the accordance between CBVs of the first and second bolus became higher, compared to standard analysis (no STC). The differences between CBV_{1st} and CBV_{2nd} generally decreased by about 10 % to 45 %. One exception was method III (TiSVD) with an increased difference between CBV values of both boli of about 10 % after STC. The visual comparison showed a clear difference between absolute CBV parameter maps based on data that were uncorrected and corrected for slice timing differences (Figure 4.19). In comparison, the ATC only had a minor impact on CBV values and produced noisier parameter maps. Nevertheless, individual patients showed deviations from these rules. Because STC was done before IDAIF selection, these IDAIFs were compared with those found without prior STC. The observed differences between both IDAIF groups (with and without STC) imply that the major differences between absolute CBV values with and without STC could be due to a change of the selected IDAIF.

For nCBV values, neither STC nor ATC significantly influenced averaged CBV values. However, slight differences were noticeable in nCBV maps.

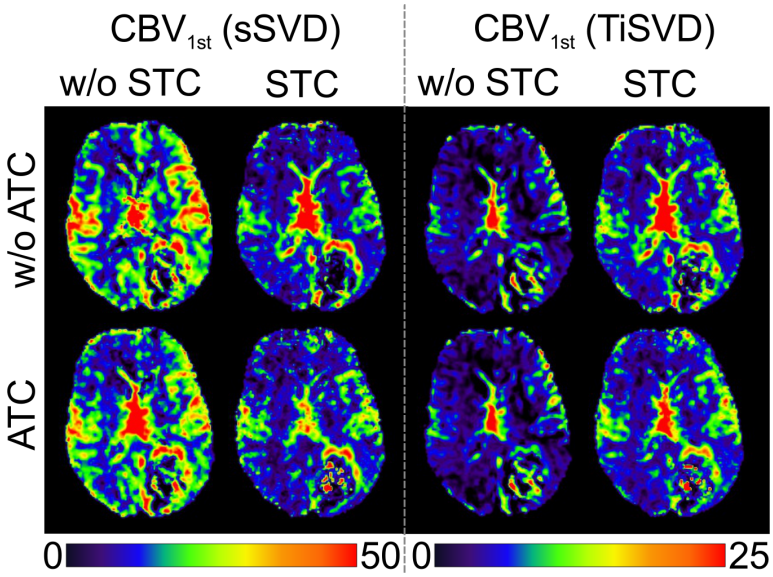

Figure 4.19: Impact of slice time correction (STC) and arrival time correction (ATC) on absolute CBV parameter maps obtained with method III for one slice of one exemplary patient. Shown are CBV maps of the first dose acquisition. First row without ATC; second row with ATC. Note that with STC and ATC sharply defined hotspots in less perfused tumor regions arise and that the range of values (color bars in ml/100 g) is different for sSVD and TiSVD.

4.5.3 Effect of a Non-Linear Relation between MR Signal and CA Concentration

The relationship between CA concentration and MR signal was assumed linear for all imaging voxels (tissue and arterial input). To study whether a non-linear relation for the IDAIF would diminish the observed CBV differences between first and second bolus, CBVs of method I were recalculated (section 3.7.4) converting the signal of IDAIF curves to CA concentration using a quadratic relationship (Eq. (2.15)). Figure 4.20 shows CBV_{1st} as a function of CBV_{2nd} for all voxels in VOI_{CET} for three exemplary patients. Across all (eight) patients, two showed a slightly higher CBV_{1st} for the linear assumption (patient A), two had a nearly perfect agreement with the linear assumption (patient B), and four showed a behavior similar to patient C. For all patients, values of both boli agreed best for the standard assumption of a linear relation between signal and concentration. Additional calculations based on the reference curve (averaged WM and GM) tested the reliability of a larger tissue relaxivity (r_2 = 0.0870 ms^{-1} mM^{-1}) in combination with the quadratic relation for the IDAIF. This relaxivity behavior proposed by Kjølby et al [49] resulted in much smaller $CBV_{method\ I}$ values for both boli (CBV_{1st}: 0.59 ± 0.23 ml/100 g, CBV_{2nd}: 1.05 ± 0.17 ml/100 g).

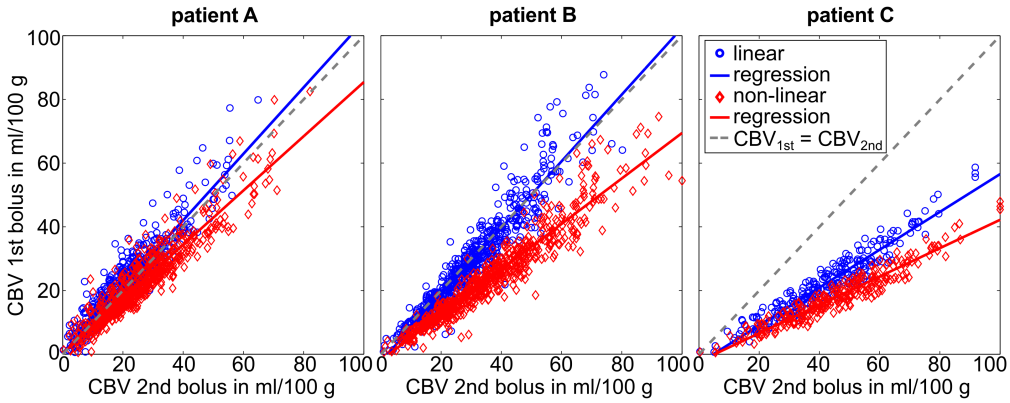

Figure 4.20: Influence of the assumed relationship between IDAIF signal and arterial concentration (linear (r_2 = 0.0053 ms^{-1} mM^{-1} [48]) vs. quadratic (Eq. (2.15))). Agreement between absolute CBV values in contrast-enhancing tissue of first and second bolus using the linear (blue) and the quadratic (red) signal to concentration relation for three patient examples.

4.6 Comparison to DCE-MRI and PET

In theory, measuring absolute CBV values should be possible with both, [^{18}F]FET-PET and DCE perfusion imaging, even though neither is a gold standard technique for CBV quantitation (sections 3.7.4, 3.7.5). Overall, 19 patients had evaluable data from DCE and DSC (with PB) acquisitions and 30 from PET and DSC (with PB). Contrast enhancing tumor tissue (CET) was found in 17 of the 19 patients with DCE.

Figure 4.21 shows exemplary CBV maps from two patients, where CBV_{PET} and CBV_{DCE} as well as CBV_{DSC} could be obtained. Since the spatial resolution of PET- and DCE-based parameter maps is lower, DSC-based CBV maps were additionally smoothed to facilitate visual inspection. Even though the spatial patterns of the CBV maps look similar at a first glance, absolute values were highly variable in general. One major difference due to image processing was the handling of vessels. They are highlighted in DCE- and cut out in PET-based maps (Figure 4.21).

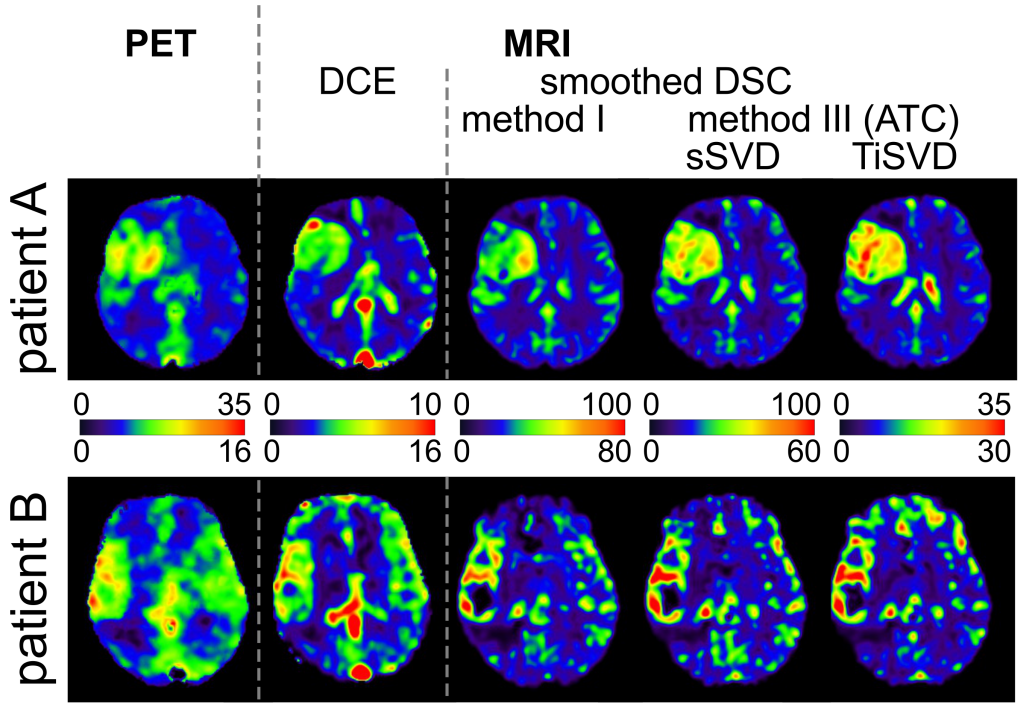

Figure 4.21: Exemplary CBV parameter maps obtained from dynamic [^{18}F]FET-PET, DCE-MRI and DSC-MRI in two patients A and B. One slice is shown for each patient and three extravasation corrected CBV_{DSC} maps (smoothed for visual inspection). Please note that the range of absolute CBV values largely disagrees as indicated by the different color codes that are displayed in the middle row of the figure in units of ml/100 g.

Comparison of DSC and DCE: CBV values obtained with DSC were generally higher than CBV_{DCE}. In WM CBV_{DCE} was 3.8 ± 2.2 ml/100 g. CBV_{DSC} values of method III (TiSVD) and method IV were closest with 5.2 ± 1.4 ml/100 g and 2.4 ± 0.9 ml/100 g, respectively. In GM, the CBV_{DCE} value of 6.5 ± 3.5 ml/100 g lay between those of methods IV (3.9 ± 1.3 ml/100 g) and III (TiSVD) (8.6 ± 2.3 ml/100 g). In tumorous tissue (VOI_{TUMOR}), only values of method IV, using a full integration, lay in a similar range as CBV_{DCE} (6.8 ± 4.2 ml/100 g) (Figure 4.22). When first pass integration was used, previously shown to improve the accordance of first and second bolus CBVs (chapter 4.5.1), absolute values of method IV increased by about 150 %, so they also exceeded values of CBV_{DCE}. Voxel-wise correlation results between CBV_{DSC} and CBV_{DCE} were heterogeneous for individual patients. Significant correlations between patient averages of CBV_{DCE} and CBV_{DSC} in VOI_{TUMOR} were only observed for methods I ($r = 0.61$, $p < 0.01$) and II ($r = 0.57$, $p < 0.05$). After normalization, averaged CBV_{DSC} values in VOI_{TUMOR} were between 3.7 ± 1.2 % (method IV) and 5.0 ± 2.5 % (method III – TiSVD, sSVD) and were thus still larger than $nCBV_{DCE}$ values (3.2 ± 1.3 %).

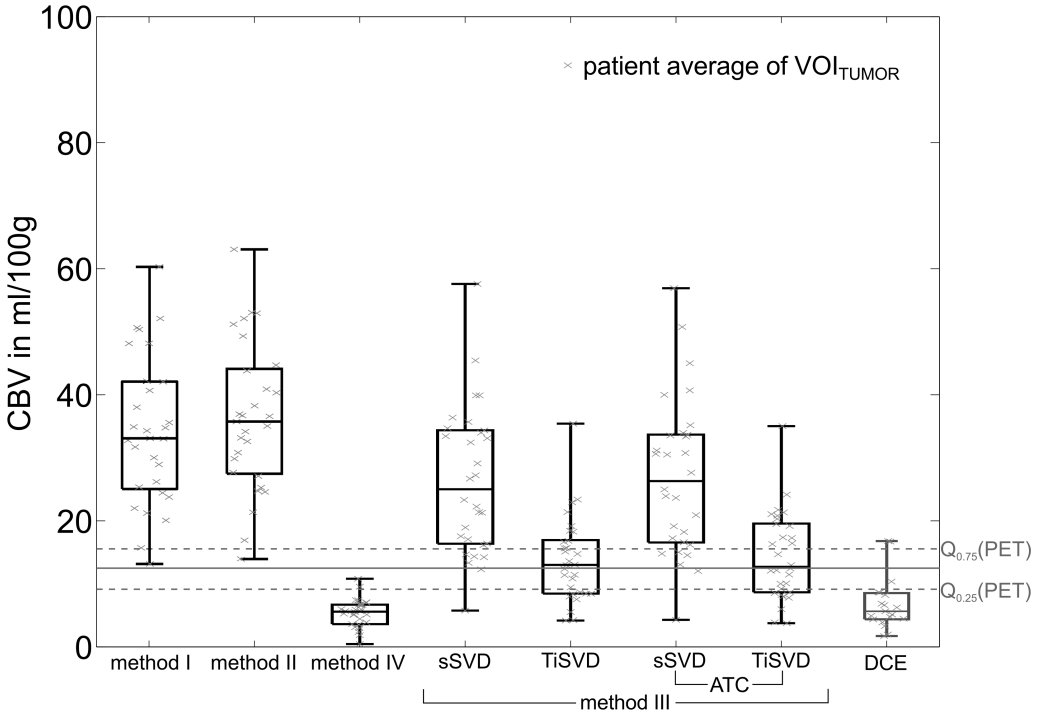

Figure 4.22: Absolute CBV_{DSC} values within VOI_{TUMOR} in comparison to CBV_{DCE} and CBV_{PET}. The boxes contain all values between the first and third quartile, the line inside marks the median, the whiskers reach from minimum to maximum. The crosses correspond to individual patient averages. The dashed gray lines marked with $Q_{0.75}$ and $Q_{0.25}$ (PET) represent the first and third quartile of CBV_{PET} and the solid gray line indicates the associated median.

Comparison of DSC and PET: Using CBV_{PET} as a reference, averaged CBV_{DSC} values agreed best for correction methods III using TiSVD (Figure 4.22). All other methods yielded mostly larger absolute values, except for method IV where values were smaller. This trend was found in all VOIs. An integration over the first pass only elevated values of $CBV_{method\ IV}$ to the range of CBV_{PET} values. Although the range of values overlapped, significant correlations between VOI averages of absolute CBV_{DSC} and CBV_{PET} values could not be observed for any of the methods. Partially detected voxel-based correlations between CBV_{PET} and CBV_{DSC} varied widely over patients. The improved VOI-wise correlation of CBV values (method IV vs. PET), using first pass instead of full integration, was reproduced in voxel-wise correlations of both modalities. As an example, the correlations for the two patients depicted in Figure 4.21 were found to be best for method I with full integration (patient A: $r = 0.70$) and method IV with first pass integration (patient B: $r = 0.59$). The worst correlations were achieved with methods III (TiSVD) (patient A: $r = 0.36$) and IV using full integration (patient B: $r = 0.55$).
After normalization of CBV_{DSC} and CBV_{PET}, all DSC-based nCBV values with leakage correction were still comparably high, but showed significant correlations with $nCBV_{PET}$. Figure 4.23 shows patient averages of $nCBV_{DSC}$ over $nCBV_{PET}$ in VOI_{TUMOR} for all

patients who got PET (n = 30). Their correlation coefficients ranged from 0.53 (p = 0.004) for method III (TiSVD, ATC) to 0.79 (p < 0.001) for method III (sSVD, ATC).

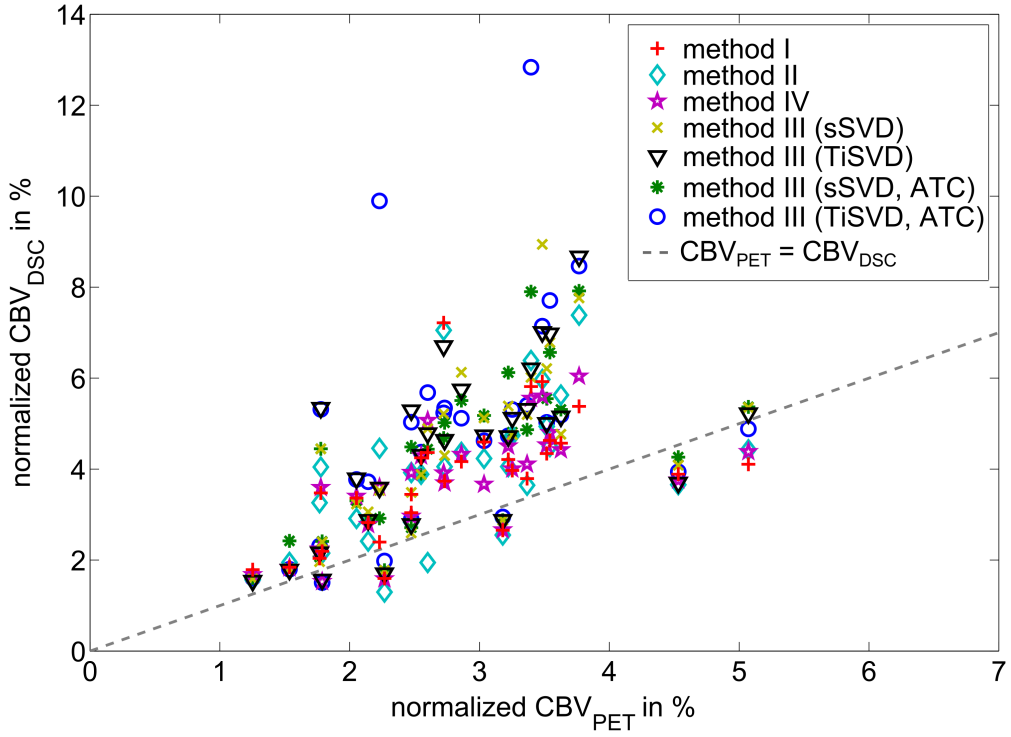

Figure 4.23: Scatterplot of patient averaged normalized CBV values for different methods (DSC-MRI vs. PET) in VOI_{TUMOR}. $nCBV_{DSC}$ for all leakage correction methods (with full integration interval) over $nCBV_{PET}$. The dashed gray line denotes equality of values.

4.7 Influence of Contrast Agent: Gd-DTPA versus Vasovist

In comparison to commonly used contrast agents like Gd-DTPA, gadofosveset trisodium (VASOVIST, Bayer Vital) transiently binds to human serum albumin. After this binding, Vasovist remains in the vascular space for a prolonged time (section 3.7.1). The first goal of this study was to evaluate the usability of Vasovist for magnetic resonance perfusion imaging as a high relaxivity contrast agent needing less CA dose. Furthermore, the reproducibility of CBV calculations with respect to different post-processing strategies should be evaluated.

Inspections of individual signal-time curves demonstrated significantly smaller signal drops for Vasovist data compared to Gd-DTPA data. In contrast, the rPH and rPSR values of VOI_{CET} (relative to normal WM) were comparable between both agents with slightly larger variances for Gd-DTPA (Figure 4.24).

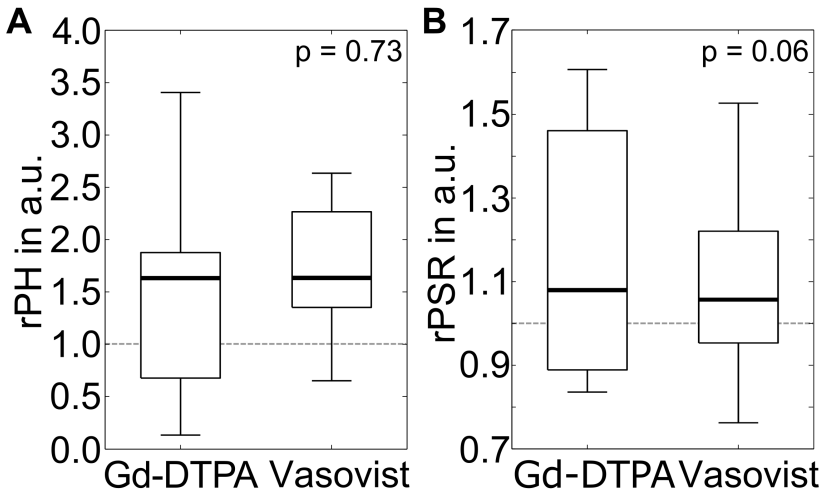

Figure 4.24: Relative peak height (rPH) (A) and relative percentage signal recovery (rPSR) (B) in VOI_{CET} for the Gd-DTPA and Vasovist (n = 10). The bold line indicates the median, the box comprises the range between the 25th and 75th quantile, the whiskers reach from minimum to maximum.

In contrast to similar rPH values, absolute CBV values acquired with Vasovist were smaller than those acquired with Gd-DTPA in all tissue types. This equally applies to data with and without extravasation correction. Figure 4.25 illustrates correlations between averaged CBV_{Vaso} and $CBV_{Gd\text{-}DTPA}$ in healthy (VOI_{WM}, VOI_{GM}) and diseased tissue (VOI_{EDE}, VOI_{T2T}, VOI_{CET}). The absolute CBV values showed significant correlations for all methods, whereas nCBV values of methods II and III showed less or even no correlation. Modifications like ATC and integration interval changed results similar to sections 4.5.2 and 4.5.1. For methods III, ATC improved correlations between absolute, but not between normalized CBV values (Figure 4.25-B). The first pass integration improved the correlation between CBVs obtained from both boli for nCBV of methods IV (r_{full} = 0.70, r_{fp} = 0.83) and for the uncorrected $nCBV_{unc\,1}$ (r_{full} = 0.75, r_{fp} = 0.84). Again, the best concordance was observed for normalized CBVs of method I (Figure 4.25-A, Figure 4.27).

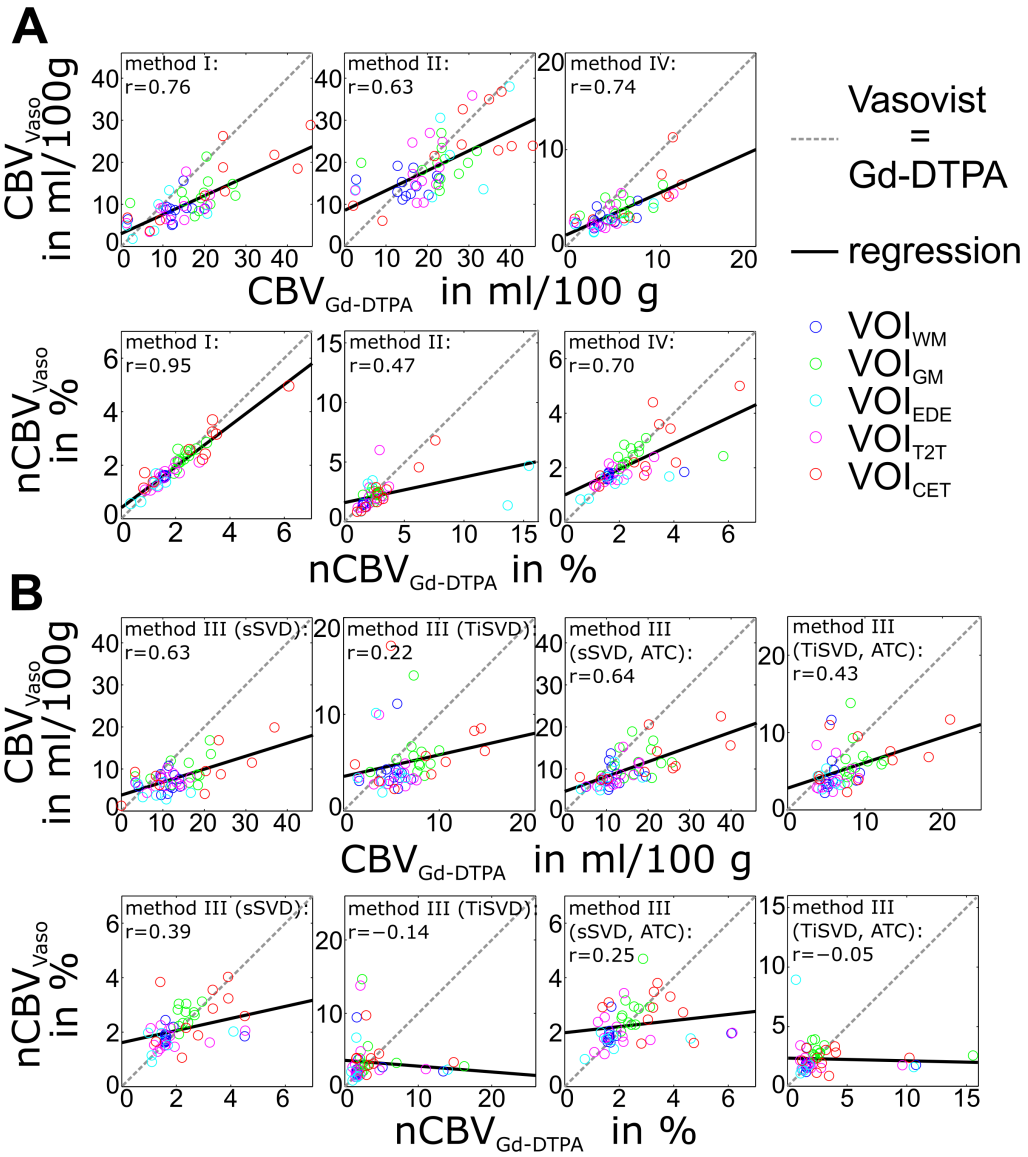

Figure 4.25: Influence of contrast agent. VOI averaged extravasation corrected CBV and nCBV values of all patients correlated between Vasovist (CBV_{Vaso}) and Gd-DTPA ($CBV_{Gd-DTPA}$). (A) Extravasation corrected CBV values of methods I, II, IV and (B) method III variants each in two rows: first row with absolute CBV, second row with normalized CBV. WM = white matter, GM = gray matter, EDE = edema, T2T = solid tumor, CET = contrast enhancing tumor tissue. r = correlation coefficient.

In accordance with the relationships of VOI averaged CBV values, voxel values of $nCBV_{Vaso}$ and $nCBV_{Gd-DTPA}$ correlated best using method I (Figure 4.26-B). However, voxel-wise correlations were generally problematic because Vasovist data appeared noisier. Leakage correction in any case equalized results between both CAs and improved quality of parameter maps, especially for CBV_{Vaso} (Figure 4.26, Figure 4.27).

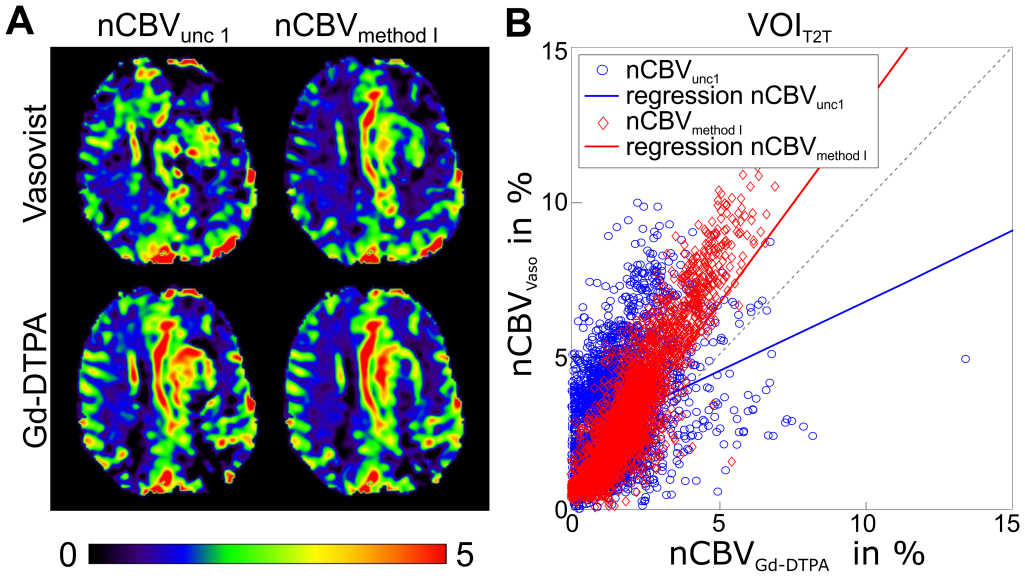

Figure 4.26: Influence of contrast agent. Comparison of Gd-DTPA and Vasovist-based nCBV parameter maps in one exemplary patient. (A) One slice of normalized CBV ($nCBV_{unc\ 1}$ and $nCBV_{method\ I}$) for both contrast agents in %. (B) Voxel-wise correlation of $nCBV_{VASO}$ and $nCBV_{Gd\text{-}DTPA}$ in solid tumor (VOI_{T2T}) without leakage correction (blue) and after correction with method I (red).

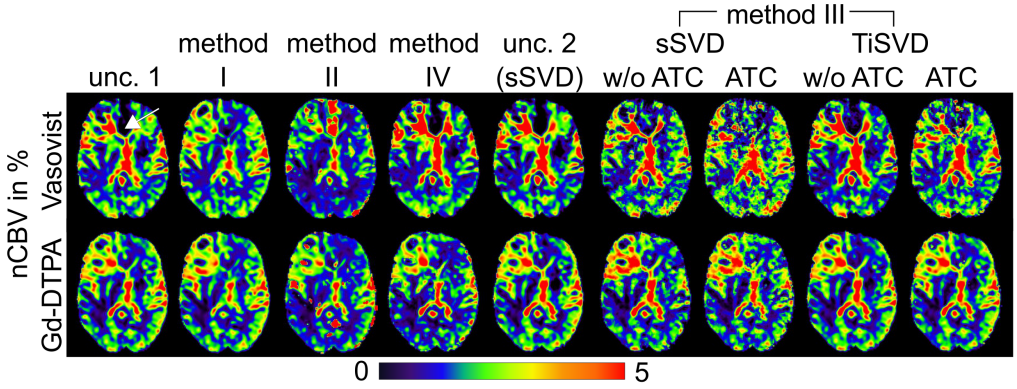

Figure 4.27: Influence of contrast agent. Exemplary slice of one patient's normalized CBV parameter maps for all post-processing methods. First row: Vasovist-based, second row, Gd-DTPA-based. The white arrow shows a large hole in Vasovist-based nCBVs that is not present in $nCBV_{Gd\text{-}DTPA}$ and was only partly corrected.

4.8 Vascular Permeability and Tumor Heterogeneity

The shape of DSC derived signal-time courses depends on numerous influencing factors (section 3.1.3). The effects of contrast agent extravasation on signal-time courses were simulated as a combination of initial tissue T1, CA extraction rate and blood flow using three tissue compartments. Within the context of the used correction methods, the signal-modifying leakage effects are represented by the extravasation correction parameter

K_2. In contrast, the transfer constant K^{trans} (Eq. (3.25)) is only determined by the tissue and vessel properties. To analyze the relation of K_2 and K^{trans} values, simulations and patient data analyses were used. Additionally, the impact of SNR and reference curves on K_2 was simulated. In patient data, the percentage of positive K_2 values within the tumor VOIs allowed the study of the heterogeneity of tumors (section 3.7.5).

Simulations: in order to optimize K_2 determination (method III, section 3.6.2), different starting points of the extravasation phase, i.e. averaging intervals, were simulated. In accordance with CBV results (section 4.1.2), K_2 of methods III changed with differently defined extravasation phases. With later thresholds, the calculated K_2s and their standard deviations increased. In other words, with shorter averaging intervals the estimated T2/T2* effects decreased and the estimated T1 effects of methods III increased. In general, the variance of K_2 values was high and input K^{trans} values could never be reproduced. Nevertheless, K_2 showed a certain dependence on the extravasation strength. With increasing K^{trans}, the K_2 values of methods I, II and III increased for T1 effects and decreased for T2/T2* effects. In contrast, K_2 values obtained by method IV only showed a small variation for T2/T2* effects, whereby K_2 values decreased for smaller input transfer rates. Furthermore, K_2 depended on the noise level, where a decreasing SNR increased standard deviations similar as for CBV. For methods I and II, K_2 depended on the applied reference curve, where different MTTs, CBFs and CBVs were used to imitate different reference tissue types. In contrast to CBV, the evaluation of those simulated reference curves showed smaller variations for K_2 values of method II compared to those of method I.

Comparison of correction methods: Using patient data from the hypoxia study group, the spatial distribution of K_2 values demonstrated large differences between methods. The percentage of predominant T1 effects ($K_2 > 0$) in VOI_{CET} over all patients with PB (n = 36) ranged between 2.4 ± 4.5 % for method IV and 55.0 ± 35.1 % for method III (sSVD, ATC). In the small subgroup of patients with two consecutive DSC scans (n = 8), K_2 was not reproducible and changed to more negative values for the second bolus. In the first bolus, without PB, a larger tumor area exhibited predominant T1 effects. Figure 4.28-A shows one patient example with color-coded K_2 maps of the first and second bolus. The red areas indicate positive, the blue ones negative values. Corresponding to this, Figure 4.28-B shows patient averages of the percentage tumor volume exhibiting T1 (red) and T2/T2* (blue) effects, respectively.

Figure 4.29 shows a voxel-wise correlation between K_2 values of methods II to IV against K_2 values of method I in VOI_{CET} of one representative patient with PB. Even though for several patients significant correlations were observed, the heterogeneity among patients was high. K_2 values obtained from the first and the second bolus did not correlate, and their differences became larger with increasing deviation from zero.

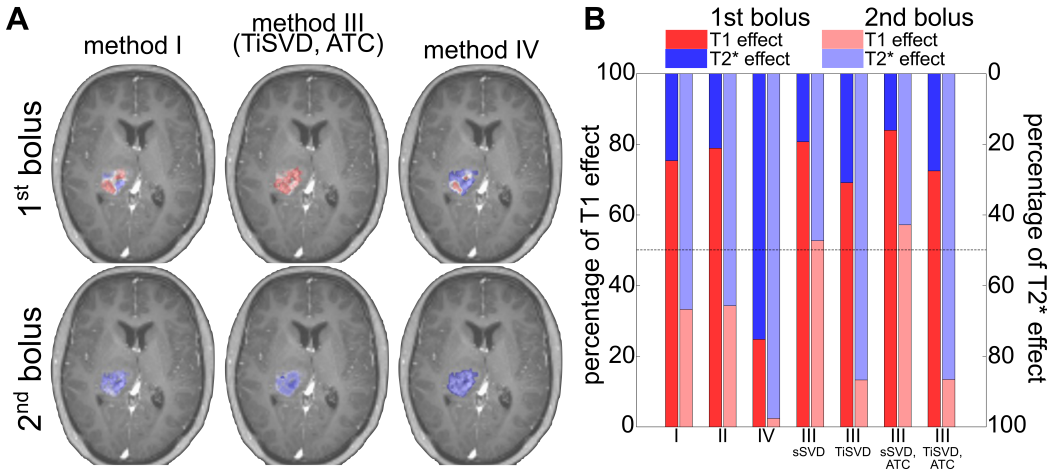

Figure 4.28: Predominant extravasation effects in patients, for the first and second bolus. (A) Example slices with color-coded K_2 (blue = T2/T2* effect, red = T1 effect) within the tumor region for 1st (top) and 2nd bolus (bottom). (B) Patient averages (n = 8) of respective percentages of T1 (red) and T2/T2* (blue) effects for 1st (deep colors) and 2nd (pale colors) bolus. Dotted line indicates 50 %.

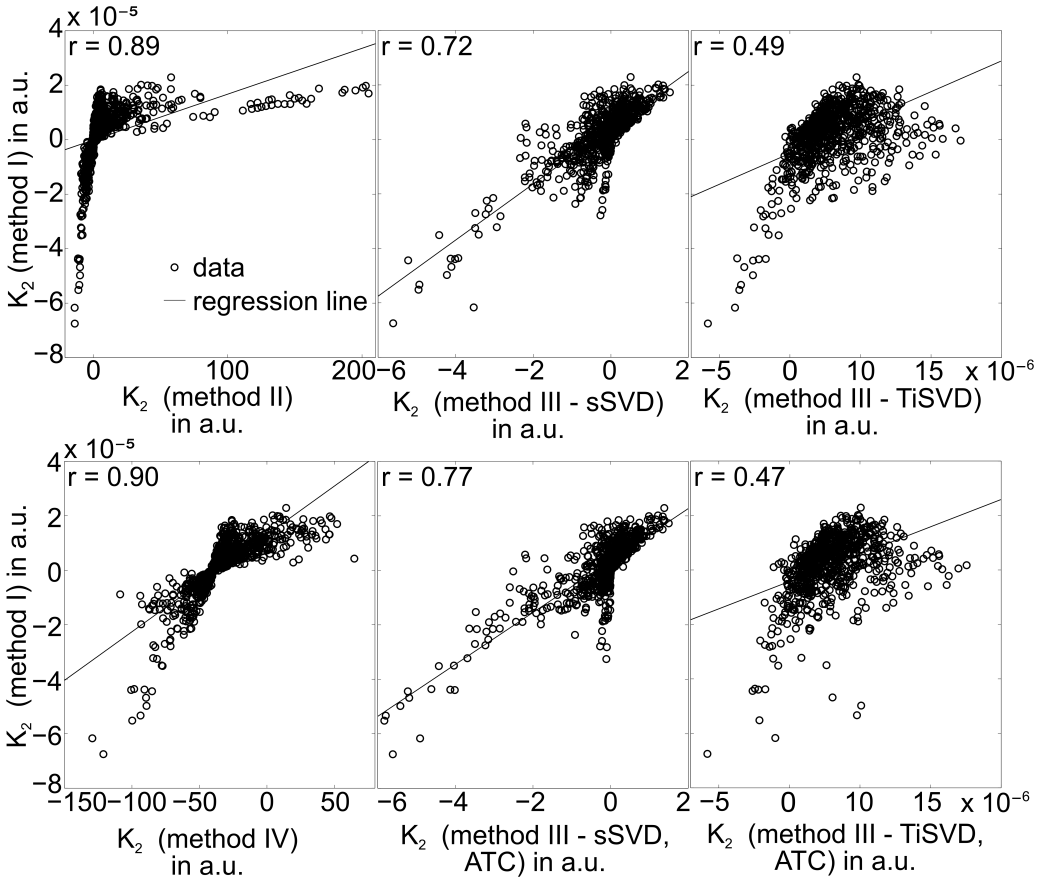

Figure 4.29: Voxel-wise correlation between K_2 values obtained with different methods in VOI_{CET} of one representative patient. Methods II to IV plotted against method I showing the regression line and the corresponding correlation coefficient r.

Comparison of contrast agents: Over the entire brain, K_2 values were different between both CAs, where K_2 values obtained with Vasovist were in parts higher than those obtained with Gd-DTPA. The relative amounts of both leakage effects were estimated to be similar for both CAs, when calculated by the same method. The voxel-wise concordance of K_2 values between both contrast agents was best for method I, which is in accordance with the similar rPSR values (section 4.7). One patient example of voxel-wise K_2 correlation in the solid tumor region (VOI_{T2T}) is shown in Figure 4.30-A.

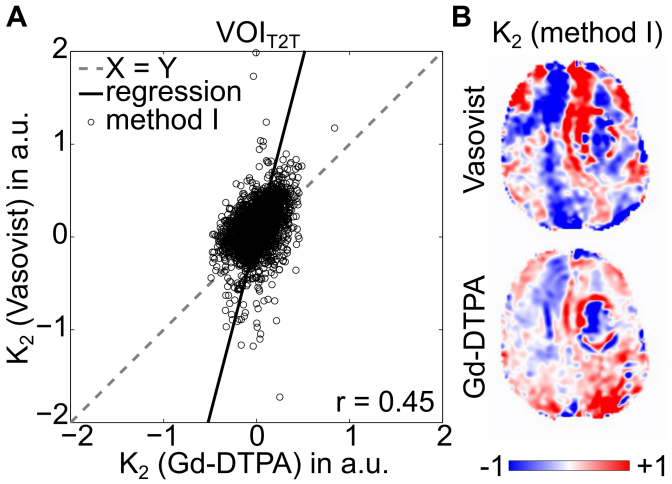

Figure 4.30: Comparison of K_2 values obtained from Vasovist and Gd-DTPA data for one exemplary patient. (A) Scatterplot of K_2 values obtained with method I and (B) one corresponding slice for each of the K_2 parameter maps: Vasovist against Gd-DTPA. All values are in arbitrary units. Positive K_2 values (T1 effects) are depicted in red, negative K_2 values (T2/T2* effects) in blue.

Relation of K^{trans} and K_2: Difficulties that had been observed in correlations between CBV_{DSC} and CBV_{DCE} (section 4.6), were also noted for correlations between the parameters K^{trans} (DCE) and K_2 (DSC). In most patients, K^{trans} values correlated best with K_2 of methods I, III (sSVD) and IV, even though the quality of correlations varied widely. Figure 4.31 shows the voxel-wise correlation between K^{trans} and K_2 (method I) for two exemplary patients. The Spearman correlation coefficient was slightly larger than the Pearson correlation coefficient indicating a non-linear relationship. Table 4.2 separately summarizes positive and negative median values of K_2 for all methods. Method IV generated the largest and method III (TiSVD) the smallest K_2 values.

Table 4.2: Positive and negative K_2 values obtained with each method; * = K^{trans}, all values in min^{-1}, medians as well as upper and lower quartiles of patient values in contrast enhancing tumor tissue (VOI_{CET}), (n = 17).

method	I	II	IV	III w/o ATC sSVD	III w/o ATC TiSVD	III with ATC sSVD	III with ATC TiSVD	DCE*
$K_2 > 0$ (0-Q_{75})	0.156 (0.308)	0.129 (0.499)	1.115 (3.590)	0.045 (0.123)	0.007 (0.011)	0.045 (0.124)	0.006 (0.020)	0.084 (0-0.222)
$K_2 < 0$ (Q_{25}-0)	-0.559 (-0.871)	-0.174 (-0.286)	-2.879 (-3.716)	-0.056 (-0.092)	-0.030 (-0.054)	-0.069 (-0.096)	-0.036 (-0.056)	

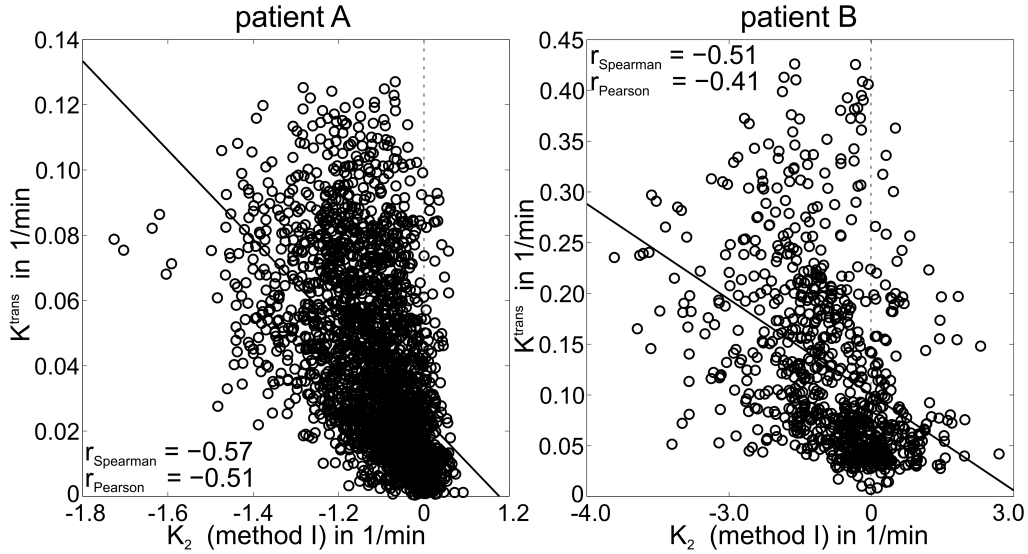

Figure 4.31: Voxel-wise comparison of K^{trans} versus K_2 (method I) within VOI_{CET}. Two patient examples showing rather good correlation results (patient A, patient B). The regression line in black. Correlation coefficients r for Spearman and Pearson correlations.

4.9 Impact of CBV Variations on rOEF

Besides $R2'$, CBV is the most important input parameter for calculation of the relative oxygen extraction fraction (rOEF), and, as could be seen in the previous sections, the variability of CBVs across different post-processing methods is huge. To estimate the expected effect on rOEF, a simulation with a range of realistic CBV deviations was done according to section 3.7.4. Additionally, as a preliminary test, the rOEF of two patients was calculated using four different nCBVs.

As detailed in section 3.7.5, assuming a CBV of 3 ml/100 g and an $R2'$ of 3.8 s^{-1} for the computation of rOEF at 3.0 T results in an rOEF of 0.4. Based on these values, a CBV underestimation by 50 % would lead to an rOEF overestimation of 100 %. If CBV was overestimated by 50 %, the rOEF would be underestimated by only 33 %. Figure 4.32

visualizes the influence of CBV variations on rOEF and shows that an overestimated CBV, which was found more often in results of the patient studies (see previous sections), had a minor effect on rOEF.

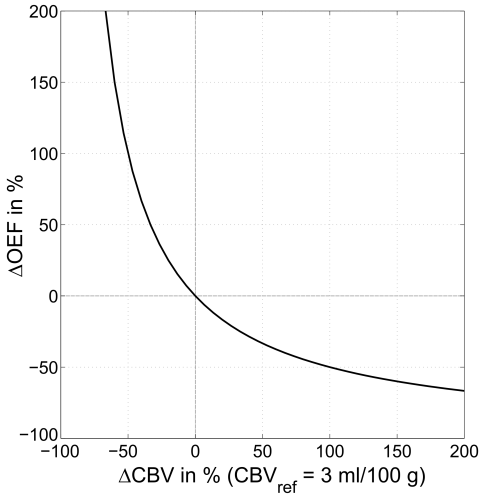

Figure 4.32: Impact of CBV variations on rOEF assuming a CBV of 3 ml/100 g and an *R2'* of 3.8 s^{-1} at 3.0 T. Deviation from the respective reference in %.

Figure 4.33 displays rOEF maps, calculated using nCBV maps, which were derived from the first and second bolus, both without and with (method I) leakage correction. The pre-bolus and the post-processing leakage correction reduced artifacts seen in the tumorous region of $rOEF_{unc\,1}$, calculated with uncorrected CBVs obtained from the first bolus. In the CET of patient A (red arrow), rOEF demonstrated a more conspicuous rim (less intense) and brighter interior areas after leakage correction. For $rOEF_{unc\,1}$ of the second bolus (with PB), this rim was less pronounced. Inside the tumor, rOEF appeared more heterogeneous after correction. For patient B, an rOEF hotspot appeared after leakage correction (red arrow).

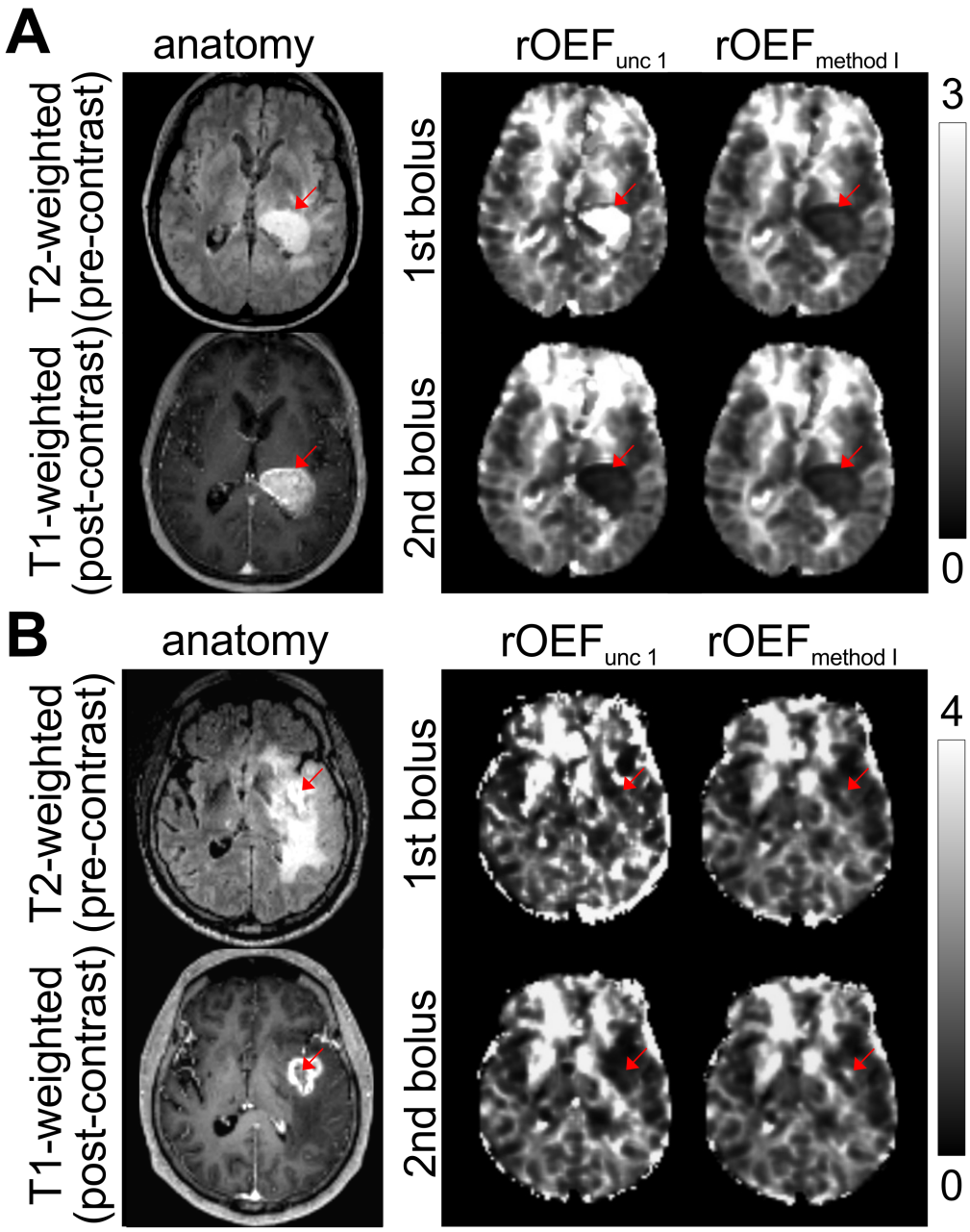

Figure 4.33: Influence of rCBV variation on rOEF parameter maps for one image slice of two patient examples. The left column shows anatomical images for each patient (A and B): a T2-weighted FLAIR (top) and a contrast enhanced T1-weighted MPRAGE (bottom). For the corresponding slice, rOEF was calculated with four different normalized CBV parameter maps: $nCBV_{unc\ 1}$ and $nCBV_{method\ I}$ each for the first and second bolus acquisition. Red arrows indicate differences due to leakage correction: the more visible, dark-rimmed CET structure for patient A and a newly appearing rOEF hotspot in patient B.

5 Discussion

Standard analysis programs for DSC-based CBV calculations assume an intact blood brain barrier without extravasation of contrast agent (CA) [59]. Within this work, the impact of CA extravasation and its correction in DSC-based CBV measurement was investigated using simulations and analyses of patient data. In the literature, several correction methods were proposed with different advantages and drawbacks [59, 102, 113]. Four correction methods [12, 16, 17, 114] were tested and optimized on data with different contrast agents and acquisition schemes in order to find the most robust and reliable technique for calculation of CBV parameter maps. In general, the results obtained using those methods differed greatly. In comparison to literature values, the majority of achieved absolute CBV values of patient data were clearly too high (section 5.4.1). However, after normalization to healthy white matter, assuming CBV_{WM} to be 1.5 % [60, 61], the values were physiologically appropriate and more consistent among methods. Throughout all investigations, method I demonstrated the best reproducibility, which is, for instance, important to assess tumor response to treatments [115].

5.1 CBV in Simulations

In a simulation study, several factors known to influence CBV quantitation [58, 67] were separately investigated with regard to the different leakage correction methods. The simulations primarily focused on the comparison of the post-processing methods and their individual dependencies on noise, temporal alterations of reference curves and IDAIFs, and the strength of CA extravasation. A perfect reproduction of input CBVs was not expected, as results depend too much on simulated tissue models.

5.1.1 Validity of Method Modifications

Arrival time correction: Methods using SVD for CBV quantification are sensitive to timing alterations of the IDAIF [66, 87, 89]. To reduce negative effects due to dispersions and delays of the IDAIF, an arrival time correction (ATC) was established. The impact of the introduced ATC was investigated on basis of standard CBV calculations using sSVD and TiSVD (variants of method III [13]). A shift of the IDAIF, either with respect to BAT or to TTP, similarly corrected delays for simulated signals without extravasation. Because the TTP can be determined more easily and robustly in noisy patient data, the TTP-based method (ATC_{TTP}) was preferred. In simulated data with extravasation, the ATC_{TTP} was shown to work also with leakage correction, but again only for delay. Delay correction techniques have primarily been investigated with regard to their influence on

CBF and MTT [89, 116-118], since in theory the CBV is independent of the shape of the curve. However, the simulations performed in this work clearly demonstrated a dependence of the calculated CBV values on IDAIF variations. This dependency was introduced by the influence of IDAIF delays and dispersions on the residual oscillations of the residue function $R(t)$. In combination with truncation, temporal differences can introduce errors in $R(t)$ [68, 116]. In dependence of the acquired and integrated time interval, this can alter the area under this curve leading to either over- or underestimation of CBVs. In contrast, Mouannes-Srour et al. [88] and Calamante et al. [87] did not find delay-dependent alterations of CBV, however, both calculated CBVs from the area under the concentration time curves (CTCs) (Eq. (3.4)), not from the residue function. Similar to most other studies [87, 116, 117], neither of the presented ATC variants could correct for IDAIF dispersions. Only Mouannes-Srour et al. [88] developed a method that aims to simultaneously correct for shifts and dispersions. However, the need for an elaborate voxel-wise fitting requires long calculation times, even though they restricted the range of values.

A stable estimate of the peak position and width is fundamental for all approaches. In the presence of perfusion abnormalities this is even more difficult and can introduce additional noise [90]. Therefore, the potential benefit of ATC and its influence on CBV were carefully investigated in patient data, as discussed in section 5.5.

Threshold between perfusion and extravasation phase: Leakage correction methods based on SVD (variants of method III) [13] require the determination of a threshold between perfusion and extravasation phase of the residue function. The extravasation phase is averaged to calculate the permeability related parameter K_2. Up to now, the influence of the threshold on CBV calculations has not been discussed in the literature. Bjørnerud et al. [13], who proposed the method, just used the T_c estimated from the Lorentzian fit of $R(t)$ generated with TiSVD as threshold. In a study by Skinner et al. [22] the threshold was set to 1.5 times the MTT achieved by circular deconvolution. However, the actual study demonstrates the importance of the threshold for CBV estimation and its dependence on the regularization method. The simulation results of this work indicate that the calculated $CBV_{\text{method III}}$ matched best with input CBV when defining the beginning of the extravasation phase at eight times T_c (Figure 4.1). Since the variance increased with later thresholds, due to less averaging a tradeoff between accuracy and variance had to be found. Consequently, for CBV calculations in patient data a minimum of at least ten time points was used to average the extravasation dominated $R(t)$. With Tikhonov regularization T_c was estimated about twice as long as with standard regularization. According to the central volume principle (Eq. (2.6)), the reason is an underestimation of CBF due to an over-regularization [119]. Thus, the threshold is already rather late and the impact of postponing the threshold on CBV was small. Probably, those underestimations would diminish if the Tikhonov regularization was

applied without an additional noise cut-off, instead, late images of the residue function might be excluded to avoid artifacts at the end of the curve (section 3.2.2). However, for leakage correction those late dynamics are most important and to exclude them in general would not be advisable. With earlier thresholds, the underestimation of simulated CBVs was more significant. This was independent of the leakage effect and could be explained by the violation of one major assumption of the correction approach of method III: a leakage dominated second phase [114]. This is only true for $t \gg T_c$ and is not satisfied for earlier thresholds, e.g. $t = T_c$. Thus, the systematic underestimation of (n)CBV for both leakage effects either results from underestimated T1 effects, overestimated T2/T2* effects or both. A major problem of later thresholds are the strong oscillations of the residue function that are still present using standard truncation. Depending on the included lobes, oscillations cannot only bias the extent of the detected leakage effects, but can also introduce a wrong sign and thus mix up T1 and T2/T2* effects. With the Tikhonov SVD or a block-circulant SVD with iterative modification of the residue function using an oscillation index (oSVD) [89], this problem could be reduced. However, those regularization techniques need longer computation times and Bjørnerud et al. [119] found no improvement in CBVs obtained with oSVD compared to those obtained with sSVD. Another possible solution would be prolonged measurement times to allow for longer averaging periods even with later thresholds.

5.1.2 Error Sources of Simulated CBVs: Interaction of Parameters

In the performed simulations, the investigated factors, i.e. degree of extravasation, SNR, reference curve and IDAIF modifications, demonstrated a highly variable impact on the investigated calculation methods.

Reproducibility of input CBV: Tissue CTCs simulated without leakage resulted in an overestimation of uncorrected CBVs. This was only partly in accordance with findings of Perkiö et al. [59], who observed that integration of CTCs over the whole time range ($CBV_{unc\,1}$) overestimates the underlying input CBV, while full integration of the tissue response ($CBV_{unc\,2}$) obtained via sSVD estimated the input CBV reasonably well. In this study, $CBV_{unc\,2}$ based on sSVD generally agreed well with input CBV, but suffered from the largest variances, most probably due to the globally selected cut-off value. As suggested by Knutsson et al. [67], this cut-off was selected SNR dependently using a global median SNR value and the classification of 0.1 for SNRs > 70 and 0.2 for SNRs < 70. A voxel-wise adaptation as proposed by Liu et al. [120] would probably reduce the variance. However, even the trapezoidal integration, the discrete sampling rate and the limited acquisition duration had effects on CBV. In theory, the convolution integral is only valid for infinite sampling durations and a fast recovery to baseline signal (section 2.3.2) [39]. Even though a finite sampling duration has been shown to introduce

systematic underestimations of simulated CBV, whereas deviations for 120 s acquisition and integration duration were shown to be relatively small [40].

Although it turned out that the input CBV is difficult to reproduce in simulations, the smallest deviations from CBV_{in} were found for methods I, II and III (sSVD). In accordance with initial results [63], extravasation corrected CBV values were predominantly underestimated, except for method II. Separated according to detected leakage effects, T1 effects were underestimated or at least insufficiently corrected, whereas T2/T2* effects were most probably overestimated or overcorrected. This agrees with current observations that CBV values of leakage unaffected tissue, i.e. GM and WM, were somewhat underestimated if processed with leakage correction (for both T10). This general underestimation is in accordance with results of Stokes et al. [21]. Even though using dual-echo data, they found that a variant of method I as well as a simplified biophysical method yielded CBV underestimations for tumors with strong T2/T2*-based leakage effects. This supports the notion of an overestimation or overcorrection of those effects. Stokes et al. [21] recommended a correction that combines pharmacokinetic and biophysical models, but the approach is much more time consuming and difficult to implement for clinical routine.

In this study, the largest underestimations were observed for methods III (TiSVD) and IV. As already mentioned in section 5.1.1, the CBV underestimation produced by method III (TiSVD) is most likely due to the additional cut-off value. However, without the additional cut-off value we found extremely noisy maps in patients because of partly occurring artifacts at the end of the residue function. For method IV, inaccurate estimations of the individual reference curves probably led to the underestimation. In contrast, CBV_{sSVD} showed smaller deviations from the input CBV most likely because of the less restrictive regularization, but in turn exhibited the largest variances. For future analyses, systematic deviations as found for methods III (TiSVD) and IV are probably easier to handle. With a much smaller variance and comparatively low deviations from input CBV, methods I and II were somewhere in between. Most likely the simple calculation algorithm makes the results in general more stable [12].

T1- vs. T2/T2*-related leakage effects: When CBV values, obtained from simulated CTCs with counteracting leakage effects were compared, it was apparent that T1-based effects generally generated larger deviations. This could be explained by the simulation approach used to evoke T1 and T2/T2* related effects. Given that sequence parameters were kept constant for signal simulations, the initial T1 (T10) was used to modify the predominant leakage effects. Thus, the effects on signal-time curves were only indirectly included, probably resulting in more severe signal alterations for a T10 of 1200 s used to simulate T1-based leakage effects. To be able to simulate both, T1- and T2/T2*-related effects, as well as a potential T1 reduction after a pre-bolus, the employed T10s were specified rather low (500 ms, 1200 ms) compared to typical native T1 values in a healthy brain at 3.0 T (800 ms to 1100 ms in WM; 1200 ms to 1800 ms in GM) [121].

According to the simulations of the present study, these values would have led to predominant T1 effects. Only the adaptation of T10 generated different leakage effects in signal curves. Different simulation approaches would therefore be needed in order to disentangle these effects properly.

However, simulations of different transfer constants K^{trans} also differently affected the observed correction strength. Yielding leakage corrected CBVs to be highly variable across methods. In accordance with these results, Paulson and Schmainda [102] identified a variable sensitivity to different manifestations of leakage effects amongst other sources as main reason for discrepancies between different correction methods. Again, methods III (TiSVD) and IV demonstrated a relatively uniform correction for all permeability levels, whereas CBV values based on sSVD demonstrated the strongest dependence on permeability. This again indicates that leakage effects were not sufficiently corrected for; in addition, CBV values were probably influenced by oscillations. In the presented simulations, K^{trans} was increased up to 0.33 min^{-1}. Such large K^{trans} values violate the assumption of a limited reflux ($K^{trans}\, t_N/v_e \ll 1$) for methods III, possibly also leading to an underestimation of K_2 values [13]. In contrast, CBV values obtained by method II demonstrated at most a minor dependency on the extravasation level. Thus, the original intention of Leigh et al. [16], who strived to find more stable permeability parameters, could be proved. Similarly stable, with increasing transfer constants were CBV values obtained with method I in the presence of T2/T2* effects. However, in presence of T1-based effects the residual dependence was rather high, further confirming the variable sensitivity to opposing leakage effects. This observation is in line with the previously detected dependence of corrected CBVs on T10 [65]. One reason might be a stronger T1 enhancement (> 30 %) compromising the simplified treatment of Eq. (3.24) [12, 14]. Haselhorst et al. [14] addressed that problem by introducing two additional fitting parameters and three additional input parameters. However, the complexity of this approach limits its usability for clinical routine.

Influence of reference curve and IDAIF properties: In principle, problems encountered with the definition of the reference curve and the IDAIF are similar. Both introduce difficulties if they are delayed or dispersed compared to the time course of the actual tissue voxel [13, 14, 87]. Therefore, it appears reasonable to perform a timing correction for both. In theory, timing alterations should influence the results of different leakage correction methods to a varying extent [13, 14, 16, 17]. In this work, T1 effects tended to be under-, T2/T2* effects to be overestimated with an incongruent reference curve (smaller MTT). This is in good agreement with the assumption of Boxerman et al. [19], later confirmed by simulations of Bjørnerud et al. [13] stating that an elevated tumor MTT ($MTT_{reference} < MTT_{tumor}$) could cause nCBV underestimation due to incorrect estimations of K_2. However, with method II (using additional temporal scaling of the reference curves) the deviations of the calculated CBV from CBV_{in} could not be reduced compared to those of method I (without timing corrections). This indicates that

MTT differences between the reference tissue and the actual tissue are not the only reason for those variations. In fact, a general bias could have induced those variations. For instance, a bias related to CBV_{in} was seen for uncorrected CBVs. In the same way, CBVs calculated with the perfect reference curve systematically overestimated high input CBVs (8 ml/100 g) and underestimated smaller input CBVs (4 ml/100 g). Nevertheless, these results also imply that reference curves generated from healthy GM and WM constitute reasonable estimates, since larger CBV values are a reasonable assumption in gliomas [55, 122-124].

The influence of IDAIF delays and dispersions was so far only investigated for CBF quantitation and data without leakage [88, 90, 119]. The present study shows that the impact on leakage corrected CBV calculations was slightly different to the effect on data without leakage using standard CBV calculations (section 5.1.1). While the simulations without leakage and respective corrections revealed a decrease in the calculated CBV from delays of -3 s (CBV overestimation) to +3 s (CBV underestimation), CBV for leakage affected and corrected data was generally underestimated for both, early and late IDAIFs. As delays also distort the residue function and might introduce or intensify oscillations (section 5.1.1), they could also affect K_2 estimates. Probably, those K_2 alterations compensate the observed overestimation of uncorrected CBV with earlier IDAIFs (section 5.1.1).

5.1.3 Limitations of the Simulation Study

The performed simulation study had several limitations. First, the signal evolution was calculated using a specific tissue model that incorporates extravasation by means of a plug-flow model and assumes the vascular space to be a well-mixed compartment. This mirrors the limitations of the employed analysis techniques, and some methods certainly work better for the assumptions underlying these simulations. For example, method III would be expected to work best for a plug-flow model because the transition between flow and extravasation exhibits a clear threshold. Furthermore, a back-flow of contrast agent into the vascular space was neglected and a fast water exchange was assumed. This fits with the assumption of most methods, but does not necessarily reflect actual physiology. A realistic tissue geometry similar to the one used by Semmineh et al. [51] was not implemented. Thus, interactions with cell size and cell packing density were only included via the susceptibility calibration factor K_e. Although K_e is expected to vary with tissue type and is supposed to be spatially heterogeneous in tumors [62], it was kept constant for all simulations. A more realistic model would further exacerbate the problem of parameter separation, since in reality strong interactions exist between biological, physiological and physical elements. With the current implementation, problems occurred, for instance, when different reference curves were investigated. Here, the

impact of MTT differences was superimposed by the influence of CBV_{in} variations and changes of the transfer constant, which is directly linked with the blood flow.

5.1.4 Preliminary Conclusions from the Simulation Study

Mainly due to time constraints, this study could only investigate some parameters and their impact. This limits conclusions with respect to the underlying real error sources permitting educated guesses at best. However, the following conclusions can be drawn with respect to optimum processing techniques and parameters: the arrival time correction worked properly for delays, but a combined delay and dispersion correction for IDAIF and reference curves similar to that presented by [88] would probably further improve CBV results. The threshold between perfusion and extravasation phase, necessary for variants of method III, has a significant impact on CBV results and should be carefully selected. Considering all investigated parameters, method I demonstrated the best performance in terms of deviations from input CBV and variability across influencing factors. Contrary, the stability of method III (sSVD) was rather low, but could probably be improved by a voxel-based SNR dependent cut-off value [120].

5.2 Impact of Sequence Design on Signal Curves

The MR signal strongly depends on sequence parameters (section 2.4.1) [51, 62]. Results of the simulation study and comparisons between patient groups indicated no significant differences between different flip angles (70° vs. 90° at constant TR) and sequences (single shot EPI vs. PRESTO) used in patient studies analyzed within this thesis. Thus, results from all study groups could be considered comparable and were analyzed together irrespective of flip angle and sequence variant. The minimally higher CBV values obtained with PRESTO compared to ssEPI acquisitions (both without PB) are most likely due to the larger dose of CA (0.10 mmol/kg) in the first one [125]. In comparison, during ssEPI (without PB) only about 0.05 mmol/kg were injected. It is known that with increasing dose the T2/T2* effects increase [15]. Consistently, larger T2/T2* effects were observed for ssEPI with PB, where about 0.05 mmol/kg (PB) plus 0.10 mmol/kg were injected. For acquisitions using PRESTO, the variance of CBV values was slightly higher, which could be explained by the more heterogeneous patient collective that besides high-grade gliomas also included two low-grade gliomas and one metastasis. Furthermore, the short (77.6 s) image acquisition could introduce several problems as discussed in section 5.4.4.

5.3 IDAIF Selection in Patients

One of the major problems of DSC-based quantification of hemodynamic parameters is the selection of a valid arterial input function (AIF). In most studies, an image-derived AIF (IDAIF) is manually selected [42]. This study demonstrates that manual selection yields inferior quality compared to the automatic selection algorithms presented (section 4.3). Especially, if more than one observer does manual selections, perfusion analysis was less reproducible. This fits with previous results proving that manual selections are highly dependent on the training status of the observer [42, 73]. Furthermore, automatic selection algorithms were comparably fast and yielded improved shapes according to known AIF criteria like high, narrow and early peaks [42]. With regard to their robustness, both algorithms (SVD and clustering) developed in this thesis were comparable to algorithms reported in the literature showing robustness factors between 10^{-5} ms^{-2} [77] and 10^{-8} ms^{-2} or even zero (but with slow algorithms) [108]. However, the variability in performance between automatic selection algorithms [70, 71, 73, 126] is huge. A study by Yin et al. [79] compared three clustering algorithms in simulations and healthy volunteers demonstrating that the normalized cut algorithm was best. However, most studies used the much faster k-means clustering [70] that is easier to implement, but less reliable [127]. In an own primary analysis of different clustering algorithms on simulated data with noise, the AIF was found to be stable for the Gaussian mixture modeling (GMM) only. However, the GMM algorithm is sensitive to the selected starting values similar to k-means and fuzzy c-means clustering [77, 108]. In the actual implementation, the variability was reduced by an iterative processing approach and by performing a second clustering, as proposed by [70], with the more reproducible normalized cut algorithm. Nevertheless, perfectly reproducible curves could not be achieved.

In this work, the approach relying on SVD was found to be much more robust. If applied to the same dataset, it always detected the same IDAIF. Similar approaches were previously used to select local AIFs, for example using the factor analysis [86] and independent component analysis [71]. Local AIFs should create hemodynamic parameters that are more robust because physiological delay and dispersion to tissue are reduced [71, 86]. Extending the SVD approach to select more local, slice specific AIFs could potentially improve the results, but computation time would approximately quintuple compared to that of the actual implementation, where five out of 25 slices were analyzed. For tumor patients, the increasing processing time would be feasible, however, if used for stroke patients the benefit should be brought in balance since partial volume effects (PVE) will increase in smaller downstream vessels [73]. The method used in this study attempts to remove voxels affected by PVE. Subsequently, local IDAIFs should be selected from a smaller number of preselected voxels. Moreover, resulting from the vascular anatomy of the brain, perfusion delays do not resemble the slice acquisition

order but rather occur in terminal areas of the vascular territories as demonstrated by arterial spin labeling [128] as well as CA-based studies of TTP [129].
Most automatic selection algorithms investigated healthy volunteers [70, 79] or patients with systemic diseases [71, 73]. In tumor patients, the selection of valid IDAIFs is aggravated by the fact that they are often found in the tumor region because of its high blood flow [130]. Accordingly, a good automatic segmentation and exclusion of tumorous tissue is fundamental. In this work, SPM12 with default parameters was used for segmentation of healthy tissue, while histogram-based thresholding for diseased tissue and vessels (section 3.7.2) allowed to reliably exclude diseased tissue. Nevertheless, errors can be introduced either by faulty segmentation or by possible misregistration between the DSC data and the segmented anatomical images. This could additionally disturb the IDAIF selection process in terms of preselected AIF voxels that relied on segmentation results of anatomical images. This error would be reduced by an analysis solely based on DSC data, as demonstrated by Bjørnerud et al. [119]. Such an analysis, however, is limited by the inferior tissue to tumor contrast of DSC time course images compared to T1-weighted post-contrast images.

5.4 CBV in Patient Studies

In this work, DSC-based CBV values were determined in the presence of CA extravasation using different post-processing techniques. Compared to the literature, absolute CBV values obtained from patient data (section 4.4) were rather high in both healthy and extravasation affected tissue [131]. The only exception from this rule was method IV, where values similar to those achieved with DCE experiments and literature values could be obtained. In accordance with [113], it was demonstrated that DSC-based CBV values strongly depend on the post-processing of the data. Besides typical variations between image processing procedures (timing correction, integration interval, AIF selection), the kind of extravasation correction method introduced additional differences in the final CBV maps. The normalization to healthy white matter yielded nCBVs well in the range of generally accepted values [131] and made results more robust against certain quantitation problems (AIF selection, signal to concentration conversion and integration interval). However, even after normalization considerable differences remained, although CBV values were much more comparable between the individual methods. Data from the two double bolus studies (two dosages, two contrast agents) allowed to derive indications with respect to reproducibility, according to which normalized CBV values obtained by method I were the most robust. This is also in accordance with the presented simulations, where method I showed smallest variances and less pronounced dependencies (section 5.1.2).

5.4.1 CBV Values in the Context of Literature

Healthy tissue: All calculated CBV values are high compared to generally accepted values of about 1.0–4.0 % in WM and 2.5–8.0 % in GM [60, 131-134]. Nevertheless, they are in the order of reported literature values for DSC-based healthy tissue CBVs that range between 1.25 ml/100 g (averaged from WM and GM of [135]) and 20.0 ± 3.8 ml/100 g (whole brain average [136]). These high CBV values are most likely caused by IDAIF imperfections like scaling problems due to residual PVE [42, 57, 74, 75, 137, 138] or a non-linear relaxivity behavior (section 2.5.1) [136]. Partial volume effects of IDAIFs are expected to result in smaller peaks and thus in an underestimation of the AIF area, finally resulting in an overestimation of calculated absolute CBV values. Even though PVE should be minimized with the initial masking (section 3.3.2) [73], segmentation and registration errors as well as susceptibility-based signal distortions can confound the masking (section 5.4.4). Analogous, a non-linear relation between IDAIF signal and concentration might hamper correct scaling (section 5.4.3). This furthermore violates one basic prerequisite of the tracer dilution theory: a linear dependence of the tissue signal on the input function [34]. Comparably high CBV values were reported by Alger et al. [139] and Wirestam et al. [136]. In [139], the CBV was reduced using a scaling constant measured in combined experiments with xenon-enhanced computed tomography. In [136], Wirestam et al. scaled the IDAIF with a venous output function to reduce PVE, as similarly proposed by Knutsson et al. [138], achieving a decrease in CBV and CBF by about 62 %. However, the venous output function is even more prone to signal distortion effects [138]. A further reason for high CBV values could be artifacts due to macroscopic vessels. Teng et al. [131] showed that CBV was significantly reduced after removing signals from CSF and vessels by means of thresholding [131, 140]. This effect could be expected to be even stronger in tumorous tissue because of its higher vascularization [130]. Imperfect IDAIFs and large vessel contributions could also explain the observed discrepancy to simulations (section 5.1.2), where methods IV and III (TiSVD) were found to largely underestimate CBV, while CBV values obtained by method III (sSVD) closely resembled input CBVs. In this scenario, it would be conceivable to presume that the underestimations observed in simulations are compensated by the IDAIF errors in patient data analysis.

Diseased tissue: Consistent with results in healthy tissue, measured absolute CBV values in tumors were relatively high in comparison to sparse literature values [13, 134, 141, 142]. Again, $CBV_{\text{method IV}}$ had the smallest values and could reproduce previously reported CBV values of [13] and [141]. Surprisingly, absolute CBV values of methods I to III were even higher than values observed with DCE and vascular-space-occupancy, which were reported to most probably overestimate CBV in the case of CA extravasation [10, 143]. The general problems of CBV quantitation are the same as in healthy tissue. In addition, an insufficient leakage correction could foster CBV overestimation in the presence of

predominant T2/T2* effects. This was observed by Stokes et al. [21] and in own simulations for large values of CBV and K^{trans}. The predominance of T2/T2*-related leakage effects in patient data taken from the hypoxia study mainly originates from the pre-dose [15, 64] and the employed magnetic field strength of 3.0 T [63]. Possible errors in leakage correction algorithms are confirmed by the partly observed increase of CBV due to extravasation correction, though values were already rather high [13, 141, 142]. Specifically, this confirms the assumption that deficient pre-processing fosters a wrong interpretation of the data. A completely different behavior, namely an exclusive reduction of the corrected VOI averaged CBV values, was observed with methods III (TiSVD) and IV. Even though CBV values obtained with method IV were much smaller than all other values, the leakage correction was insufficient. This could be inferred from the large discrepancy between CBV values obtained from the first and second CA dose (section 4.5.1). Further, parameter maps of $CBV_{\text{method IV}}$ appeared much noisier than most other maps. Here, first pass integration improved the results as discussed in section 5.4.5. With method III (TiSVD), a moderate reduction could be achieved, but CBV was still rather high. The higher CBV with sSVD is in accordance with simulations and can be explained by a less strict regularization (section 5.1.1). Similar to $CBV_{\text{method III, sSVD}}$, values of $CBV_{\text{method I}}$ and $CBV_{\text{method II}}$ were extremely high (about 36 ml/100 g and 42 ml/100 g) in comparison to previously reported values in high-grade glioma (3.9 ± 1.7 ml/100 g [13], average maximum values: 14.5 ml/100 g [142], recurrent glioblastoma 21.7 ± 13.6 ml/100 g [134]). Considering that the major leakage effect in patients acquired with pre-dose was due to T2/T2* effects [63] and the MTT was slightly longer in tumor compared to healthy reference tissue, those results agree with simulation outcomes (section 5.1.2), according to which $CBV_{\text{method I}}$ and $CBV_{\text{method II}}$ were overestimated under those conditions. High $CBV_{\text{method II}}$ values might even be fostered by a second effect: in simulations of T1 effects, the CBV was observed to be overestimated even for a perfect reference curve (section 4.1.6). The fact that absolute $CBV_{\text{method III, TiSVD}}$ and $CBV_{\text{method IV}}$ matched best with the literature, is most likely due to a general tendency of these methods to underestimate CBV (as detected by simulations), which is compensated by the IDAIF problems (PVE, non-linearity).

The weak correction effects detected with methods III compared to all other methods may be explained by the correction factor k_H (0.705 $cm^3\ g^{-1}$) that was, in contrast to the original implementation [13], also included in the extravasation part of Eq. (3.12). The parameter k_H considers that the CA distributes only over the blood plasma whose volume percentage is different in small and large vessels. In EES, a similar effect should be present. However, its impact is most likely dependent on the tissue type and changed in pathologies. In any case, it would lead to a reduction of the extravasation part, which at least partially compensates the desired increase due to the optimization of T_c [63]. Due to its impact on CBV, the distribution of the CA after extravasation should be considered in future studies. From [112] it is known that the hematocrit is different between

individual subjects and smaller in women than men. However, it is not known whether k_H is similarly influenced [58] and the exact value of k_H should be further investigated if absolute CBV is desired.

Normalized CBV: Since results differ greatly even without extravasation, as discussed above, most studies examine only relative values, normalized to a defined region or value [12, 60, 101, 123, 124, 131, 139, 144, 145]. The normalization process itself thereby introduces several uncertainties [115, 146, 147]. Therefore, an automatic algorithm for user independent normalization was developed within this work. The automatic segmentation of WM, excluding pathological tissue, allowed to achieve stable CBV values of 2.7 ± 0.1 % in GM and of 1.7 ± 0.1 % in WM averaged over all methods and patients. This perfectly agrees with normalized CBVs from Vasovist data (WM: 1.9 ± 0.5 %, GM: 2.8 ± 0.7 %) and $nCBV_{DCE}$ values (WM: 1.6 ± 0.01 %, GM: 2.7 ± 0.3 %). The literature reports a slightly stronger contrast between WM and GM with GM-to-WM ratios of 1.8 to 2.5 [119, 131]. One possible reason could be a difference in the segmentation of GM and WM. A more restrictive probability value than the used 75 % would probably increase the observed difference between GM and WM.

In VOI_{CET}, the nCBV values of all calculation methods were between 4.4 ± 1.4 % and 6.7 ± 7.4 % (35 high-grade gliomas, 1 low-grade glioma). This is in good agreement with normalized values from Boxerman et al. [12], where nCBV was about 4.0 % for grade IV gliomas (CBV-based VOI definition), and values from Law et al. [122] (6.1 ± 2.2 % for grade III gliomas) and Server et al. [148] (7.0 ± 1.7 % for glioblastoma). The leakage correction significantly changed nCBV values compared to corresponding uncorrected nCBVs. For most methods, the direction of the correction was opposed to that of the absolute CBVs because healthy WM, which served as normalization reference, was also noticeably affected by the leakage correction. One explanation for this observation is an actually existing small extravasation in healthy tissue [10, 149], another an inaccurate estimation of leakage effects (section 5.1.2). Even though leakage effects were generally estimated differently (section 4.8), all correction methods were tightly correlated with each other, except for single outliers (the only grade II tumor with CET, one patient with analysis errors introduced by the arrival time correction and sSVD, respectively), indicating their usefulness to estimate nCBV values in extravasation affected tissue. Nevertheless, possible analysis errors in automatic procedures acknowledge the need to carefully control interim results [39].

5.4.2 Attempt to Validate the DSC-based CBV

In the actual study, absolute CBV values were shown to be highly variable between methods and strongly dependent on IDAIF alterations (section 4.1.6). To evaluate the reproducibility of CBV values, acquisitions with and without pre-bolus (section 4.5.1) as well as with two different contrast agents; a protein binding CA (Vasovist) was tested

against the standard agent Gd-DTPA (section 4.7), demonstrating improved accordance after correction. Furthermore, CBV_{DSC} values and their influences were validated with independently measured PET- and DCE-based CBVs (section 4.6). Again, leakage correction improved the consistency between the three modalities, but in accordance with [133, 139] absolute CBV_{DSC} values were still larger than CBV_{PET} and CBV_{DCE}. Overall, the stability of CBV estimation can be improved by normalization of CBVs [55]. In contrast to absolute CBV values obtained in this study, normalized CBVs demonstrated higher within patient correlations between different CA boli (sections 4.5.1 and 4.7) as well as between $nCBV_{DSC}$ and CBV_{DCE} and $nCBV_{PET}$ (section 4.6), respectively.

Comparison of two consecutive boli: The use of a PB combined with post-processing was previously shown [19, 102] to improve CBV estimation in presence of CA extravasation. Therefore, the interaction of a PB with the modified post-processing methods was investigated with respect to CBV reproducibility. CBV values obtained from the second bolus were for all tissue types larger than the ones obtained from the first bolus. Although extravasation should be negligible [6], minor contrast agent extravasation has been previously reported for normal brain tissue [10, 149]. Therefore, and because image quality appeared to be improved after leakage correction and to reduce artifacts in general (section 4.8), in this study leakage correction was done for the complete brain. However, leakage correction did not definitely improve the correspondence between both boli indicating a combination of several problems. Firstly, leakage was not perfectly corrected leading to dissimilar under- or overestimations depending on whether T1- or T2/T2*-related leakage effects prevailed (see simulations section 5.1.2). Secondly, the discrepancy might also be caused by the difference in CA dose. The dose dependence of DSC studies has been discussed previously with different outcomes [58]. The majority of studies investigating two consecutive contrast agent doses found smaller CBV values for the first bolus [135, 136, 150] in healthy tissue. Nael et al. [135] explained this with the semiquantitative nature of DSC itself. Wirestam et al. [136] and Manke et al. [150] reasoned the fact with a different signal to concentration behavior for both CA doses that could be explained by a quadratic relationship (section 5.4.3). Contrary to that, Alger et al. [139] observed about 20 % lower CBV values with a doubled CA dose, which the authors explained by complex dispersion effects between the injection site and the location of the selected AIF voxels.

In tissue with obvious CA extravasation (CET), the CBV calculated from the first injection was again smaller than the one from the second injection. This is in accordance with the well-accepted theory that T1-based leakage effects are minimized after an initial pre-dose [19], which was for the investigated patients also confirmed by the distribution of K_2 values (section 4.8). Even though the T2/T2* effects are known to be increased at 3.0 T [151], scanning parameters like large flip angles and short TRs can enhance T1 effects. After leakage correction, first and second bolus CBV values converged, where for

all investigated techniques CBV_{2nd} was still higher. This is supported by findings from the simulations, in which the correction reduces, but not completely eliminates the errors. During the first bolus, the leaky tumor tissue predominantly shows T1-related leakage effects. According to the simulations, those effects are underestimated, leading to an insufficient increase of CBV. During the second bolus, more T2/T2*-related leakage effects are present. Thus, CBV would be larger. Since the degree of extravasation plays an important role for the correction (section 5.1.2), several discrepancies remained between CBVs obtained from both boli, which were furthermore based on two separate acquisitions including individual IDAIFs. Besides the different curves per se, the relationship between CA concentration and signal could also vary because of the different contrast agent doses. This could be true not only in blood, but also in tissue [150]. For small CA doses the relationship is most likely linear, while for the second doubled dose a non-linear behavior could exist (section 2.5.1). Accordingly, Gahramanov et al. [152] reported a general dose dependence of CBV if a PB was used. Compared to acquisitions with intravascular superparamagnetic iron oxide particles, Gd-DTPA was found to lead to a dose dependent overestimation with PB and an underestimation without PB [152]. The dose dependent bias probably occurs because the pre-load quickly saturates the EES with CA. Subsequently, the assumption that the molecules of the agent can freely distribute is no longer satisfied.

With normalization, a number of these problems could be bypassed and the differences between both injections were largely decreased. Nevertheless, some differences remained. Overall, the best accordance between first and second bolus was achieved with $nCBV_{method\ I}$.

Comparison of contrast agents: Because of its binding to human serum albumin [47], Vasovist is supposed to better fulfill the model assumption for CBV calculation, e.g. no back diffusion and long circulation half-live. However, the presented results (section 4.7) do not verify a clear advantage of Vasovist compared to Gd-DTPA, but rather again confirm the general problems in image analysis. The absolute CBV values obtained with Vasovist (CBV_{Vaso}) were on average about 12 % smaller than $CBV_{Gd\text{-}DTPA}$ in the same patients, irrespective of tissue type. Consequently, absolute values of CBV_{Vaso} were still too high compared to literature. Only method IV exhibited physiologically reasonable CBV values. Furthermore, method IV showed a high correlation between contrast agents, especially when using first pass integration. The reasons for CBV overestimations are similar for Vasovist and Gd-DTPA data (section 5.4.1), and a real advantage of Vasovist due to its higher relaxivity could not convincingly be demonstrated. Because of the higher T2 relaxivity (r_2) smaller doses (0.03 mmol/kg versus 0.10 mmol/kg) of CA were used. Accordingly, significantly smaller signal drops were observed for Vasovist data, which caused CBV maps to appear much noisier, especially for SVD-based approaches (Figure 4.27). This indicates that the dose was rather too low. In addition, the image acquisition protocol was suboptimal and with insufficient temporal coverage (section

3.7.1) [39]. With leakage correction, the quality of the parameter maps improved visually. Unfortunately, the T1 relaxivity (r_1) of Vasovist is also much larger (about 2.5 times) [153] resulting in a stronger T1 enhancement and thus stronger T1-related leakage effects. Although values of method I showed the best accordance between both CAs, the assumption of less than 30 % T1 enhancement [12] is probably violated. Nevertheless, in tumorous tissue the parameters PH and PSR relative to healthy tissue (rPH, rPSR) were similar for both contrast agents, indicating a similar leakage effects. However, depending on the time of injection, the short acquisition time of 77.6 s compromised reliable calculations of the baseline MR signal or the extravasation phase of the curve [39, 154]. To sum up, an increased number of baseline and post-bolus images and/or a higher CA dose would be advisable to increase SNR [155] and improve leakage correction [39, 154]. Even though both studies were performed on different days, a potential interaction between both CA boli cannot be excluded, especially if the long circulating Vasovist was injected first. In a lung perfusion study, a waiting period of at least five days was adhered after injection of Vasovist before another agent was administered [156].

After normalization, correlations between CBV values obtained with both contrast agents only increased for methods I and IV. Using methods II and III the correlation unexpectedly worsened, probably due to the poor quality of uncorrected maps that resulted in unreliable healthy white matter values.

Overall, the prospect of improved CBV measurements with Vasovist in the case of a disrupted BBB could not be confirmed and numerous disadvantages balanced potential advantages. The major problem with Vasovist is probably related to the even more complex relaxation behavior in blood, with a parabolic relationship of signal and concentration [47] (section 5.2.4). Considering possibly detrimental depositions of gadolinium-based CAs [157], which might be more severe for agents with slower systemic excretion, future studies should not use Vasovist, especially since neither CA dose reductions nor improved CBV quantitation appear feasible.

Comparison with DCE and PET: DCE-MRI is a reliable alternative to estimate absolute CBV because converting the T1-weighted MR signal to CA concentration is more straightforward than in DSC-MRI [158], and the acquisition techniques are less associated with signal distortions [143]. DCE-based CBV calculations are known to achieve quantitative measures of CBV also in the case of extravasation [143, 158]. A comparison with DCE-based absolute CBVs averaged in VOIs of healthy WM (3.8 ± 2.2 ml/100 g) and GM (6.5 ± 3.5 ml/100 g) confirms that methods III (TiSVD) and IV yield the most realistic absolute values. Nevertheless, own CBV_{DCE} values are rather high compared to previously reported values [91] and CBVs obtained with the gold standard [^{11}C]-CO PET (WM: 1.3 ± 1.2 ml/100 g, GM: 3.7 ± 0.4 ml/100 g) [133]. In our study, a comparison with [^{18}F]FET-PET in healthy tissue was not reasonable, because in that case the accumulation of the tracer was too low, which restricted the reliability of dynamic modeling.

In VOI_{TUMOR}, i.e. tumor tissue with high [^{18}F]FET uptake, CBV_{DSC} was generally higher than both, CBV_{DCE} and CBV_{PET}. This is in accordance with previous comparisons [131, 133]. One reason might be the higher spatial resolution in DSC-MRI compared to PET and DCE-MRI. Due to the limited spatial resolution of both modalities, larger PVE lead to a stronger averaging of CBV values in heterogeneous tumorous tissue (e.g. gliomas [1, 159]) and thus decreasing maximum CBV. After Gaussian smoothing, CBV_{DSC} parameter maps looked more similar and averaged CBV_{TUMOR} values were reduced. Discrepancies between the three imaging techniques might also be explained by alignment errors introduced by automatic image registration (section 5.4.4), though this was visually inspected for each patient. Further, vessels are handled differently between methodologies and can thus influence VOI averaged values. While in PET vessels were outmasked, they exhibited very high values in CBV_{DCE} and moderate values in CBV_{DSC}. Nevertheless, DCE-based CBV_{TUMOR} values calculated in this study were shown to be the smallest with a low contrast to CBV_{GM}. Even though absolute values should be more reliable with T1-based perfusion imaging (DCE-MRI) [91, 143, 160, 161], the larger volume coverage, the higher spatial and temporal resolution and the better contrast between tumor and GM in DSC-based CBV maps confirmed in this study is beneficial for clinical assessment. Recently some groups investigated combined methods (DCE and DSC) for a simultaneous determination of high-resolution parameter maps of absolute CBV, CBF, MTT and permeability, aiming at an improved assessment of tumor biology [158, 162, 163].

Although some absolute CBV_{DSC} values were in accordance with CBV_{PET} or CBV_{DCE}, only after normalization of all CBVs, significant correlations were observed between the three modalities. This again indicates that the high absolute CBV_{DSC} values suffer from individual scaling errors (section 5.4.3) [136].

Limitation: The major limitation of these comparison studies is the lack of a true gold standard to which the current DSC-based CBV values could be reliably compared. Although PET could principally provide absolute CBV values, FET is not a known perfusion marker, so that in the current work the strongest limitation of the comparison to PET-derived CBV is due to the tracer. Furthermore, although DSC, DCE and PET were performed within a single imaging session without a repositioning of the patient, resolution and contrast differences, as well as distortions in DSC data made automatic co-registration challenging, potentially causing substantial errors. The retrospective study design with different acquisition times and sequence parameters additionally introduced variances (section 5.2), and the number of patients in the dual contrast agent perfusion group (eleven) and the group with two consecutive boli (eight) was rather low. The acquisition of more patients with two CA boli is therefore currently under way. Nevertheless, the combined consideration of all these comparison studies allows to infer some indications about the most suitable and reproducible method.

5.4.3 From Signal to Concentration

Independent of contrast agent extravasation, one of the largest problems in DSC-based CBV quantitation, is the unknown relationship between MR signal and CA concentration. The relationship depends on the CA concentration. Thus, it changes during the bolus passage and is further different between blood (higher CA concentration) and tissue (smaller CA concentration). To investigate whether the non-linear relation described by [49] would be more appropriate for converting IDAIF signal to concentration, the accordance between CBVs obtained from the first (3.75 mmol) and the second (7.50 mmol) bolus was used as an indicator for accurate CBV estimation and thus accurate conversion of the signal.

According to the presented results, CBV values obtained from the first and second bolus data (two CA doses) matched best with the linear assumption, while a quadratic relation for the IDAIF using the same tissue relaxivity resulted in a reduction of CBV_{1st} (smaller CA dose) and an increase in CBV_{2nd} (larger CA dose), which increased the difference between both values. At a first glance, this suspects that IDIAF signals selected outside vessels to have a linear signal to concentration behavior, as proposed by [73]. However, in contrast to this, the measured absolute CBV values obtained from both boli were much larger than expected across all tissue types (section 5.4.1) indicating some kind of scaling problems [42]. For Gd-DTPA and the commonly applied linear relationship, different relaxivities can be found in the literature (r_2 = 0.0052 ms^{-1} mM^{-1} [153], r_2 = 0.0053 ms^{-1} mM^{-1} [48], r_2 = 0.0048 ms^{-1} mM^{-1} [99] or r_2 = 0.0870 ms^{-1} mM^{-1} [49]). Figure 5.1 shows two of them. In fact, the exact values are unimportant for CBV calculations, as long as the same linear relation can be assumed for both, tissue and arteries (IDAIF). This should be applicable if IDAIF voxels are chosen in the vicinity of arterial vessels since the same susceptibility-based contrast mechanism applies as in tissue [57]. However, if a non-linear relationship is adopted for IDAIF voxels, as would be appropriate for blood signals [49] or probably even brain parenchyma [164], the chosen value strongly influences results. Using the tissue and blood relaxivity of [49] resulted in much smaller CBVs of healthy tissue because the $\Delta R2^*$ response is stronger in tissue than in arterial blood [49, 139] (Figure 5.1). Those values are slightly too small (section 5.4.1), but demonstrate a similar scaling factor (about 0.1) as found in comparisons with xenon-enhanced computed tomography (0.1369) [139]. A non-linear relation between MR signal and CA concentration in tissue [112, 165] could probably explain the underestimation that was found in the data presented in this study, when using relaxivities as proposed by [49]. Previously, compartmentalization of CA and secondary magnetic field perturbations were suspected to induce the non-linear tissue relaxation [112, 165]. For this reason, Patil et al. [164] empirically determined a calibration curve for WM and GM based on the static dephasing regime and thus reduced the fractional error of initially overestimated CBV values. However, this is in contradiction to the

assumption that smaller CA concentrations minimize errors by non-linearity effects [158]. Additionally, as mentioned in chapter 2, the impact of the recirculation effect on CBV is only negligible in the case of a linear signal to CA concentration [40]. If a non-linearity is suspected, the impact of the recirculation depends on the contrast agent concentration during the post-bolus phase and could be different between individual voxels. Consequently, the recirculation effect modifies the CBV on a voxel basis in dependence on CA dose and integration range. Integration over a larger period would thus be more prone to recirculation related errors (section 5.4.5).

Similar problems were observed for acquisitions with Vasovist that yielded smaller CBV values than Gd-DTPA data, but were still too high compared to the literature (section 5.4.1). Here, the dependence of the MR signal on CA concentration is even more complex as it additionally depends on the protein binding [153] and thus even more on tissue structures [158]. Blockley et al. [47] found a parabolic relation for pure blood that would further increase CBV values for small concentrations (Figure 5.1). Consequently, the scaling problem is not completely caused by nonlinearities of the IDAIF relaxivity, but vessel segmentation errors and inaccurate k_H values probably also contribute to those effects [88].

Recent studies used different linear relaxivities to obtain absolute CBV values [13, 136], but only a minority [166] applied a non-linear relationship. For AUC-based methods (methods unc 1, I, II), the area of the IDAIF acts like a scaling factor between tissue and blood (Eq. (3.4)). Even though the relaxivity of both is highly variable with tissue structure and CA dose, distorting the shape of the curves, normalized CBVs based on those techniques are more robust because they are independent of the curve shapes and probably can be scaled with an empirically estimated factor to reach reasonable CBV values [139].

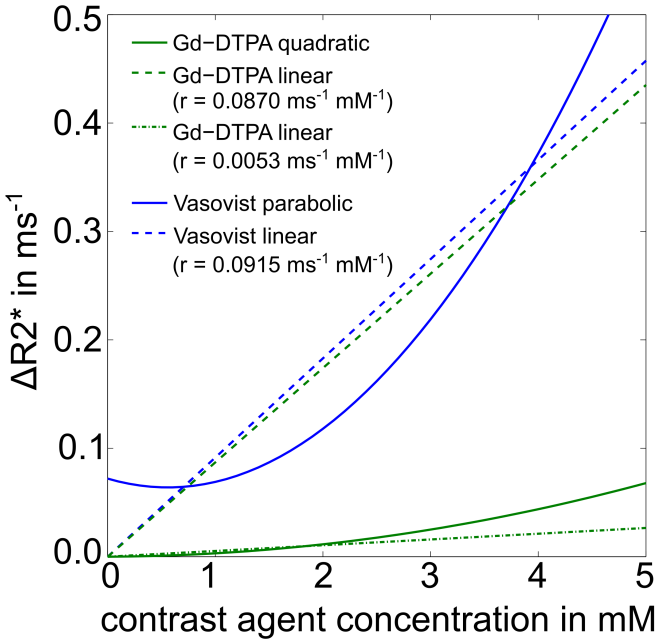

Figure 5.1: Transverse relaxation rate (Δ*R2) versus contrast agent concentration for Gd-DTPA (green) and Vasovist (blue). For Gd-DTPA two different relaxivities assuming a linear (r_2 = 0.0053 ms^{-1} mM^{-1} [48], r_2 = 0.0870 ms^{-1} mM^{-1} [49]) and one assuming a quadratic relation [49] (green), for Vasovist one linear (r_2 = 0.0915 ms^{-1} mM^{-1}) and one parabolic relationship [47] are demonstrated (blue).**

5.4.4 Problems of Image Processing

The majority of DSC data analyzed in this work were acquired with a single shot EPI (ssEPI) sequence. Because EPI is prone to image distortions that depend on susceptibility-induced magnetic field inhomogeneities, which also change during the bolus injection of paramagnetic CA, problems with voxel assignments [139] especially around major vessels could influence several steps of the CBV calculation process. First, registration errors could occur during the rigid body registration of anatomical MP-RAGE and FLAIR images to the partially distorted EPIs of the DSC time series. Since both anatomical images are the basis for segmentation and masking of the DSC series, an inaccurate registration results in assignment problems of segmented voxels. Additional distortion correction could improve spatial registration between anatomical images and distorted EPI data. However, the rather limited improvement is not worth the additional effort for $\boldsymbol{B_0}$ mapping and elaborate correction procedures [167]. In addition, the segmentation itself could be inadequate, particularly if heterogeneous tumorous tissue is contained.

A standard problem of 2D data acquisitions that influences the ssEPI DSC perfusion data itself are slice-timing effects. Although slice time correction (STC) is a standard procedure in fMRI [168], for DSC analysis STC is rather uncommon [53, 88, 169, 170]. The commonly used interleaved acquisition scheme is clearly visible in the final

maps, particularly in TTP maps (Figure 4.17). With STC, the alternating intensity schemes could be removed. For CBV calculations based on SVD, the timing is also important especially with regard to the IDAIF [89, 118]. To investigate the impact of timing corrections on CBV evaluations, averaged CBV_{WM} and CBV_{GM} values obtained from first and second bolus data were compared (section 4.5.2). Slice timing correction introduced noticeable differences in final CBV maps. However, timing correction was not consistently beneficial for CBV results in combination with the investigated leakage correction methods. This was caused by the differential impact of IDAIF timing errors on the resulting CBV values, that was most severe for methods III [87, 89]. Contrary to that, timing errors of the reference curves mainly affected method I, but the effect was comparably small as was also demonstrated in simulations. Furthermore, it needs to be emphasized that STC was done before IDAIF selection. Thus, STC increases the potential number of IDAIF locations that else would be excluded due to a later slice acquisition. Therefore, processing with STC partly leads to different IDAIFs, which may influence results when comparing CBV values without and with STC. Supported by the lower impact of STC on normalized CBV values, those IDAIF differences were probably the main reason for variations in absolute CBV. Irrespective of this potential confound, in the actual study, STC improved the calculation of TTP maps and reduced the variance of CBV values.

Originally introduced to account for different arrivals of the CA bolus at different tissues the arrival time correction (ATC) represents an alternative approach to compensate for interleaved slice timing. Here, the IDAIF is shifted in each voxel with respect to the TTP of the tissue curves prior to SVD (variants of method III). In general, the ATC method worked properly, which manifested in more homogeneous CBV maps and reduced fitting residuals of methods III. The latter improved because oscillations were reduced due to appropriate shifts of the IDAIF (section 5.1.1). If applied after STC, the influence of ATC was expected to be reduced. However, this was only partly observed because physiological differences between the globally selected IDAIF and the microvasculature of tissue also had a noticeable impact. Accordingly, a clear difference was observed between WM and GM because MTT is usually prolonged in WM, and CBV_{GM} was thus increased by ATC. Considering simulation results (section 4.1.6), this agrees with previous studies, where GM was found to have a shorter tracer delay and MTT [117, 119]. In own simulations, ATC increased CBV values calculated using IDAIFs with negative delays. The advantage of the presented ATC against STC is the additional correction of physiological transit time differences, e.g. between WM and GM. Unfortunately, a dispersion cannot be corrected and similar to simulations the variance of CBV values in final CBV maps is enhanced by ATC.

Both, STC and ATC are expected to unequivocally improve the accuracy of calculated CBV maps. However, timing errors should be corrected with care because corrections tend to introduce artifacts if data is either noisy (ATC) or affected by motion (STC). The

correction of motion directly interacts with the STC [107, 168], meaning that the voxels timing and location do no longer match if either STC or motion correction is done. Bannister et al. [168] found that the best way to circumvent this problem is a simultaneous motion and timing correction, but these methods are time-consuming and not technically mature yet. For functional MRI, Sladky et al. [107] therefore recommended to use STC first if only small motion is detectable, and otherwise the other way around.

5.4.5 Integration Interval

CBV calculation requires the integration of either concentration-time curves (CTC) or impulse response curves ($H(t)$). A consensus regarding the integration interval has not yet been reached. While Willats et al. [39] recommended first pass integration, Boxerman et al. [12] proposed to integrate trapezoidal over 120 s. Comparing these common two integration ranges, demonstrated in all tissue types larger absolute CBV values with a globally selected first pass integration compared to the full integration of the time course irrespective of underlying curves (CTC or $H(t)$). However, in healthy tissue, the integration interval had less impact on SVD-based techniques. These results are in contradiction to the simulations of Perkiö et al. [59], who demonstrated that first pass integration underestimated, while full range integration overestimated the underlying absolute CBV. This discrepancy in healthy tissue can be explained by a shorter simulated acquisition period of 60 s instead of our 120 s and the rather small input CBV values (1.8 to 4 ml/100 g). Since in the presented study the IDAIF area increased for longer acquisition times, because of the larger CA concentration during the peak and the post-bolus, the longer acquisition used in this work could result in reduced CBV values for a complete integration of the time courses. Further, depending on the location of the IDAIF voxels, the relationship between CA concentration and relaxation rate can vary between the first pass and the recirculation peak [39]. Consequently, the complete area under the IDAIF (first pass and recirculation part) could increase more than for the tissue curve reducing the CBV values calculated with full integration (section 5.4.3). Another difference is related to the definition of the first pass period, that Perkiö et al. [59] chose very tight around the peak of a globally averaged concentration time curve, strictly excluding the recirculation part. In tissue with prolonged MTT, the first pass thus may exceed the range of the globally selected integration limits, which would result in an underestimation of CBV as found for hypo-perfused tissue in patient data of Perkiö et al. [59]. In the present study, the first pass integration limits were chosen rather generously to ensure that the complete peak lay within limits, even for tissue with perfusion abnormalities, especially prolonged MTT. Still, a too narrow integration range is probably responsible for slice depending CBV alterations of the presented ssEPI data (section 4.5.2). Therefore, with first pass integration an STC is strongly recommended.

For leakage affected tissue, a larger CBV_{fp} implies predominant T1 effects because the degree of CBV over- or underestimation is directly related to the post-bolus $\Delta R2^*$ signal [102]. The presented results indicate that mainly CBV calculations without leakage correction as well as method IV benefit from the first pass integration. The improved accordance between the first and second bolus CBV values and between both contrast agents supports this assumption. In the presence of extravasation effects, the first pass integration benefits from the lower impact of extravasation on the peak signal and on the initial portion of $R(t)$ as well as from the reduced impact of recirculation effects (section 5.4.3).

Normalized CBV values demonstrated no systematic changes between integration ranges, but showed method specific fluctuations. However, in extravasation-affected tissue, the accordance between first and second bolus nCBVs mainly improved emphasizing the advantage of first pass integration against full integration. In particular, for standard, i.e. uncorrected CBV calculations ($nCBV_{unc\,1}$, $nCBV_{unc\,2}$) first pass integration acts in a similar way as a leakage correction. This contradicts to previous recommendations [12, 59] who identified the numerical integration over the whole time course to be optimal in terms of computational efficiency, SNR, and accuracy of relative values. On the other hand, Boxerman et al. [155] pointed out that larger integration ranges add considerable noise to final CBV maps. In any case, the results of the comparisons performed in this work clearly demonstrate that even a generously performed first pass integration minimizes the impact of post bolus signal problems (non-linearity, recirculation, leakage effects).

5.5 Potential of DSC to Estimate Vascular Permeability

The different DSC correction methods identified leakage effects differently, depending on the prevailing relaxation effects, extravasation strength and distribution across the tumor. Nevertheless, voxel-wise correlations between K_2 values could be observed. When comparing results obtained from the first and the second bolus, T1 effects were expectedly decreased in the latter. Between methods, the impact of the PB was different and a correlation of K_2 (first bolus) and K_2 (second bolus) values was only partly seen. This corresponds to the different effects of T2/T2*- and T1-based leakage effects on the signal (section 2.5.2). For this reason, Skinner et al. [22] concluded that identical absolute values of K_2 do not necessarily reflect the same tissue properties (vascular permeability, tissue compartments, microstructural geometry). In this work, the observed difference between K_2 values of the first and second bolus became larger with increasing deviation from zero. In fact, all investigated leakage correction approaches assume either a small extravasation or a small extravasation effect (section 3.2.2). If vascular permeability

becomes larger and the leakage effects increase, the models are no longer valid. This could explain the increasing deviations between methods for larger K_2 values and is in accordance with simulations (section 4.1.4) that demonstrated changing accuracy of CBV with changing transfer constant K^{trans}, being pronounced differently between methods. Accordingly, Bonekamp et al. [142] found a correlation between K_2 (method I) and K^{trans}, particularly for smaller values. Direct comparisons to the more commonly used permeability marker K^{trans} are difficult because neither the exact meaning of K^{trans} nor that of the individual K_2 values is really known. Even in the performed simulations, K_2 varied and did not really represent K^{trans}, although some dependence was observed. In patients, K^{trans} (as derived from DCE) and most K_2 values were in the range of reported literature values for high-grade glioma [22, 144, 171], whereby K_2 values of method III demonstrated the best accordance with measured K^{trans}. Highest correlations between K_2 and K^{trans} were found for methods I, III (sSVD) and IV, but this was not constant among patients. For patients showing high correlations, a non-linear relationship could be suspected, since Pearson correlation was smaller than Spearman correlation. This is in agreement with results of Bjørnerud et al. [13], who found a non-linear correlation of K_2 (method III) with K^{trans} in simulations. Once more, method IV showed a contrasting performance with about 10 times larger K_2 values in patient data and negative correlation of K_2 and K^{trans} in simulations. In fact, the original implementation merely investigated T1 effects using an intravascular CA [17]. Thus, for the prevailing T2/T2* effects observed in this study the method probably predicts K_2 values less reliably.

Irrespective of the inaccuracies of DSC-based K_2 values, the validity of K^{trans} as estimated with the extended Tofts model is also restricted. Based on the model assumptions, K^{trans} is only supposed to represent pure permeability if tissue is weakly vascularized (CBV small) or highly perfused (CBF large), otherwise, K^{trans} either represents CBV or CBF [161]. Because in this work the CA injection for the DCE study served as a pre-bolus for the DSC study, the DSC-based K_2 values were always affected by the pre-dose, and cannot be expected to reliably represent extravasation. Skinner et al. [22] investigated the difference between three DSC-based permeability parameters. They advised a careful use of K_2 values obtained from methods I and III as permeability parameter because they quadratically depend on the volume of the EES. Alternatively, a DSC-based K^{trans} value derived from multi-echo acquisitions could serve as a convenient measure of vascular permeability [22].

Comparing data from Vasovist and Gd-DTPA injections revealed different K_2 values across the whole brain. The K_2 values derived from Vasovist data were partially even higher than the ones of Gd-DTPA. A difference between both CAs was expected, as both have different circulation and binding behavior (Table 3.2). However, after its binding to human serum albumin Vasovist is classified as blood pool agent [103]. Considering the

unknown relation of K_2 and K^{trans}, this either demonstrates a stronger extravasation of Vasovist prior to its binding to human serum albumin and/or a stronger impact of the leakage on the signal behavior due to the higher relaxivity of Vasovist [47]. However, within this study a differentiation of both effects was not possible.
Eventually, several factors, such as its dependence on acquisition parameters and contrast agent dose prevent K_2 from being a real permeability marker, especially after a pre-dose. For leakage correction, however, it does not really matter if K_2 matches among methods. The K_2 values seem to compensate different artifacts besides extravasation, which could especially be seen for the Vasovist data. Independent of its usefulness as a permeability marker, K_2 has the potential to improve the differentiation between high- and low-grade gliomas. Even though a preliminary analysis of the data showed promising results [63], definite conclusions are not possible considering the low number of low-grade gliomas in our patient sample. Indeed the results agree with previous findings of two studies without PB that demonstrated a correlation of K_2 (method I) [7] and of K_2 (method III) with tumor grade in the presence of T2/T2* effects [13]. In contrast, Donahue et al. [172] reported a missing correlation between K_2 (method I) and tumor grade, which they explained with the administered pre-dose. However, they only evaluated T1 effects ($K_2 > 0$) that previously demonstrated less correlation with K^{trans} [13], a known predictor of tumor grade [122, 171].

5.6 Consequences for rOEF

The exemplary analysis of rOEF, using CBV parameter maps with and without leakage correction, confirms the positive impact of a PB and post-processing correction techniques for rOEF calculations. Both methods predominantly increased CBV compared to uncorrected CBV values acquired without PB. However, this is only a first step towards more quantitative values of the oxygen extraction fraction. General problems of T2 and T2* mapping are still the focus of actual research and are discussed in [60]. Nevertheless, maps appeared visually improved and could be expected to become more stable when calculated with leakage corrected CBVs. A quantitative study, comparing rOEF with the uptake of a PET tracer that is assumed to get trapped in hypoxic cells ([^{18}F]-fluoro-misonidazole) [3] and an analysis of more patients are currently underway; hopefully this will shed some light on the relationship between rOEF as a measure of blood deoxygenation and tissue hypoxia. Robust CBV maps are in any case an important prerequisite towards more reliable rOEF maps. Further studies will be needed to determine whether perfusion and oxygenation related parameters allow statements about tumor hypoxia and heterogeneity.

6 Conclusion and Future Directions

Within this graduate thesis, an automatic tool was developed to allow stable and accurate analysis of DSC-MRI data. Each processing step was separately analyzed and optimized. Several recommendations for CBV evaluations were derived with special consideration of the clinical situation. In line with a recent study by Hu et al. [113] the most important result of this work is the recognition that a standardization of post-processing methods for CBV quantification should be of highest priority.

Optimized post-processing, as proposed in this work, improves the reproducibility of CBV estimates and thus the comparability between different acquisitions of one patient, allowing for different types and doses of contrast agents as well as a range of acquisition parameters. The absolute CBV is difficult to estimate; even though the CBV values obtained with methods III (TiSVD) and IV are in the range of PET- and DCE-derived values, the results differ widely. Taking into account the simulation results, the rather favorable CBV values obtained by methods III and IV most likely emerge from a coincidental compensation of overestimations due to IDAIF errors with method specific underestimations resulting from regularization or inadequate extravasation correction.

According to the presented results, the stability of CBV estimates can be improved by normalization. However, this normalization process might by itself introduce several uncertainties [146, 147], and like all post-processing steps it should be standardized and user independent. Applying the proposed automatic segmentation procedure of healthy white matter with rigorous thresholds, normalization generates highly reproducible values. Nevertheless, a considerable variability across methods remains. SVD-based methods particulary demonstrated a high variability being sensitive to low SNR, the degree of extravasation and IDAIF timing. Normalized CBV values obtained by method I ($nCBV_{method\ I}$) are independent of IDAIF selection, which is a major factor fostering its surpassing stability.

According to the presented simulation results, ATC similar to that of Mouannes-Srour et al. [88] would probably improve the accuracy of every method, if applied to the reference curve or IDAIF. However, the benefit of an ATC needs to be weighed against two major disadvantages, namely the enhancement of noise and the prolonged processing time. If additional K_2 estimates are needed, such a timing correction would potentially improve outcomes. However, the ability of K_2 to reliably characterize vascular permeability or tumor grade remains unclear. In any case, for a more detailed analysis of DSC-based permeability acquisitions without a pre-dose seem to be more reliable. Based on the presented results, a semi-quantitative CBV analysis might be feasible by combining methods I and IV, using first pass integration and normalizing $CBV_{method\ I}$ with the

absolute WM values obtained with method IV. However, this approach requires further investigations into the stability of method IV in healthy tissue.

In addition to an improved comparability of studies, optimized post-processing might even allow the reduction of the applied contrast agent dose, minimizing the potentially detrimental accumulation of Gd-DTPA in the brain [24]. This is especially relevant with regard to the question if a pre-bolus is necessary when suitable leakage correction methods are applied. In the present study, leakage correction method I yielded similar nCBV results for data, acquired with and without a pre-dose. Thus, reducing the injected Gd-DTPA dose from a total of 0.15 mmol to 0.05 mmol seems to yield comparable results. As an alternative, data obtained from injection of a high relaxivity contrast agent (Vasovist) were investigated. However, the prospect of avoiding some post-processing steps with the more intravascular agent could not be confirmed. The lower dose of Vasovist (0.03 mmol) turned out to be sufficient to measure CBV, but resulted in rather noisy parameter maps. The appearance improved after leakage correction highlighting the need for such correction. Again, $nCBV_{method\ I}$ demonstrated the best performance and reproducibility.

In terms of more quantitative OEF values, preliminary results indicate an improvement if leakage corrected CBV is used. Theoretical estimates indicate that CBV overestimation introduces less bias to rOEF than underestimation (section 4.9). According to the findings reported in this work, corrected in contrast to uncorrected CBV values rather tend to overestimate the actual CBV. This supports the hypothesis that appropriate leakage correction techniques should improve the reliability of calculated rOEF values. Indeed, initial results demonstrated a clear improvement in the visual appearance of rOEF maps revealing additional detail after a PB and even more after post-processing correction. As a next step, these preliminary results need to be validated in a larger patient group, in combination with a gold standard reference for CBV and hypoxia.

7 List of Abbreviations

A

AIF	arterial input function
ATC	arrival time correction
AUC	area under the curve

B

BAT	bolus arrival time
BOLD	blood oxygenation level dependent

C

CA	contrast agent
CBF	cerebral blood flow
CBV	cerebral blood volume
CSF	cerebrospinal fluid
CTC	concentration-time curve

D

dCBV	deoxygenated cerebral blood volume
DCE	dynamic contrast-enhanced
DSC	dynamic susceptibility contrast
DTPA	diethylenetriaminepentaacetate

E

EES	extracellular-extravascular space
EPI	echo planar imaging

F

FA	flip angle
FET	O-(2-fluoroethyl)-L-tyrosine
FLAIR	fluid attenuated inversion recovery
FLASH	fast low angle shot
FWHM	full width at half maximum

G

GE	gradient echo
GM	gray matter, gray matter
GMM	Gaussian mixture model

H

Hct	hematocrit level

I

ICS	intracellular space
IDAIF	image-derived arterial input function

M

MP-RAGE	magnetization prepared rapid gradient echo
MRI	magnetic resonance imaging
MTT	mean transit time

O

OEF	oxygen extraction fraction
oSVD	oscillation indexed circular singular value decomposition

P

PB	pre-bolus
PET	positron emission tomography
PVE	partial volume effects

R

RBC	red blood cell
RF	radiofrequency
rOEF	relative oxygen extraction fraction
rPH	relative peak height
rPSR	relative percentage signal recovery

S

SE	spin echo
SNR	signal-to-noise ratio
ssEPI	single shot echo planar imaging
sSVD	standard singular value decomposition
STC	slice time correction
SVD	singular value decomposition

T

TBR	tumor-to-brain ratio
TE	echo time
TiSVD	Tikhonov singular value decomposition
TR	repetition time

TTP	time-to-peak

V

VOI	volume of interest

W

WM	white matter

8 List of Figures

9 List of Tables

10 Bibliography

[1] A. Omuro and L. M. DeAngelis, "Glioblastoma and other malignant gliomas: a clinical review," *JAMA,* vol. 310, pp. 1842-50, Nov 6 2013.

[2] S. Kesari, "Understanding Glioblastoma Tumor Biology: The Potential to Improve Current Diagnosis and Treatments," *Seminars in Oncology,* vol. 38, pp. S2-S10, 2011.

[3] I. Mendichovszky and A. Jackson, "Imaging hypoxia in gliomas," *Br J Radiol,* vol. 84 Spec No 2, pp. S145-58, Dec 2011.

[4] S. E. Rademakers, P. N. Span, J. H. Kaanders, F. C. Sweep, A. J. van der Kogel, and J. Bussink, "Molecular aspects of tumour hypoxia," *Mol Oncol,* vol. 2, pp. 41-53, Jun 2008.

[5] G. Bergers and D. Hanahan, "Modes of resistance to anti-angiogenic therapy," *Nature Reviews Cancer,* vol. 8, pp. 592-603, 2008.

[6] P. Ballabh, A. Braun, and M. Nedergaard, "The blood-brain barrier: an overview: structure, regulation, and clinical implications," *Neurobiology of disease,* vol. 16, pp. 1-13, Jun 2004.

[7] J. M. Provenzale, G. R. Wang, T. Brenner, J. R. Petrella, and A. G. Sorensen, "Comparison of Permeability in High-Grade and Low-Grade Brain Tumors Using Dynamic Susceptibility Contrast MR Imaging," *American Journal of Roentgenology,* vol. 178, pp. 711-716, 2002/03/01 2002.

[8] K. A. Krohn, J. M. Link, and R. P. Mason, "Molecular imaging of hypoxia," *J Nucl Med,* vol. 49 Suppl 2, pp. 129S-48S, Jun 2008.

[9] D. A. Yablonskiy and E. M. Haacke, "Theory of NMR signal behavior in magnetically inhomogeneous tissues: the static dephasing regime," *Magn Reson Med,* vol. 32, pp. 749-63, Dec 1994.

[10] N. M. Hirsch, "BOLD-based Magnetic Resonance Imaging of Hypoxia in the Human Brain," Dissertation, Fakultät für Physik, Technische Universität München, 2013.

[11] R. F. Barajas, Jr. and S. Cha, "Benefits of dynamic susceptibility-weighted contrast-enhanced perfusion MRI for glioma diagnosis and therapy," *CNS oncology,* vol. 3, pp. 407-19, Nov 2014.

[12] J. Boxerman, K. Schmainda, and R. Weisskoff, "Relative Cerebral Blood Volume Maps Corrected for Contrast Agent Extravasation Significantly Correlate with Glioma Tumor Grade, Whereas Uncorrected Maps Do Not," *AJNR Am J Neuroradiol,* vol. 27, pp. 859–67, 2006.

[13] A. Bjørnerud, A. G. Sorensen, K. Mouridsen, and K. E. Emblem, "T1- and T2*-dominant extravasation correction in DSC-MRI: Part I—theoretical considerations and implications for assessment of tumor hemodynamic properties," *Journal of Cerebral Blood Flow & Metabolism,* vol. 31, pp. 2041-2053, 2011.

[14] R. Haselhorst, L. Kappos, D. Bilecen, K. Scheffler, D. Möri, E. Radü*, et al.*, "Dynamic Susceptibility Contrast MR Imaging of Plaque Development in Multiple Sclerosis: Application of an Extended Blood-Brain Barrier Leakage Correction," *Journal of Magnetic Resonance Imaging,* vol. 11, pp. 495–505, 2000.

[15] L. S. Hu, L. C. Baxter, D. S. Pinnaduwage, T. L. Paine, J. P. Karis, B. G. Feuerstein*, et al.*, "Optimized preload leakage-correction methods to improve the diagnostic accuracy of dynamic susceptibility-weighted contrast-enhanced perfusion MR imaging in posttreatment gliomas," *AJNR Am J Neuroradiol,* vol. 31, pp. 40-8, Jan 2010.

[16] R. Leigh, S. S. Jen, D. D. Varma, A. E. Hillis, and P. B. Barker, "Arrival time correction for dynamic susceptibility contrast MR permeability imaging in stroke patients," *PLoS One,* vol. 7, p. e52656, 2012.

[17] C. C. Quarles, B. D. Ward, and K. M. Schmainda, "Improving the reliability of obtaining tumor hemodynamic parameters in the presence of contrast agent extravasation," *Magn Reson Med,* vol. 53, pp. 1307-16, Jun 2005.

[18] E. J. Vonken, M. J. van Osch, C. G. Bakker, and M. A. Viergever, "Measurement of Cerebral Perfusion With Dual-Echo Multi-Slice Quantitative Dynamic Susceptibility Contrast MRI," *J. Magn. Reson. Imaging,* vol. 10, pp. 109–117, 1999.

[19] J. L. Boxerman, D. E. Prah, E. S. Paulson, J. T. Machan, D. Bedekar, and K. M. Schmainda, "The Role of preload and leakage correction in gadolinium-

based cerebral blood volume estimation determined by comparison with MION as a criterion standard," *AJNR Am J Neuroradiol,* vol. 33, pp. 1081-7, Jun 2012.

[20] H. Schmiedeskamp, J. B. Andre, M. Straka, T. Christen, S. Nagpal, L. Recht*, et al.*, "Simultaneous perfusion and permeability measurements using combined spin- and gradient-echo MRI," *J Cereb Blood Flow Metab,* vol. 33, pp. 732-43, May 2013.

[21] A. M. Stokes, N. Semmineh, and C. C. Quarles, "Validation of a T and T2* leakage correction method based on multiecho dynamic susceptibility contrast MRI using MION as a reference standard," *Magnetic Resonance in Medicine,* Sep 12 2015.

[22] J. T. Skinner, P. L. Moots, G. D. Ayers, and C. C. Quarles, "On the Use of DSC-MRI for Measuring Vascular Permeability," *AJNR Am J Neuroradiol,* vol. 37, pp. 80-7, Jan 2016.

[23] M. S. Shiroishi, G. Castellazzi, J. L. Boxerman, F. D'Amore, M. Essig, T. B. Nguyen*, et al.*, "Principles of T2 *-weighted dynamic susceptibility contrast MRI technique in brain tumor imaging," *J Magn Reson Imaging,* vol. 41, pp. 296-313, Feb 2015.

[24] C. Lukas, R. Gold, J. Fiehler, S. Siemonsen, J. Kleine, F. Zipp*, et al.*, "Ablagerung von gadoliniumhaltigen Kontrastmitteln im Gehirn nach mehrfacher Anwendung: Konsequenzen für den Einsatz der MRT bei Diagnosestellung und Verlaufsbeurteilung der Multiplen Sklerose?," *Aktuelle Neurologie,* vol. 43, pp. 237-241, 2016.

[25] D. W. McRobbie, E. A. Moore, M. J. Graves, and M. R. Prince, "MRI From PictureTo Proton," ed, 2006.

[26] P. Mansfield and I. L. Pykett, "Biological and medical imaging by NMR," *Journal of Magnetic Resonance,* vol. 29, pp. 355-373, 1978.

[27] D. L. Bailey, D. W. Townsend, P. E. Valk, and M. N. Maisey, *Positron Emission Tomography*: Springer-Verlag London Limited, 2005.

[28] R. B. Buxton. (2009). *Introduction to Functional Magnetic Resonance Imaging (2nd ed.)*.

[29] B. Schaller, "Physiology of cerebral venous blood flow: from experimental data in animals to normal function in humans," *Brain Res Brain Res Rev,* vol. 46, pp. 243-60, Nov 2004.

[30] K. L. Leenders, D. Perani, A. A. Lammertsma, J. D. Heather, P. Buckingham, M. J. Healy*, et al.*, "Cerebral blood flow, blood volume and oxygen utilization. Normal values and effect of age," *Brain,* vol. 113 (Pt 1), pp. 27-47, Feb 1990.

[31] R. E. Latchaw, H. Yonas, G. J. Hunter, W. T. Yuh, T. Ueda, A. G. Sorensen*, et al.*, "Guidelines and recommendations for perfusion imaging in cerebral ischemia: A scientific statement for healthcare professionals by the writing group on perfusion imaging, from the Council on Cardiovascular Radiology of the American Heart Association," *Stroke,* vol. 34, pp. 1084-104, Apr 2003.

[32] M. Wintermark, M. Sesay, E. Barbier, K. Borbely, W. P. Dillon, J. D. Eastwood*, et al.*, "Comparative overview of brain perfusion imaging techniques," *Stroke,* vol. 36, pp. e83-99, Sep 2005.

[33] D. S. Williams, J. A. Detre, J. S. Leigh, and A. P. Koretsky, "Magnetic resonance imaging of perfusion using spin inversion of arterial water," *Proc Natl Acad Sci U S A,* vol. 89, pp. 212-6, Jan 01 1992.

[34] R. E. Carson, "Tracer Kinetic Modeling in PET*," in *Positron Emission Tomography*, D. L. T. Bailey, D.W.; Valk, P.E.; Maisey, M.N., Ed., ed Singapore: Springer-Verlag London, 2005.

[35] J. A. Johnson and T. A. Wilson, "A model for capillary exchange," *Am J Physiol,* vol. 210, pp. 1299-303, Jun 1966.

[36] K. S. St Lawrence and T. Y. Lee, "An adiabatic approximation to the tissue homogeneity model for water exchange in the brain: I. Theoretical derivation," *J Cereb Blood Flow Metab,* vol. 18, pp. 1365-77, Dec 1998.

[37] S. P. Sourbron and D. L. Buckley, "Tracer kinetic modelling in MRI: estimating perfusion and capillary permeability," *Phys Med Biol,* vol. 57, pp. R1-33, Jan 21 2012.

[38] E. D. Morris, J. E. Christopher, K. C. Schmidt, B. T. Christian, R. F. Muzic JR., and R. E. Fisher, "Chapter 23 - Kinetic Modeling in Positron Emission Tomography," in *Emission Tomography - The Fundamentals of PET and*

SPECT, M. N. Wernick and J. N. Aarsvold, Eds., ed San Diego: Academic Press, 2004, pp. 499-540.

[39] L. Willats and F. Calamante, "The 39 steps: evading error and deciphering the secrets for accurate dynamic susceptibility contrast MRI," *NMR in Biomedicine,* vol. 26, pp. 913-931, 2013.

[40] J. C. Kosior and R. Frayne, "Perfusion parameters derived from bolus-tracking perfusion imaging are immune to tracer recirculation," *Journal of Magnetic Resonance Imaging,* vol. 31, pp. 753-756, 2010.

[41] T. E. Yankeelov, J. J. Luci, M. Lepage, R. Li, L. Debusk, P. C. Lin*, et al.*, "Quantitative pharmacokinetic analysis of DCE-MRI data without an arterial input function: a reference region model," *Magn Reson Imaging,* vol. 23, pp. 519-29, May 2005.

[42] F. Calamante, "Arterial input function in perfusion MRI: a comprehensive review," *Prog Nucl Magn Reson Spectrosc,* vol. 74, pp. 1-32, Oct 2013.

[43] A. Haase, J. Frahm, D. Matthaei, W. Hanicke, and K. D. Merboldt, "FLASH imaging: rapid NMR imaging using low flip-angle pulses," *J Magn Reson,* vol. 67, pp. 258-266, Apr 1986.

[44] Brown R. W., Cheng Y.-C. N., Haacke E. M., Thompson M. R., and Venkatesan R., "Magnetic Properties of Tissues," in *Magnetic Resonance Imaging: Physical Principles and Sequence Design*, Second Edition ed. Chichester, UK: John Wiley & Sons Ltd, 2014.

[45] D. A. Yablonskiy, A. L. Sukstanskii, and X. He, "Blood oxygenation level-dependent (BOLD)-based techniques for the quantification of brain hemodynamic and metabolic properties - theoretical models and experimental approaches," *NMR Biomed,* vol. 26, pp. 963-86, Aug 2012.

[46] E. Debroye and T. N. Parac-Vogt. (2015, 01). ChemInform Abstract Towards Polymetallic Lanthanide Complexes as Dual Contrast Agents for Magnetic Resonance and Optical Imaging, ChemInform Volume 46, Issue 6. *ChemInform 46(6),* no. Available: http://onlinelibrary.wiley.com/doi/10.1002/chin.201506268/abstract

[47] N. P. Blockley, L. Jiang, A. G. Gardener, C. N. Ludman, S. T. Francis, and P. A. Gowland, "Field strength dependence of R1 and R2* relaxivities of

human whole blood to ProHance, Vasovist, and deoxyhemoglobin," *Magn Reson Med,* vol. 60, pp. 1313-20, Dec 2008.

[48] J. Pintaske, P. Martirosian, H. Graf, G. Erb, K. P. Lodemann, C. D. Claussen*, et al.*, "Relaxivity of Gadopentetate Dimeglumine (Magnevist), Gadobutrol (Gadovist), and Gadobenate Dimeglumine (MultiHance) in human blood plasma at 0.2, 1.5, and 3 Tesla," *Invest Radiol,* vol. 41, pp. 213-21, Mar 2006.

[49] B. F. Kjølby, L. Østergaard, and V. G. Kiselev, "Theoretical model of intravascular paramagnetic tracers effect on tissue relaxation," *Magnetic Resonance in Medicine,* vol. 56, pp. 187-197, 2006.

[50] M. M. Modo and J. W. Bulte, *Molecular and cellular MR imaging*: CRC Press, 2007.

[51] N. B. Semmineh, J. Xu, J. L. Boxerman, G. W. Delaney, P. W. Cleary, J. C. Gore*, et al.*, "An efficient computational approach to characterize DSC-MRI signals arising from three-dimensional heterogeneous tissue structures," *PLoS One,* vol. 9, p. e84764, 2014.

[52] M. Wintermark, G. W. Albers, J. P. Broderick, A. M. Demchuk, J. B. Fiebach, J. Fiehler*, et al.*, "Acute Stroke Imaging Research Roadmap II," *Stroke,* vol. 44, pp. 2628-39, Sep 2013.

[53] M. Straka, G. W. Albers, and R. Bammer, "Real-time diffusion-perfusion mismatch analysis in acute stroke," *J Magn Reson Imaging,* vol. 32, pp. 1024-37, Nov 2010.

[54] R. F. Barajas, J. S. Chang, P. K. Sneed, M. R. Segal, M. W. McDermott, and S. Cha, "Distinguishing Recurrent Intra-Axial Metastatic Tumor from Radiation Necrosis Following Gamma Knife Radiosurgery Using Dynamic Susceptibility-Weighted Contrast-Enhanced Perfusion MR Imaging," *American Journal of Neuroradiology,* vol. 30, pp. 367-372, 2008.

[55] K. Welker, J. Boxerman, A. Kalnin, T. Kaufmann, M. Shiroishi, and M. Wintermark, "ASFNR recommendations for clinical performance of MR dynamic susceptibility contrast perfusion imaging of the brain," *AJNR Am J Neuroradiol,* vol. 36, pp. E41-51, Jun 2015.

[56] J. E. Perthen, F. Calamante, D. G. Gadian, and A. Connelly. (2002, 01). Is quantification of bolus tracking MRI reliable without deconvolution?

Magnetic Resonance in Medicine Volume 47, Issue 1. *Magnetic Resonance in Medicine 47(1),* 61-67. Available: http://onlinelibrary.wiley.com/doi/10.1002/mrm.10020/abstract

[57] E. J. Bleeker, M. A. van Buchem, and M. J. van Osch, "Optimal location for arterial input function measurements near the middle cerebral artery in first-pass perfusion MRI," *J Cereb Blood Flow Metab,* vol. 29, pp. 840-52, Apr 2009.

[58] L. Knutsson, F. Ståhlberg, and R. Wirestam, "Absolute quantification of perfusion using dynamic susceptibility contrast MRI: pitfalls and possibilities," *Magn Reson Mater Phy,* vol. 23, pp. 1-21, 2010.

[59] J. Perkiö, H. J. Aronen, A. Kangasmaki, Y. Liu, J. Karonen, S. Savolainen*, et al.*, "Evaluation of four postprocessing methods for determination of cerebral blood volume and mean transit time by dynamic susceptibility contrast imaging," *Magn Reson Med,* vol. 47, pp. 973-81, May 2002.

[60] N. M. Hirsch, V. Toth, A. Forschler, H. Kooijman, C. Zimmer, and C. Preibisch, "Technical considerations on the validity of blood oxygenation level-dependent-based MR assessment of vascular deoxygenation," *NMR Biomed,* vol. 27, pp. 853-62, Jul 2014.

[61] V. Toth, A. Forschler, N. M. Hirsch, J. den Hollander, H. Kooijman, J. Gempt*, et al.*, "MR-based hypoxia measures in human glioma," *J Neurooncol,* vol. 115, pp. 197-207, Nov 2013.

[62] C. C. Quarles, D. F. Gochberg, J. C. Gore, and T. E. Yankeelov, "A theoretical framework to model DSC-MRI data acquired in the presence of contrast agent extravasation," *Phys Med Biol,* vol. 54, pp. 5749-66, Oct 7 2009.

[63] A. Kluge, M. Lukas, V. Toth, T. Pyka, C. Zimmer, and C. Preibisch, "Analysis of three leakage-correction methods for DSC-based measurement of relative cerebral blood volume with respect to heterogeneity in human gliomas," *Magn Reson Imaging,* vol. 34, pp. 410-21, May 2016.

[64] P. S. LaViolette, M. K. Daun, E. S. Paulson, and K. M. Schmainda, "Effect of contrast leakage on the detection of abnormal brain tumor vasculature in high-grade glioma," *J Neurooncol,* vol. 116, pp. 543-9, Feb 2014.

[65] R. M. Weisskoff, J. L. Boxerman, A. G. Sorensen, S. F. Kulke, T. A. Campbell, and B. R. Rosen, "Simultaneous blood volume and permeability mapping using a single Gd-based contrast injection. ," in *Proceedings of the Society of Magnetic Resonance*, San Francisco, Calif.; Berkeley, Calif: , 1994.

[66] L. Østergaard, R. Weisskoff, D. Chesler, C. Gyldensted, and B. Rosen "High Resolution Measurement of Cerebral Blood Flow using Intravascular Tracer Bolus Passages. Part I: Mathematical Approach and Statistical Analysis," *Magnetic Resonance in Medicine,* vol. 36, pp. 715-725, 1996.

[67] L. Knutsson, F. Ståhlberg, and R. Wirestam, "Aspects on the accuracy of cerebral perfusion parameters obtained by dynamic susceptibility contrast MRI: a simulation study," *Magn Reson Imaging,* vol. 22, pp. 789-798, 2004.

[68] F. Calamante, D. G. Gadian, and A. Connelly, "Quantification of bolus-tracking MRI: Improved characterization of the tissue residue function using Tikhonov regularization," *Magn Reson Med,* vol. 50, pp. 1237-47, Dec 2003.

[69] P. C. Hansen, "Regularization Tools Version 4.0 for Matlab 7.3," *Numerical Algorithms,* pp. 189-194, 2007.

[70] K. Mouridsen, S. Christensen, L. Gyldensted, and L. Østergaard, "Automatic selection of arterial input function using cluster analysis," *Magn Reson Med,* vol. 55, pp. 524-31, Mar 2006.

[71] F. Calamante, M. Mørup, and L. K. Hansen, "Defining a local arterial input function for perfusion MRI using independent component analysis," *Magnetic Resonance in Medicine,* vol. 52, pp. 789-797, 2004.

[72] E. J. W. Bleeker, A. G. Webb, M. A. A. van Walderveen, M. A. van Buchem, and M. J. P. van Osch, "Evaluation of signal formation in local arterial input function measurements of dynamic susceptibility contrast MRI," *Magnetic Resonance in Medicine,* vol. 67, pp. 1324-1331, 2012.

[73] E. J. W. Bleeker, M. J. P. van Osch, A. Connelly, M. A. van Buchem, A. G. Webb, and F. Calamante, "New criterion to aid manual and automatic selection of the arterial input function in dynamic susceptibility contrast MRI," *Magnetic Resonance in Medicine,* vol. 65, pp. 448-456, 2011.

[74] B. F. Kjølby, I. K. Mikkelsen, M. Pedersen, L. Østergaard, and V. G. Kiselev, "Analysis of partial volume effects on arterial input functions using gradient

echo: A simulation study," *Magnetic Resonance in Medicine,* vol. 61, pp. 1300-1309, 2009.

[75] M. J. P. van Osch, J. van der Grond, and C. J. G. Bakker, "Partial volume effects on arterial input functions: Shape and amplitude distortions and their correction," *Journal of Magnetic Resonance Imaging,* vol. 22, pp. 704-709, 2005.

[76] G. McLachlan and D. Peel, *Finite Mixture Models*: John Wiley & Sons, Inc., 2005.

[77] J. Yin, H. Sun, J. Yang, and Q. Guo, "Comparison of K-means and fuzzy c-means algorithm performance for automated determination of the arterial input function," *PLoS One,* vol. 9, p. e85884, 2014.

[78] J. Yin, H. Sun, J. Yang, and Q. Guo, "Automated detection of the arterial input function using normalized cut clustering to determine cerebral perfusion by dynamic susceptibility contrast-magnetic resonance imaging," *Journal of Magnetic Resonance Imaging,* vol. 41, pp. 1071-1078, 2015.

[79] J. Yin, J. Yang, and Q. Guo, "Automatic determination of the arterial input function in dynamic susceptibility contrast MRI: comparison of different reproducible clustering algorithms," *Neuroradiology,* vol. 57, pp. 535-43, May 2015.

[80] J. Shi and J. Malik, "Normalized Cuts and Image Segmentation," *IEEE Trans. Pattern Anal. Mach. Intell.,* vol. 22, pp. 888-905, 2000.

[81] T. Cour, S. Yu, and J. Shi, "Normalized Cut Segmentation Code," Tested on matlab R2009b ed: University of Pennsylvania, Computer and Information Science Department, 2004.

[82] G. Golub and W. Kahan, "Calculating the singular values and pseudo-inverse of a matrix," *J. SIAM Numer. Anal.,* vol. 2, pp. 205-224, 1965.

[83] M. E. Wall, A. Rechtsteiner, and L. M. Rocha, "Singular value decomposition and principal component analysis," in *A Practical Approach to Microarray Data Analysis*, D. P. Berrar, W. Dubitzky, and M. Granzow, Eds., ed Norwell: Kluwer, 2003, pp. 91-109.

[84] R. Sanz-Requena, J. M. Prats-Montalban, L. Marti-Bonmati, A. Alberich-Bayarri, G. Garcia-Marti, R. Perez*, et al.*, "Automatic individual arterial input

functions calculated from PCA outperform manual and population-averaged approaches for the pharmacokinetic modeling of DCE-MR images," *J Magn Reson Imaging,* vol. 42, pp. 477-87, Aug 2015.

[85] A. L. Martel, D. Fraser, G. S. Delay, P. S. Morgan, and A. R. Moody, "Separating arterial and venous components from 3D dynamic contrast-enhanced MRI studies using factor analysis," *Magn Reson Med,* vol. 49, pp. 928-33, May 2003.

[86] L. Knutsson, E.-M. Larsson, O. Thilmann, F. Ståhlberg, and R. Wirestam. (2006, 01). Calculation of cerebral perfusion parameters using regional arterial input functions identified by factor analysis. *Journal of Magnetic Resonance Imaging 23(4),* 444-453. Available: http://onlinelibrary.wiley.com/doi/10.1002/jmri.20535/abstract

[87] F. Calamante, D. G. Gadian, and A. Connelly, "Delay and Dispersion Effects in Dynamic Susceptibility Contrast MRI: Simulations Using Singular Value Decomposition," *Magnetic Resonance in Medicine,* vol. 44, pp. 466–473, 2000.

[88] J. J. Mouannes-Srour, W. Shin, S. A. Ansari, M. C. Hurley, P. Vakil, B. R. Bendok*, et al.*, "Correction for arterial-tissue delay and dispersion in absolute quantitative cerebral perfusion DSC MR imaging," *Magnetic Resonance in Medicine,* vol. 68, pp. 495-506, Aug 2012.

[89] O. Wu, L. Østergaard, R. M. Weisskoff, T. Benner, B. R. Rosen, and A. G. Sorensen, "Tracer arrival timing-insensitive technique for estimating flow in MR perfusion-weighted imaging using singular value decomposition with a block-circulant deconvolution matrix," *Magnetic Resonance in Medicine,* vol. 50, pp. 164-174, 2003.

[90] M. Ibaraki, E. Shimosegawa, H. Toyoshima, K. Takahashi, S. Miura, and I. Kanno, "Tracer delay correction of cerebral blood flow with dynamic susceptibility contrast-enhanced MRI," *Journal of Cerebral Blood Flow & Metabolism,* vol. 25, pp. 378-390, 2005.

[91] S. Sourbron, M. Ingrisch, A. Siefert, M. Reiser, and K. Herrmann, "Quantification of cerebral blood flow, cerebral blood volume, and blood-brain-barrier leakage with DCE-MRI," *Magn Reson Med,* vol. 62, pp. 205-17, Jul 2009.

[92] P. S. Tofts, "Modeling tracer kinetics in dynamic Gd-DTPA MR imaging," *J Magn Reson Imaging,* vol. 7, pp. 91-101, Jan-Feb 1997.

[93] C. S. Patlak and R. G. Blasberg, "Graphical evaluation of blood-to-brain transfer constants from multiple-time uptake data. Generalizations," *J Cereb Blood Flow Metab,* vol. 5, pp. 584-90, Dec 1985.

[94] N. M. Hirsch and C. Preibisch, "T2* Mapping with Background Gradient Correction Using Different Excitation Pulse Shapes," *American Journal of Neuroradiology,* vol. 34, pp. E65-E68, 2012.

[95] T. Christen, B. Lemasson, N. Pannetier, R. Farion, C. Segebarth, C. Rémy*, et al.*, "Evaluation of a quantitative blood oxygenation level-dependent (qBOLD) approach to map local blood oxygen saturation," *NMR in Biomedicine,* pp. n/a-n/a, 2010.

[96] W. M. Spees, D. A. Yablonskiy, M. C. Oswood, and J. J. Ackerman, "Water proton MR properties of human blood at 1.5 Tesla: magnetic susceptibility, T(1), T(2), T*(2), and non-Lorentzian signal behavior," *Magn Reson Med,* vol. 45, pp. 533-42, Apr 2001.

[97] M. J. Silvennoinen, C. S. Clingman, X. Golay, R. A. Kauppinen, and P. C. van Zijl, "Comparison of the dependence of blood R2 and R2* on oxygen saturation at 1.5 and 4.7 Tesla," *Magn Reson Med,* vol. 49, pp. 47-60, Jan 2003.

[98] P. S. Tofts, G. Brix, D. L. Buckley, J. L. Evelhoch, E. Henderson, M. V. Knopp*, et al.*, "Estimating kinetic parameters from dynamic contrast-enhanced T(1)-weighted MRI of a diffusable tracer: standardized quantities and symbols," *J Magn Reson Imaging,* vol. 10, pp. 223-32, Sep 1999.

[99] C. Kalavagunta and G. J. Metzger, "A field comparison of r1 and r2* relaxivities of Gd-DTPA in aqueous solution and whole blood: 3T versus 7T," presented at the Proc. Intl. Soc. Mag. Reson. Med. 18, 2010.

[100] M. A. Bernstein. (2004). *Handbook of MRI Pulse Sequences*.

[101] K. E. Emblem, A. Bjørnerud, K. Mouridsen, R. J. H. Borra, T. T. Batchelor, R. K. Jain*, et al.*, "T1- and T2*-dominant extravasation correction in DSC-MRI: Part II—predicting patient outcome after a single dose of cediranib in recurrent glioblastoma patients," *Journal of Cerebral Blood Flow & Metabolism,* vol. 31, pp. 2054-2064, 2011.

[102] E. S. Paulson and K. M. Schmainda, "Comparison of Dynamic Susceptibility-weighted Contrast-enhanced MR Methods: Recommendations for Measuring Relative Cerebral Blood Volume in Brain Tumors," *Radiology,* vol. 249, 2008.

[103] N. L. o. Medicine. DailyMed [Online]. Available: http://dailymed.nlm.nih.gov/dailymed/

[104] T. Pyka, J. Gempt, D. Hiob, F. Ringel, J. Schlegel, S. Bette, *et al.*, "Textural analysis of pre-therapeutic [18F]-FET-PET and its correlation with tumor grade and patient survival in high-grade gliomas," *Eur J Nucl Med Mol Imaging,* vol. 43, pp. 133-41, Jan 2016.

[105] A. Habermeier, J. Graf, B. F. Sandhofer, J. P. Boissel, F. Roesch, and E. I. Closs, "System L amino acid transporter LAT1 accumulates O-(2-fluoroethyl)-L-tyrosine (FET)," *Amino Acids,* vol. 47, pp. 335-44, Feb 2015.

[106] S. Haller and A. J. Bartsch, "Pitfalls in FMRI," *Eur Radiol,* vol. 19, pp. 2689-706, Nov 2009.

[107] R. Sladky, K. J. Friston, J. Trostl, R. Cunnington, E. Moser, and C. Windischberger, "Slice-timing effects and their correction in functional MRI," *Neuroimage,* vol. 58, pp. 588-94, Sep 15 2011.

[108] L. Shi, D. Wang, W. Liu, K. Fang, Y. X. Wang, W. Huang, *et al.*, "Automatic detection of arterial input function in dynamic contrast enhanced MRI based on affinity propagation clustering," *J Magn Reson Imaging,* vol. 39, pp. 1327-37, May 2014.

[109] K. Shi, X. Cheng, S. Forster, and S. Ziegler, "Hierarchical pharmacokinetic modeling for the analysis of dynamic F-18 FET PET/MR," *J NUCL MED MEETING ABSTRACTS,* vol. 55, pp. 43-, May 1, 2014 2014.

[110] H. An and W. Lin. (2002, 01). Cerebral venous and arterial blood volumes can be estimated separately in humans using magnetic resonance imaging Magnetic Resonance in Medicine Volume 48, Issue 4. *Magnetic Resonance in Medicine 48(4),* 583-588. Available: http://onlinelibrary.wiley.com/doi/10.1002/mrm.10257/abstract

[111] M. E. Raichle, A. M. MacLeod, A. Z. Snyder, W. J. Powers, D. A. Gusnard, and G. L. Shulman, "A default mode of brain function," *Proc Natl Acad Sci U S A,* vol. 98, pp. 676-82, Jan 16 2001.

[112] F. Calamante, A. Connelly, and M. J. van Osch, "Nonlinear ΔR2* effects in perfusion quantification using bolus-tracking MRI," *Magnetic Resonance in Medicine,* vol. 61, pp. 486-492, 2009.

[113] L. S. Hu, Z. Kelm, P. Korfiatis, A. C. Dueck, C. Elrod, B. M. Ellingson*, et al.*, "Impact of Software Modeling on the Accuracy of Perfusion MRI in Glioma," *AJNR Am J Neuroradiol,* vol. 36, pp. 2242-9, Dec 2015.

[114] C. Z. Simonsen, L. Østergaard, P. Vestergaard-Poulsen, L. Rohl, A. Bjornerud, and C. Gyldensted, "CBF and CBV measurements by USPIO bolus tracking: reproducibility and comparison with Gd-based values," *J Magn Reson Imaging,* vol. 9, pp. 342-7, Feb 1999.

[115] X. Zhang, M. D. Pagel, A. F. Baker, and R. J. Gillies, "Reproducibility of magnetic resonance perfusion imaging," *PLoS One,* vol. 9, p. e89797, 2014.

[116] L. Willats, A. Connelly, and F. Calamante, "Improved deconvolution of perfusion MRI data in the presence of bolus delay and dispersion," *Magn Reson Med,* vol. 56, pp. 146-56, Jul 2006.

[117] M. Ibaraki, E. Shimosegawa, H. Toyoshima, K. Ishigame, H. Ito, K. Takahashi*, et al.*, "Effect of regional tracer delay on CBF in healthy subjects measured with dynamic susceptibility contrast-enhanced MRI: comparison with 15O-PET," *Magn Reson Med Sci,* vol. 4, pp. 27-34, 2005.

[118] O. Wu, L. Østergaard, W. J. Koroshetz, L. H. Schwamm, J. O'Donnell, P. W. Schaefer*, et al.*, "Effects of tracer arrival time on flow estimates in MR perfusion-weighted imaging," *Magnetic Resonance in Medicine,* vol. 50, pp. 856-64, Oct 2003.

[119] A. Bjørnerud and K. E. Emblem, "A fully automated method for quantitative cerebral hemodynamic analysis using DSC–MRI," *Journal of Cerebral Blood Flow & Metabolism,* vol. 30, pp. 1066-1078, 2010.

[120] H.-L. Liu, Y. Pu, Y. Liu, L. Nickerson, T. Andrews, P. T. Fox*, et al.*, "Cerebral blood flow measurement by dynamic contrast MRI using singular value decomposition with an adaptive threshold," *Magnetic Resonance in Medicine,* vol. 42, pp. 167-172, 1999.

[121] G. J. Stanisz, E. E. Odrobina, J. Pun, M. Escaravage, S. J. Graham, M. J. Bronskill*, et al.*, "T1, T2 relaxation and magnetization transfer in tissue at 3T," *Magnetic Resonance in Medicine,* vol. 54, pp. 507-512, 2005.

[122] M. Law, S. Yang, J. S. Babb, E. A. Knopp, J. G. Golfinos, D. Zagzag*, et al.*, "Comparison of cerebral blood volume and vascular permeability from dynamic susceptibility contrast-enhanced perfusion MR imaging with glioma grade," *AJNR Am J Neuroradiol,* vol. 25, pp. 746-55, May 2004.

[123] K. E. Emblem, B. Nedregaard, T. Nome, P. Due-Tonnessen, J. K. S. Hald, D., O. C. Borota*, et al.*, "Glioma Grading by Using Histogram Analysis of Blood Volume Heterogeneity from MR-derived Cerebral Blood Volume Maps," *Radiology,* vol. 247, 2008.

[124] H. Kim, S. H. Choi, J. H. Kim, I. Ryoo, S. C. Kim, J. A. Yeom*, et al.*, "Gliomas: application of cumulative histogram analysis of normalized cerebral blood volume on 3 T MRI to tumor grading," *PLoS One,* vol. 8, p. e63462, 2013.

[125] Y. Meng and H. Lei, "A single-scan T2* mapping method based on two gradient-echo images with compensation for macroscopic field inhomogeneity," *Magn Reson Med,* vol. 60, pp. 1388-95, Dec 2008.

[126] K. Murase, K. Kikuchi, H. Miki, T. Shimizu, and J. Ikezoe. (2001, 01). Determination of arterial input function using fuzzy clustering for quantification of cerebral blood flow with dynamic susceptibility contrast-enhanced MR imaging Journal of Magnetic Resonance Imaging Volume 13, Issue 5. *Journal of Magnetic Resonance Imaging 13(5),* 797-806. Available: http://onlinelibrary.wiley.com/doi/10.1002/jmri.1111/abstract

[127] D. Peruzzo, A. Bertoldo, F. Zanderigo, and C. Cobelli, "Automatic selection of arterial input function on dynamic contrast-enhanced MR images," *Comput Methods Programs Biomed,* vol. 104, pp. e148-57, Dec 2011.

[128] M. Helle, S. Rufer, M. J. van Osch, A. Nabavi, K. Alfke, D. G. Norris*, et al.*, "Superselective arterial spin labeling applied for flow territory mapping in various cerebrovascular diseases," *J Magn Reson Imaging,* vol. 38, pp. 496-503, Aug 2013.

[129] C. Nasel, A. Azizi, A. Wilfort, R. Mallek, and E. Schindler, "Measurement of time-to-peak parameter by use of a new standardization method in patients with stenotic or occlusive disease of the carotid artery," *AJNR Am J Neuroradiol,* vol. 22, pp. 1056-61, Jun-Jul 2001.

[130] T. Barrett, M. Brechbiel, M. Bernardo, and P. L. Choyke, "MRI of tumor angiogenesis," *J Magn Reson Imaging,* vol. 26, pp. 235-49, Aug 2007.

[131] M. M. Teng, I. C. Cho, Y. H. Kao, C. S. Chuang, F. Y. Chiu, and F. C. Chang, "Improvements in the quantitative assessment of cerebral blood volume and flow with the removal of vessel voxels from MR perfusion images," *Biomed Res Int,* vol. 2013, p. 382027, 2013.

[132] A. M. Smith, C. B. Grandin, T. Duprez, F. Mataigne, and G. Cosnard, "Whole brain quantitative CBF, CBV, and MTT measurements using MRI bolus tracking: implementation and application to data acquired from hyperacute stroke patients," *J Magn Reson Imaging,* vol. 12, pp. 400-10, Sep 2000.

[133] C. Grandin, A. Bol, A. Smith, C. Michel, and G. Cosnard, "Absolute CBF and CBV measurements by MRI bolus tracking before and after acetazolamide challenge: Repeatabilily and comparison with PET in humans," *NeuroImage,* 2005.

[134] A. Stadlbauer, P. Pichler, M. Karl, S. Brandner, C. Lerch, B. Renner*, et al.*, "Quantification of serial changes in cerebral blood volume and metabolism in patients with recurrent glioblastoma undergoing antiangiogenic therapy," *Eur J Radiol,* vol. 84, pp. 1128-36, Jun 2015.

[135] K. Nael, B. Mossadeghi, T. Boutelier, W. Kubal, E. A. Krupinski, J. Dagher*, et al.*, "Bayesian estimation of cerebral perfusion using reduced-contrast-dose dynamic susceptibility contrast perfusion at 3T," *AJNR Am J Neuroradiol,* vol. 36, pp. 710-8, Apr 2015.

[136] R. Wirestam, O. Thilmann, L. Knutsson, I. M. Bjorkman-Burtscher, E. M. Larsson, and F. Stahlberg, "Comparison of quantitative dynamic susceptibility-contrast MRI perfusion estimates obtained using different contrast-agent administration schemes at 3T," *Eur J Radiol,* vol. 75, pp. e86-91, Jul 2010.

[137] G. Zaharchuk, R. Bammer, M. Straka, R. D. Newbould, J. Rosenberg, J.-M. Olivot*, et al.*, "Improving dynamic susceptibility contrast MRI measurement of quantitative cerebral blood flow using corrections for partial volume and nonlinear contrast relaxivity: A xenon computed tomographic comparative study," *Journal of Magnetic Resonance Imaging,* vol. 30, pp. 743-752, 2009.

[138] L. Knutsson, E. Lindgren, A. Ahlgren, M. J. van Osch, K. M. Bloch, Y. Surova*, et al.*, "Dynamic susceptibility contrast MRI with a prebolus contrast agent administration design for improved absolute quantification of perfusion," *Magn Reson Med,* vol. 72, pp. 996-1006, Oct 2014.

[139] J. R. Alger, T. J. Schaewe, T. C. Lai, A. J. Frew, P. M. Vespa, M. Etchepare, *et al.*, "Contrast agent dose effects in cerebral dynamic susceptibility contrast magnetic resonance perfusion imaging," *J Magn Reson Imaging,* vol. 29, pp. 52-64, Jan 2009.

[140] Y. H. Kao, M. M. Teng, W. Y. Zheng, F. C. Chang, and Y. F. Chen, "Removal of CSF pixels on brain MR perfusion images using first several images and Otsu's thresholding technique," *Magn Reson Med,* vol. 64, pp. 743-8, Sep 2010.

[141] H. B. Larsson, F. Courivaud, E. Rostrup, and A. E. Hansen, "Measurement of brain perfusion, blood volume, and blood-brain barrier permeability, using dynamic contrast-enhanced T(1)-weighted MRI at 3 tesla," *Magn Reson Med,* vol. 62, pp. 1270-81, Nov 2009.

[142] D. Bonekamp, K. Deike, B. Wiestler, W. Wick, M. Bendszus, A. Radbruch, *et al.*, "Association of overall survival in patients with newly diagnosed glioblastoma with contrast-enhanced perfusion MRI Comparison of intraindividually matched T1- and T2*-based bolus techniques, Journal of Magnetic Resonance Imaging Volume 42, Issue 1," *Journal of Magnetic Resonance Imaging,* vol. 42, pp. 87-96, 01 2015.

[143] H. A. Haroon, T. F. Patankar, X. P. Zhu, K. L. Li, N. A. Thacker, M. J. Scott, *et al.*, "Comparison of cerebral blood volume maps generated from T2* and T1 weighted MRI data in intra-axial cerebral tumours," *Br J Radiol,* vol. 80, pp. 161-8, Mar 2007.

[144] M. Law, D. E. Meltzer, S. G. Wetzel, S. Yang, E. A. Knopp, J. Golfinos, *et al.*, "Conventional MR imaging with simultaneous measurements of cerebral blood volume and vascular permeability in ganglioglioma," *Magn Reson Imaging,* vol. 22, pp. 599-606, Jun 2004.

[145] T. Christen, N. A. Pannetier, W. W. Ni, D. Qiu, M. E. Moseley, N. Schuff, *et al.*, "MR vascular fingerprinting: A new approach to compute cerebral blood volume, mean vessel radius, and oxygenation maps in the human brain," *Neuroimage,* vol. 89, pp. 262-70, Apr 1 2014.

[146] B. M. Ellingson, T. Zaw, T. F. Cloughesy, K. M. Naeini, S. Lalezari, S. Mong, *et al.*, "Comparison between intensity normalization techniques for dynamic susceptibility contrast (DSC)-MRI estimates of cerebral blood volume (CBV) in human gliomas," *J Magn Reson Imaging,* vol. 35, pp. 1472-7, Jun 2012.

[147] D. Bedekar, T. Jensen, and K. M. Schmainda, "Standardization of Relative Cerebral Blood Volume (rCBV) Image Maps for Ease of Both Inter- and Intrapatient Comparisons," *Magnetic Resonance in Medicine,* vol. 64, pp. 907-913, Sep 2010.

[148] A. Server, B. A. Graff, T. E. D. Orheim, T. Schellhorn, R. Josefsen, Ø. B. Gadmar*, et al.*, "Measurements of diagnostic examination performance and correlation analysis using microvascular leakage, cerebral blood volume, and blood flow derived from 3T dynamic susceptibility-weighted contrast-enhanced perfusion MR imaging in glial tumor grading," *Neuroradiology,* vol. 53, pp. 435-447, 2010.

[149] S. P. Cramer, H. Simonsen, J. L. Frederiksen, E. Rostrup, and H. B. W. Larsson, "Abnormal blood–brain barrier permeability in normal appearing white matter in multiple sclerosis investigated by MRI," *NeuroImage: Clinical,* vol. 4, pp. 182-189, 2014.

[150] C. Manka, F. Traber, J. Gieseke, H. H. Schild, and C. K. Kuhl, "Three-dimensional dynamic susceptibility-weighted perfusion MR imaging at 3.0 T: feasibility and contrast agent dose," *Radiology,* vol. 234, pp. 869-77, Mar 2005.

[151] N. Mauz, A. Krainik, I. Tropres, L. Lamalle, E. Sellier, O. Eker*, et al.*, "Perfusion magnetic resonance imaging: comparison of semiologic characteristics in first-pass perfusion of brain tumors at 1.5 and 3 Tesla," *J Neuroradiol,* vol. 39, pp. 308-16, Dec 2012.

[152] S. Gahramanov, L. Muldoon, X. Li, and E. Neuwelt, "Improved Perfusion MR Imaging Assessment of Intracerebral Tumor Blood Volume and Antiangiogenic Therapy Effi cacy in a Rat Model with Ferumoxytol," *Radiology,* vol. 261, pp. 796-804, 2011.

[153] M. Rohrer, H. Bauer, J. Mintorovitch, M. Requardt, and H. J. Weinmann, "Comparison of magnetic properties of MRI contrast media solutions at different magnetic field strengths," *Invest Radiol,* vol. 40, pp. 715-24, Nov 2005.

[154] M. Wintermark, G. W. Albers, A. V. Alexandrov, J. R. Alger, R. Bammer, J. C. Baron*, et al.*, "Acute stroke imaging research roadmap," *AJNR Am J Neuroradiol,* vol. 29, pp. e23-30, May 2008.

[155] J. L. Boxerman, B. R. Rosen, and R. M. Weisskoff, "Signal-to-noise analysis of cerebral blood volume maps from dynamic NMR imaging studies," *J Magn Reson Imaging,* vol. 7, pp. 528-37, May-Jun 1997.

[156] S. Veldhoen, M. Oechsner, A. Fischer, A. M. Weng, A. S. Kunz, T. A. Bley, *et al.*, "Dynamic Contrast-Enhanced Magnetic Resonance Imaging for Quantitative Lung Perfusion Imaging Using the Dual-Bolus Approach: Comparison of 3 Contrast Agents and Recommendation of Feasible Doses," *Invest Radiol,* vol. 51, pp. 186-93, Mar 2016.

[157] F. L. Giesel, A. Mehndiratta, and M. Essig, "High-relaxivity contrast-enhanced magnetic resonance neuroimaging: a review," *Eur Radiol,* vol. 20, pp. 2461-74, Oct 2010.

[158] S. Sourbron, M. Heilmann, A. Biffar, C. Walczak, J. Vautier, A. Volk, *et al.*, "Bolus-tracking MRI with a simultaneous T1- and T2*-measurement," *Magn Reson Med,* vol. 62, pp. 672-81, Sep 2009.

[159] J. M. Lupo, S. M. Cha, S. M. Chang, and S. J. Nelson, "Dynamic susceptibility-weighted perfusion Imaging of high-grade gliomas: Characterization of spatial heterogeneity," *American Journal of Neuroradiology,* vol. 26, pp. 1446-1454, Jun-Jul 2005.

[160] R. Luypaert, S. Sourbron, and J. de Mey, "Validity of perfusion parameters obtained using the modified Tofts model: a simulation study," *Magn Reson Med,* vol. 65, pp. 1491-7, May 2011.

[161] S. P. Sourbron and D. L. Buckley, "On the scope and interpretation of the Tofts models for DCE-MRI," *Magn Reson Med,* vol. 66, pp. 735-45, Sep 2011.

[162] J. M. Srour, W. Shin, S. Shah, A. Sen, and T. J. Carroll, "SCALE-PWI: A pulse sequence for absolute quantitative cerebral perfusion imaging," *J Cereb Blood Flow Metab,* vol. 31, pp. 1272-82, May 2011.

[163] X. P. Zhu, K. L. Li, I. D. Kamaly-Asl, D. R. Checkley, J. J. Tessier, J. C. Waterton, *et al.*, "Quantification of endothelial permeability, leakage space, and blood volume in brain tumors using combined T1 and T2* contrast-enhanced dynamic MR imaging," *J Magn Reson Imaging,* vol. 11, pp. 575-85, Jun 2000.

[164] V. Patil, J. H. Jensen, and G. Johnson, "Intravascular contrast agent T2* relaxivity in brain tissue," *NMR in Biomedicine,* vol. 26, pp. 392-399, 2013.

[165] V. Patil, G. Johnson, and J. H. Jensen, "Robust quantification of contrast agent (CA) concentration with magnetic field correlation (MFC) imaging," *Magn Reson Med,* vol. 62, pp. 1002-6, Oct 2009.

[166] L. Knutsson, F. Stahlberg, R. Wirestam, and M. J. van Osch, "Effects of blood DeltaR2* non-linearity on absolute perfusion quantification using DSC-MRI: comparison with Xe-133 SPECT," *Magn Reson Imaging,* vol. 31, pp. 651-5, Jun 2013.

[167] C. Hutton, A. Bork, O. Josephs, R. Deichmann, J. Ashburner, and R. Turner, "Image Distortion Correction in fMRI: A Quantitative Evaluation," *Neuroimage,* vol. 16, pp. 217-240, 2002.

[168] P. R. Bannister and J. M. Brady, "Non-rigid Motion Estimation and Spatio-temporal Realignment in FMRI," 2004.

[169] M. Salluzzi, R. Frayne, and M. R. Smith, "Is correction necessary when clinically determining quantitative cerebral perfusion parameters from multi-slice dynamic susceptibility contrast MR studies?," *Phys Med Biol,* vol. 51, pp. 407-24, Jan 21 2006.

[170] R. K. Kosior, J. C. Kosior, and R. Frayne, "Improved dynamic susceptibility contrast (DSC)-MR perfusion estimates by motion correction," *J Magn Reson Imaging,* vol. 26, pp. 1167-72, Oct 2007.

[171] M. Bergamino, L. Saitta, L. Barletta, L. Bonzano, G. L. Mancardi, L. Castellan*, et al.*, "Measurement of blood-brain barrier permeability with t1-weighted dynamic contrast-enhanced MRI in brain tumors: a comparative study with two different algorithms," *ISRN Neurosci,* vol. 2013, p. 905279, 2013.

[172] K. M. Donahue, H. G. J. Krouwer, S. D. Rand, A. P. Pathak, C. S. Marszalkowski, S. C. Censky*, et al.*, "Utility of simultaneously acquired gradient-echo and spin-echo cerebral blood volume and morphology maps in brain tumor patients," *Magnetic Resonance in Medicine,* vol. 43, pp. 845-853, 2000.

11 Acknowledgment

At this point, I would like to thank all the people that supported me during this thesis. Above all, PD Dr. Christine Preibisch, my supervisor, for having always time for my questions, giving me helpful suggestions and always motivating me. Further, I thank Prof. Dr. Axel Haase and Prof. Dr. Sybille Ziegler for being my supervisor and mentor, and Prof. Dr. Claus Zimmer for the opportunity to work at the Neuroradiology department. I would also like to thank Mathias Lukas und Dr. Kuangyu Shi for their help with the PET data and for providing the PET-based CBV maps. Furthermore, I thank Dr. Annette Förschler for providing the data of the dual contrast agent group. My grateful thanks are also extended to Dr. Marcus Settles for his helpful reflections about the arterial input function and because he always had an open ear for my problems. Further, I would thank all my colleagues in the office for so many constructive discussions. In addition, I thank Barbara Cervantes and John Meakin for proofreading my dissertation.
Thanks to all of you!